

AD-A056 892 PURDUE UNIV LAFAYETTE IND SCHOOL OF MECHANICAL ENGI--ETC F/G 21/9.2  
THE EFFECT OF OXIDIZER PARTICLE SIZE DISTRIBUTION ON THE STEADY--ETC(U)  
JUN 78 J A CONDON, J R OSBORN F04611-76-C-0067

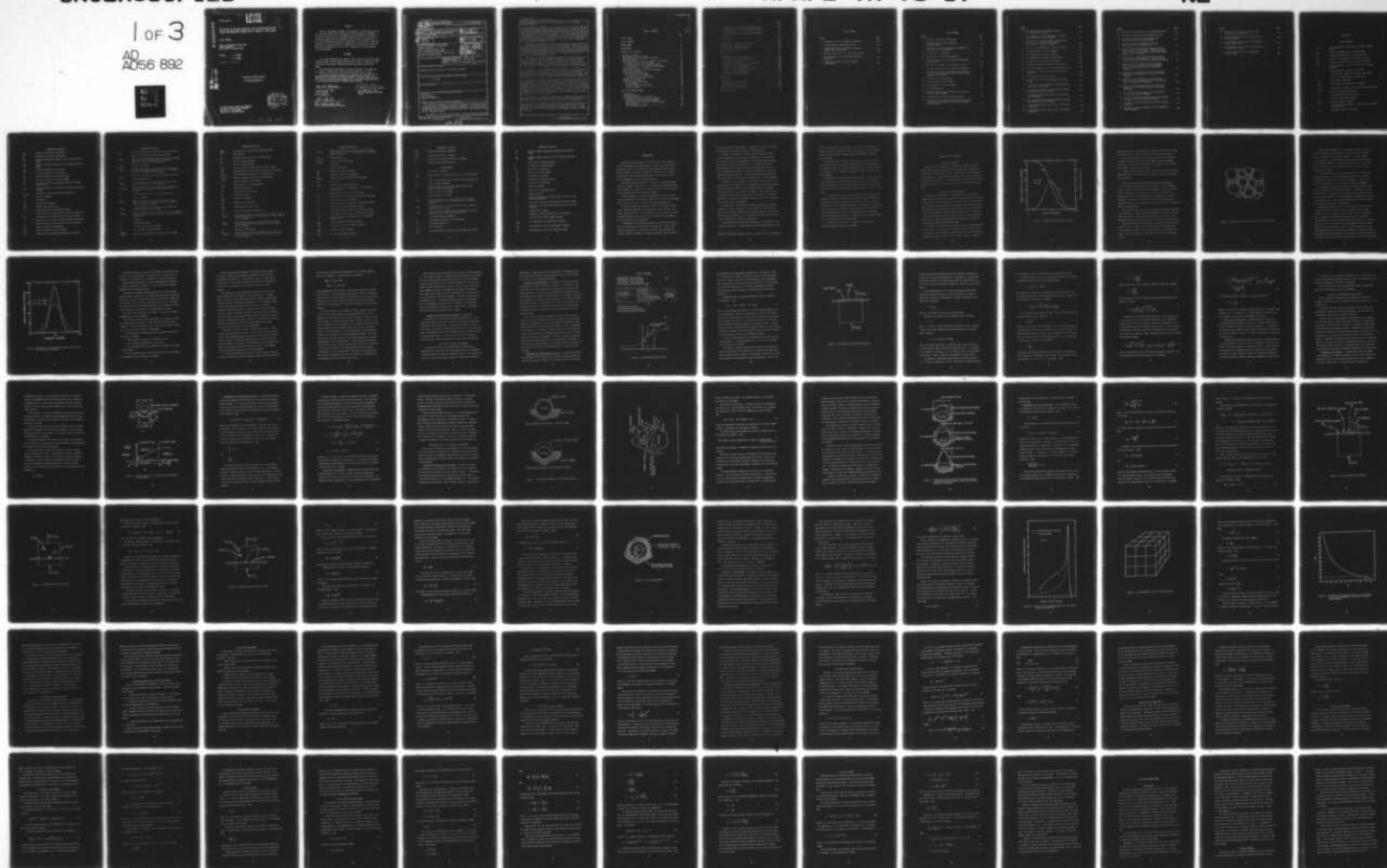
UNCLASSIFIED

AFRPL-TR-78-17

NL

1 OF 3

AD  
A056 892



AD A056892

AFRPL-TR-78-17

LEVEL

THE EFFECT OF OXIDIZER PARTICLE SIZE DISTRIBUTION ON THE  
STEADY AND NONSTEADY COMBUSTION OF COMPOSITE PROPELLANTS

FINAL REPORT

SCHOOL OF MECHANICAL ENGINEERING  
PURDUE UNIVERSITY  
WEST LAFAYETTE, INDIANA 47907

AUTHORS: J. A. CONDON

J. R. OSBORN

J U N E 1 9 7 8

AD No.   
DDC FILE COPY

APPROVED FOR PUBLIC RELEASE

DISTRIBUTION UNLIMITED

AIR FORCE ROCKET PROPULSION LABORATORY  
DIRECTOR OF SCIENCE AND TECHNOLOGY  
AIR FORCE SYSTEMS COMMAND  
EDWARDS AFB, CALIFORNIA 93523

DDC  
RECEIVED  
AUG 1 1978  
RECEIVED

78 07 27 007



## NOTICES

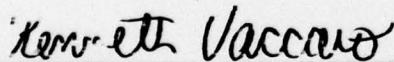
When U.S. Government drawings, specifications, or other data are used for any purpose other than a definitely related Government procurement operation, the fact that the Government may have formulated, furnished, or in any way supplied the said drawings, specifications, or other data, is not to be regarded by implication or otherwise, or in any manner licensing the holder or any other person or corporation, or conveying any rights or permission to manufacture, use, or sell any patented invention that may be related thereto.

## FOREWORD

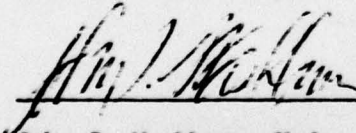
This report summarizes the technical effort and the conclusions reached during the course of the program conducted under Contract F04611-76-C-0067 with the Air Force Rocket Propulsion Laboratory, Edwards, California, 93523.

The Co-Principal Investigators for the program were J.A. Condon and J.R. Osborn. Contributions to the program were made by J.P. Renie.


This report has been reviewed by the Information Office (XOJ) and is releaseable to the National Technical Information Service (NTIS). At NTIS it will be available to the general public, including foreign nations. This technical report has been reviewed and is approved for publication; it is unclassified and suitable for general public release.



K. Vaccaro, Capt. USAF  
Project Manager  
For the Commander



John I. Washburn, Major, USAF  
Chief, Propulsion Analysis Division



J.J. Donn, Capt., USAF  
Chief, Combustion and Plumes  
Branch

UNCLASSIFIED

SECURITY CLASSIFICATION OF THIS PAGE (When Data Entered)

REPORT DOCUMENTATION PAGE		READ INSTRUCTIONS BEFORE COMPLETING FORM	
1. REPORT NUMBER AFRPL-TR-78-17	2. GOVT ACCESSION NO.	3. RECIPIENT'S CATALOG NUMBER	
4. TITLE (and Subtitle) THE EFFECT OF OXIDIZER PARTICLE SIZE DISTRIBUTION ON THE STEADY AND NONSTEADY COMBUSTION OF COMPOSITE PROPELLANTS.		5. TYPE OF REPORT & PERIOD COVERED Final Report	
6. AUTHOR J. A. Condon J. R. Osborn		7. PERFORMING ORG. REPORT NUMBER	
8. PERFORMING ORGANIZATION NAME AND ADDRESS School of Mechanical Engineering Purdue University West Lafayette, Indiana 47907		9. CONTRACT OR GRANT NUMBER(s) F04611-76-C-0067	
10. CONTROLLING OFFICE NAME AND ADDRESS Air Force Rocket Propulsion Laboratory/PA Edwards, California 93523		11. PROGRAM ELEMENT, PROJECT, TASK AREA & WORK UNIT NUMBERS 573 MODR 1710	
12. MONITORING AGENCY NAME & ADDRESS (if different from Controlling Office) 12 228 P.		13. REPORT DATE June 1978	
		14. NUMBER OF PAGES 226	
		15. SECURITY CLASS. (of this report) UNCLASSIFIED	
		16. DECLASSIFICATION/DOWNGRADING SCHEDULE N/A	
17. DISTRIBUTION STATEMENT (of this Report) Approved for Public Release: Distribution Unlimited			
18. DISTRIBUTION STATEMENT (of the abstract entered in Block 20, if different from Report) 623 02F			
19. SUPPLEMENTARY NOTES			
20. KEY WORDS (Continue on reverse side if necessary and identify by block number) Combustion Erosive Burning Combustion Instability			
21. ABSTRACT (Continue on reverse side if necessary and identify by block number) A theoretical analysis of the combustion of composite propellants (with an emphasis on the heterogeneous effects) is presented. The analysis based on the combination of a unique statistical treatment of the burning surface (9, 10) with a very comprehensive multiple flame type of physiochemical model for the combustion process.  The analysis is divided into four parts: the steady state burning rate.			

DD FORM 1 JAN 73 1473

EDITION OF 1 NOV 65 IS OBSOLETE  
S/N 0102-LF-014-6601

UNCLASSIFIED

SECURITY CLASSIFICATION OF THIS PAGE (When Data Entered)

292 070

alt



UNCLASSIFIED

SECURITY CLASSIFICATION OF THIS PAGE (When Data Entered)

erosive burning rate, the pressure coupled response, and the velocity coupled response.

The results of calculations with the steady state burning rate model are compared with the experimental results of Miller (6,7) for twenty one HTPB/AP propellants containing a wide range of oxidizer particle size distributions. The calculated values of both the burning rate and the pressure exponent are in good agreement with the experimental results. The poorest agreement with the experimental results occurs for propellants that contain a very wide overall particle size distribution. It is demonstrated that the poorer agreement is possible due to the lack of consideration of flame interactions between the flames of individual oxidizer particles.

The steady state burning rate model was extended to include erosive burning effects by coupling a model for the turbulent boundary layer over a flat plate with blowing to the steady state burning rate model. The erosive burning model is based on the hypothesis that the erosive effect is due to enhancement of the transport properties in the region of the gas phase reaction zone. The enhancement of the transport properties is assumed to be due to the presence of a turbulent boundary layer.

The results of calculations with the erosive burning model are not compared with experimental data. However, calculations are presented which illustrate that the model correctly predicts the experimentally observed trends in erosive burning. A critical particle diameter for erosive burning is defined since the combustion of oxidizer particles of diameter below the critical diameter is not influenced by the presence of a cross flow velocity.

Two pressure coupled response models are presented. One is based on the Cohen hypothesis which related the resonant frequency and peak magnitude of the pressure coupled response function of the oxidizer particle diameter. The other model is based on the Zel'dovich-Novozhilov formalism which relates the nonsteady state propellant properties to steady state propellant properties.

The theoretical pressure coupled response results compare favorably with the experimental results of several propellants. The addition of small particles to the oxidizer particle size distribution of a propellant is shown to increase the propellant's resonant frequency and the magnitude of the response. Conversely, the addition of coarse particles is shown to decrease the resonant frequency and the peak magnitude of the response. A sample calculation is presented which illustrates the dramatic effect of the oxidizer particle size distribution on the shape of the curve which represents the pressure coupled response as a function of frequency.

The model for the velocity coupled response is based on the previously described erosive burning model and the relation between the pressure coupled response and the velocity coupled response as derived by Lengelle (43).

The results of calculations with the velocity coupled response model indicate that the addition of coarse particles to the oxidizer particle size distribution of a propellant increases the potential for velocity coupling. Moreover, it is shown that the velocity coupled response vanishes as frequency is increased.

UNCLASSIFIED

SECURITY CLASSIFICATION OF THIS PAGE (When Data Entered)

# TABLE OF CONTENTS

	Page
LIST OF TABLES. . . . .	3
LIST OF FIGURES . . . . .	4
NOMENCLATURE. . . . .	8
INTRODUCTION. . . . .	15
REVIEW OF THE LITERATURE. . . . .	18
General Discussion. . . . .	18
The Composite Solid Propellant. . . . .	18
Description of the Combustion of Composite Solid Propellants . . . . .	20
Composite Propellant Combustion Models: Steady State . . . . .	27
The Granular Diffusion Flame Model . . . . .	27
The Hermance Heterogeneous Reaction Model. . . . .	36
The Beckstead-Derr Price Multiple Flame Model. . . . .	41
Description of Erosive Burning. . . . .	65
Experimental Observations of Erosive Burning. . . . .	66
Erosive Burning Models. . . . .	67
The Lenoir Robillard Model . . . . .	67
The Flame Displacement Model . . . . .	70
The Lengelle Erosive Burning Model . . . . .	73
Nonsteady State Combustion. . . . .	76
Nonsteady State Models. . . . .	78
The Denison and Baum Model . . . . .	79
The Cohen Model. . . . .	81
The Zel'dovich Novozhilov Model. . . . .	82
Lengelle's Model . . . . .	87
THE PETITE ENSEMBLE MODEL . . . . .	90
Introduction. . . . .	90
The Physical Model. . . . .	91
The Theoretical Steady State Model. . . . .	95
Derivation of the Statistical Formalism. . . . .	95
Derivation of the Physiochemical Model . . . . .	109
Modifications of the Model to Include Burning Rate Catalysts . . . . .	131
The Erosive Burning Model. . . . .	133



	Page
The PEM Nonsteady State Combustion Model. . . . .	149
Derivation of the Statistical Nonsteady Model. . . . .	149
The Pseudopropellant Pressure Coupled Response Function . . . . .	151
The Pseudopropellant Velocity Coupled Response Function . . . . .	154
ANALYTICAL RESULTS. . . . .	160
Introduction. . . . .	160
Steady State PEM Burning Rate Results . . . . .	160
Erosive Burning Results . . . . .	169
Pressure Coupled Response Results . . . . .	172
Velocity Coupled Response Results . . . . .	190
DISCUSSION OF RESULTS . . . . .	194
Introduction. . . . .	194
The Steady State Burning Rate . . . . .	194
Comparison with Experimental Results . . . . .	194
Oxidizer Particle Size Effects . . . . .	200
The Erosive Burning Rate. . . . .	204
Comparison with Experimental Observations. . . . .	204
Oxidizer Particle Size Effects . . . . .	207
The Pressure Coupled Response . . . . .	209
Comparison with Experimental Results . . . . .	209
Oxidizer Particle Size Effects . . . . .	210
The Velocity Coupled Response . . . . .	210
Oxidizer Particle Size Effects . . . . .	211
CONCLUSIONS . . . . .	212
Introduction. . . . .	212
The Steady State Burning Rate . . . . .	212
The Erosive Burning . . . . .	214
The Pressure Coupled Response . . . . .	216
The Velocity Coupled Response . . . . .	217
LIST OF REFERENCES. . . . .	219

## LIST OF TABLES

Table	Page
1. Correlation for the Log Normal Distributions. . . . .	161
2. Miller Propellant Compositional Grid. . . . .	163
3. Strand Burning Rate of the Miller Propellant Compositions at 1000 psia . . . . .	164
4. PEM Input Parameters for the Miller Propellants . . . . .	167
5. Oxidizer Particle Size Distribution Data for NWC-SP-520. . . . .	182
6. Oxidizer Composition of Miller Acoustic Propellants . . . . .	182

## LIST OF FIGURES

Figure	Page
1. A Typical Particle Size Distribution. . . . .	19
2. The Structure of a Typical Composite Propellant Mixture. . . . .	21
3. The Effect of the Distribution Width Parameter on the Particle Size Distribution. . . . .	23
4. The GDF Physical Description. . . . .	29
5. The Summerfield Surface Energy Balance. . . . .	31
6. Physical Description of the Hermance Heterogeneous Reaction Model. . . . .	38
7. The Pressure Dependence of the Hermance Crevice . . . . .	42
8. The Flame Structure for an AP Composite Propellant. . . . .	43
9. Interaction of Primary Flame and AP Monopropellant Flame at Different Pressures (Dashed Lines indicate hypothetical position). . . . .	46
10. The BDP Surface Energy Balance. . . . .	50
11. Energy Balance for the AP Flame . . . . .	51
12. Energy Balance for the Final Flame. . . . .	53
13. The Determination. . . . .	57
14. Diffusion Flame Standoff Distance as a Function of Oxidizer Volume Fraction. . . . .	61
15. The BDP Oxidizer Particle Packing Structure . . . . .	62
16. The Ratio of the Distance Between Oxidizer Particles to the Particle Diameter as a Function of Oxidizer Volume Fraction . . . . .	64



Figure	Page
17. The Packing Structure and Burning Surface of a Polydisperse Propellant. . . . .	93
18. The Rearrangement of the Polydisperse Propellant into Monodisperse Pseudopropellants . . . . .	94
19. Weight Percent Less than Diameter Versus Diameter, Comparison of Log Normal Distributions to Measured Data of Several AP Grinds. . . . .	108
20. The Birth and Consumption of an Oxidizer Particle . . . . .	110
21. The Pseudopropellant Burning Geometry . . . . .	113
22. The Pseudopropellant Surface Geometry . . . . .	114
23. The Pseudopropellant Surface Energy Balance . . . . .	119
24. The PEM One Dimensional Flame Structure . . . . .	120
25. The Burke-Schumann Bunsen Burner Configuration. . . . .	126
26. The Physical Model for the Turbulent Boundary Layer . . . . .	136
27. The Reduction in Shear Stress at the Wall Due to Injection . . . . .	142
28. The Boundary Layer Velocity Profile . . . . .	144
29. The Integrated Average Eddy Momentum Diffusivity Profile . . . . .	146
30. A Comparison of PEM Burning Rate with Experimental Burning Rate: Miller Data. . . . .	165
31. A Comparison of PEM Burning Rate Pressure Exponent with Experimental Data of Miller. . . . .	166
32. The Pseudopropellant Burning Rate Versus Oxidizer Particle Diameter . . . . .	170
33. The Pseudopropellant Burning Rate Pressure Exponent Versus Oxidizer Particle Diameter . . . . .	171
34. Propellant Burning Rate Versus Cross Flow Velocity at 1000 psia. . . . .	173
35. Propellant Burning Rate Versus Cross Flow Velocity at 500 psia . . . . .	174



Figure	Page
36. The Effect of Burning Rate on the Threshold Velocity . . . . .	175
37. The Effect of Pressure on the Threshold Velocity . . . . .	176
38. The Effect of Oxidizer Particle Size on the Pseudopropellant Erosive Burning Rate. . . . .	177
39. The Critical Particle Diameter for Erosive Burning Versus Free Stream Velocity. . . . .	178
40. The Real Part of the Normalized Response Function Versus Nondimensional Frequency: Comparison of the Cohen - Denison and Baum Method with the Experimental Results of A-13 Propellant . . . . .	180
41. The Real Part of the Normalized Response Function Versus Nondimensional Frequency: Comparison of ZN Method to the Experimental Results for A-13 Propellant . . . . .	181
42. Comparison of the Theoretical Results with the Cohen - Denison and Baum Method to Experimental Pressure Coupled Response Date of NWC-SP-520 Propellant . . . . .	184
43. Comparison of the Theoretical Results with the ZN Method to the Experimental Results for NWC-SP-520 Propellant . . . . .	185
44. Comparison of the Theoretical Results with the Cohen - Denison and Baum Method to the Experimental Results for the Miller Propellants . . . . .	186
45. Comparison of the Theoretical Results with the ZN Method to the Experimental Results for the Miller Propellants. . . . .	187
46. The Effect of Oxidizer Particle Size Distribution on the Pressure Coupled Response . . . . .	188
47. The Effect of Oxidizer Particle Size and Perturbation Frequency on the Pressure Coupled Response . . . . .	189
48. The Velocity Coupled Response for the Miller Acoustic Propellants. . . . .	191
49. The Effect of Oxidizer Particle Size on the Velocity Coupled Response . . . . .	192

Figure	Page
50. The Effect of Cross Flow Velocity on the Velocity Coupled Response . . . . .	.193
51. The Pseudopropellant Density Versus Oxidizer Particle Diameter . . . . .	.197
52. The Pseudopropellant Oxidizer Mass Fraction Versus Particle Size. . . . .	.198
53. The Pseudopropellant Oxidizer Volume Fraction Versus Particle Size. . . . .	.199
54. Gas Phase Reaction Zone in the Turbulent Boundary Layer. . . . .	.206

## NOMENCLATURE

### English Symbols

$A$	Empirical constant in the Denison and Baum nonsteady analysis
$A_{AP}$	Arrhenius frequency factor for the AP flame
$A_f$	Arrhenius pre-exponential for fuel pyrolysis
$A_{ox}$	Arrhenius pre-exponential for oxidizer pyrolysis
$A_{PF}$	Arrhenius frequency factor for the primary flame
$B$	Empirical constant in the Denison and Baum nonsteady analysis
$B$	Blowing parameter defined by equation 257
$b$	"Bunsen burner" diameter in diffusion flame analysis
$C$	Empirical constant defined in equation 135
$C_f$	Skin friction coefficient
$C_{f0}$	Skin friction coefficient with no blowing
$C_{ign}$	Constant in the equation for the oxidizer ignition delay
$C_p$	Specific heat of the propellant
$C'$	Constant described by equation 281
$c'$	Prandtl mixing length constant
$D_o$	Oxidizer particle diameter
$D'$	Mean intersection diameter of an oxidizer particle with the fuel plane
$d_f$	Distance of the fuel regression



# NOMENCLATURE (cont'd.)

$d_{ox}$	Distance of the oxidizer regression
$D$	Molecular gas diffusion coefficient
$D_{FF}^t$	Turbulent diffusion coefficient of gas below the final flame
$D_{PF}^t$	Turbulent diffusion coefficient of gas below the primary flame
$E_{AP}$	Activation energy for the AP flame
$E_f$	Activation energy for fuel pyrolysis
$E_{ox}$	Activation energy for oxidizer pyrolysis
$E_{PF}$	Activation energy for the primary flame
$F_k$	Oxidizer particle size distribution function given by equation 153
$F_{k,j}$	Oxidizer particle size distribution function for particles in mode j
$F_{p,d,k}$	Distribution function defined by equation 123
$f_p$	Resonant frequency
$h$	See Figure 21
$K_{AP}$	AP flame rate constant
$K_{PF}$	Primary flame rate constant
$k$	Thermal conductivity of combustion gases
$L$	Flame height for determining the average eddy diffusivity
$M_k$	The number of distribution modes of oxidizer specie k
$m$	Natural log of the oxidizer particle weight mean diameter
$\dot{m}$	Mass flux from an oxidizer particle fuel surface pair
$\dot{m}_f$	Mass flux from the fuel surface
$\dot{m}_{ox}$	Mass flux from the oxidizer surface
$\dot{m}_t$	Total mass flux from the propellant burning surface



# NOMENCLATURE (Cont'd)

$\bar{m}_t$	Average mass flux per unit planar burning surface area
$m''$	Mass flux at any point on the burning surface
$m''_{d,k}$	Mass flux per unit burning surface area from the subarea containing oxidizer particles of size between $D_o$ and $D_o + dD_o$ and oxidizer species k
$\bar{m}''_{d,k}$	Average of the above
$\bar{m}''_{p,d,k}$	Average mass flux per unit planar surface area from a subsurface containing oxidizer crystals of size between $D_o$ and $D_o + dD_o$ and oxidizer species k
$m_{o,k,j}$	Total mass of oxidizer in mode j and oxidizer specie k
$m'$	Fluctuating mass flux
$dm_{o,d,k}$	The elemental mass of oxidizer with diameter between $D_o$ and $D_o + dD_o$ and oxidizer specie k
$dm_{o,d,k,j}$	The elemental mass of oxidizer with diameter between $D_o$ and $D_o + dD_o$ in distribution mode j and oxidizer specie k
$N$	Total number of particles at the burning surface
$n$	Pressure exponent
$\Delta N_{p,d,k}$	Number of particles at the burning surface of size between $D_o$ and $D_o + dD_o$ and of species k, per unit of planar burning surface area
$dN_{o,d}$	The number of oxidizer crystals per unit volume with diameters between $D_o$ and $D_o + dD_o$
$dN_{p,d,k}$	Number of particles at the burning surface of size between $D_o$ and $D_o + dD_o$ and species k per unit of planar burning surface area
$P$	Pressure
$P'$	Fluctuating pressure
$Q_L$	Oxidizer net surface heat release
$Q_f$	Heat to vaporize the fuel binder
$Q_{surf}^{AP,FF}$	Heat flux at the surface from the AP and final flame

# NOMENCLATURE (Cont'd)

$Q_{surf}^{PF}$	Heat flux at the surface from the primary flame
$R$	See Figure 21
$Re_x$	Reynolds number based on down stream position
$R_p$	Pressure coupled response
$R_v$	Velocity coupled response
$R_{p,r}$	Real part of the pressure coupled response function
$R_{p,i}$	Imaginary part of the pressure coupled response function
$R_{p,d,k}$	Pressure coupled response of a pseudopropellant
$R_{v,d,k}$	Velocity coupled response of a pseudopropellant
$\bar{r}$	Average propellant burning rate
$\bar{r}_{d,k}$	Burning rate of a pseudopropellant
$S_b$	Burning surface area
$S_p$	Planar burning surface area
$S_f$	Fuel surface area
$S_{ox}$	Oxidizer surface area
$S_f^p$	Planar fuel surface area
$S_{ox}^p$	Planar oxidizer surface area
$S_T^p$	Planar total burning surface area
$S_{o,d,k}^*$	The exposed surface area of oxidizer in a pseudopropellant with oxidizer particles of size between $D_o$ and $D_o + dD_o$ and oxidizer specie k
$S_{p,d,k}^*$	Planar surface area of a pseudopropellant containing oxidizer particles of size between $D_o$ and $D_o + dD_o$ and oxidizer specie k
$s$	Number of oxidizer types
$\Delta S_{b,d,k}$	Burning surface area of a pseudopropellant containing oxidizer particles of size between $D_o$ and $D_o + dD_o$ and oxidizer specie k

# NOMENCLATURE (Cont'd)

$\Delta S_{p,d,k}$	Planar surface area of a pseudopropellant containing oxidizer particles of size between $D_0$ and $D_0 + dD_0$ and oxidizer species $k$
$\overline{\Delta S}_{p,d,k}$	Average of $\Delta S_{p,d,k}$
$\overline{\Delta S}_{o,d,k}$	The average value of $S_{o,d,k}^*$
$T$	Temperature
$T_s$	Surface temperature
$T_{AP}$	Adiabatic AP flame temperature
$T_{FF}$	Adiabatic final flame temperature
$T(x_{AP})$	Temperature at the location of the AP flame
$t_b$	Burn time
$t_{ign}$	Oxidizer particle ignition delay
$U$	Diameter exponent in the equation for the oxidizer ignition delay
$u$	Velocity parallel to the burning surface
$\bar{u}$	Time average velocity parallel to the burning surface
$u_e$	Rocket chamber core gas velocity
$u'$	Fluctuating velocity parallel to the burning surface
$v$	Velocity normal to the burning surface
$\bar{v}$	Time average velocity normal to the burning surface
$v'$	Fluctuating velocity normal to the burning surface
$W$	Pressure exponent in the equation for the oxidizer ignition delay
$x_{AP}$	Location of the AP flame heat release
$x_{FF}$	Location of the final flame heat release
$x_{AP}^*$	AP flame standoff distance
$x_{FF}^*$	Final flame standoff distance



# NOMENCLATURE (Cont'd.)

$x_{PD}^*$	Primary flame diffusion distance
$x_{PF}^*$	Primary flame kinetics distance
$x$	Natural log of the oxidizer particle diameter
$y$	Oxidizer particle number density

## Greek Symbols

$\alpha$	Oxidizer mass fraction
$\alpha_{d,k}^*$	Mass fraction of oxidizer specie $k$ in the psuedopropellant
$\beta$	Species concentration term in the diffusion flame analysis
$\beta_e$	Erosive burning strength
$\delta$	Distance between the inner and outer annulus of the "Bunsen burner" configuration
$\epsilon$	Eddy diffusivity of momentum
$\zeta$	Volume fraction of oxidizer
$\zeta_{d,k}^*$	The volume fraction of a psuedopropellant containing oxidizer particles of size between $D_0$ and $D_0 + dD_0$ and specie $k$
$d\zeta_d$	The volume fraction of oxidizer particles with diameter between $D_0$ and $D_0 + dD_0$
$\eta_{d,k}$	The fraction of particles in the propellant with diameter between $D_0$ and $D_0 + dD_0$ and oxidizer type $k$
$\lambda$	The complex frequency parameter
$\lambda_p$	The thermal conductivity of the propellant
$\lambda_i$	The imaginary part of $\lambda$
$\lambda_r$	The real part of $\lambda$
$\lambda_{AP}^t$	Turbulent thermal conductivity of gas below the AP flame



# NOMENCLATURE (Cont'd)

$\lambda_{FF}^t$	Turbulent thermal conductivity of gas below the final flame
$\lambda_{PF}^t$	Turbulent thermal conductivity of gas below the primary flame
$v$	Stoichiometric related variable
$\mu$	Viscosity of combustion gases
$\rho_e$	Density of the core gas
$\rho_f$	Density of the fuel binder
$\rho_{ox}$	Density of the oxidizer
$\rho_{o,k}$	Density of the oxidizer specie k
$\rho_p$	Density of the propellant
$\rho_t$	Propellant density
$\rho_{d,k}^*$	Density of the pseudopropellant
$\sigma$	Natural log of $\sigma^*$
$\sigma^*$	Standard deviation of oxidizer particle size in the log normal distribution
$\tau$	Life time of an oxidizer particle at the burning surface
$\tau_w$	Shear stress at the burning surface due to a cross flow velocity
$\Omega$	Dimensionless frequency
$\omega$	Frequency of the gas phase pressure oscillations
$\xi$	Non-dimensional flame standoff distance
$\xi_{AP}^*$	Non-dimensional AP flame standoff distance
$\xi_{PF}^*$	Non-dimensional primary flame standoff distance
$\xi_T^*$	Non-dimensional final flame standoff distance

## INTRODUCTION

Composite solid propellants are currently used in the majority of the solid propellant propulsion systems. Composite propellants are a mixture of a plastic fuel binder and finely ground oxidizer crystals. The fuel binder is initially a liquid but is polymerized to a solid after mixing. The oxidizer crystals range in size from less than a micron in diameter to several hundred microns.

The mixing properties, combustion properties, and mechanical properties of composite propellants can be changed by changing the mixture ratio of binder to oxidizer and by changing the overall solids particle size distribution within the propellant mixture.

In the formulation of composite propellants to satisfy specific mission requirements, the propellant chemist is faced with the formidable task of satisfying several stringent simultaneous constraints.

The basic variables the propellant chemist has at hand for formulating composite propellants are the amount and type of binder; the amount, type and particle size distribution of the oxidizer; the amount and type of burning rate catalyst; and the amount, type and particle size distribution of metal additives.

In determining the propellant formulation, the propellant chemist must first consider the desired ballistic properties. That is, the propellant must burn at a specified rate at any given pressure and initial propellant temperature within some specified range of pressures

and initial propellant temperatures. The particle size of the oxidizer has a profound effect upon the ballistic characteristics.

Currently, much attention is being given to nozzleless rockets. In this configuration the propellant is subjected to very high cross flow velocities which cause enhancement of the propellant burning rate. This effect is termed erosive burning. It is suggested that the oxidizer particle size distribution has a pronounced effect on the erosive burning characteristics of composite propellants. Thus, the propellant formulator may have to meet constraints regarding both the steady state and the erosive burning characteristics of the propellants.

In addition to the importance of the steady state ballistics, the nonsteady burning characteristics of the propellant are also significant, since the combustion processes may interact with spurious pressure oscillations present in the combustion chamber. That interaction can be such that the amplitude of the pressure oscillations is increased resulting in a condition of unstable combustion so destructive that the rocket engine itself is destroyed.

Spurious cross flow velocity oscillations can result in a similar condition of unstable combustion. Recent work (1-5)<sup>\*</sup> suggests that both types of unstable combustion are strongly dependent on the oxidizer particle size distribution. Thus, the propellant chemist may be forced to meet constraints on combustion instability.

The processability of the propellant must also be considered. Variations of the particle size distribution have a pronounced effect on the

---

\* Numbers in parentheses indicate references listed in the List of References.



after mix viscosity of the propellant. The propellant must have a viscosity low enough to permit it to flow into every corner of the rocket chamber in order to insure repeatability of performance of the propulsion system.

Having determined a propellant that meets the ballistics and processing constraints, the propellant must now also meet constraints on its mechanical properties. These properties are also influenced heavily by the particle size distribution of the solid oxidizer as well as the metal additive.

Unfortunately, definitive a priori methodologies relating ballistics processability and mechanical properties do not exist. Thus, the propellant formulator is left only with empiricisms and his own intuition to guide in the mixing of propellants that meet specific mission requirements.

It is evident, then, that a combustion model which describes the steady and nonsteady burning processes of composite solid propellants, with particular emphasis on particle size effects, should result in a valuable tool for the propellant formulator. The combustion model when used in conjunction with available empirical data (6,7) on the effect of oxidizer particle size and size distribution on the propellant's viscosity and mechanical properties should result in a complete description of the desired propellant formulation.

The objective of this research program is to develop such a combustion model for composite propellants.



## REVIEW OF THE LITERATURE

### General Discussion

The review of the literature is concerned with those pertinent references pertaining to the models of the steady state combustion of solid composite propellants as well as erosive burning and nonsteady state combustion. Before reviewing the models a brief description will be given of the composite solid propellant and the physical and chemical processes that occur near the burning surface of that composite propellant.

### The Composite Solid Propellant

The composite propellant is a heterogeneous mixture of finely ground oxidizer particles, with a plastic fuel binder which is initially a liquid but is finally polymerized to a solid. The oxidizer particles used in composite propellants are usually ground ammonium perchlorate (AP) crystals with a particle size range of from less than a micron in diameter to diameters as large as several hundred microns. Other oxidizers which are used to a lesser extent include cyclotetramethylene-tetranitramine (HMX), hydroxylammonium perchlorate (HAP), potassium perchlorate (KP) and ammonium nitrate (AN).

The number density of oxidizer particles in a composite propellant usually varies in a log normal distribution fashion with the size of the particle. This variation of particle number density with particle diameter is termed a particle size distribution. Figure 1 depicts a

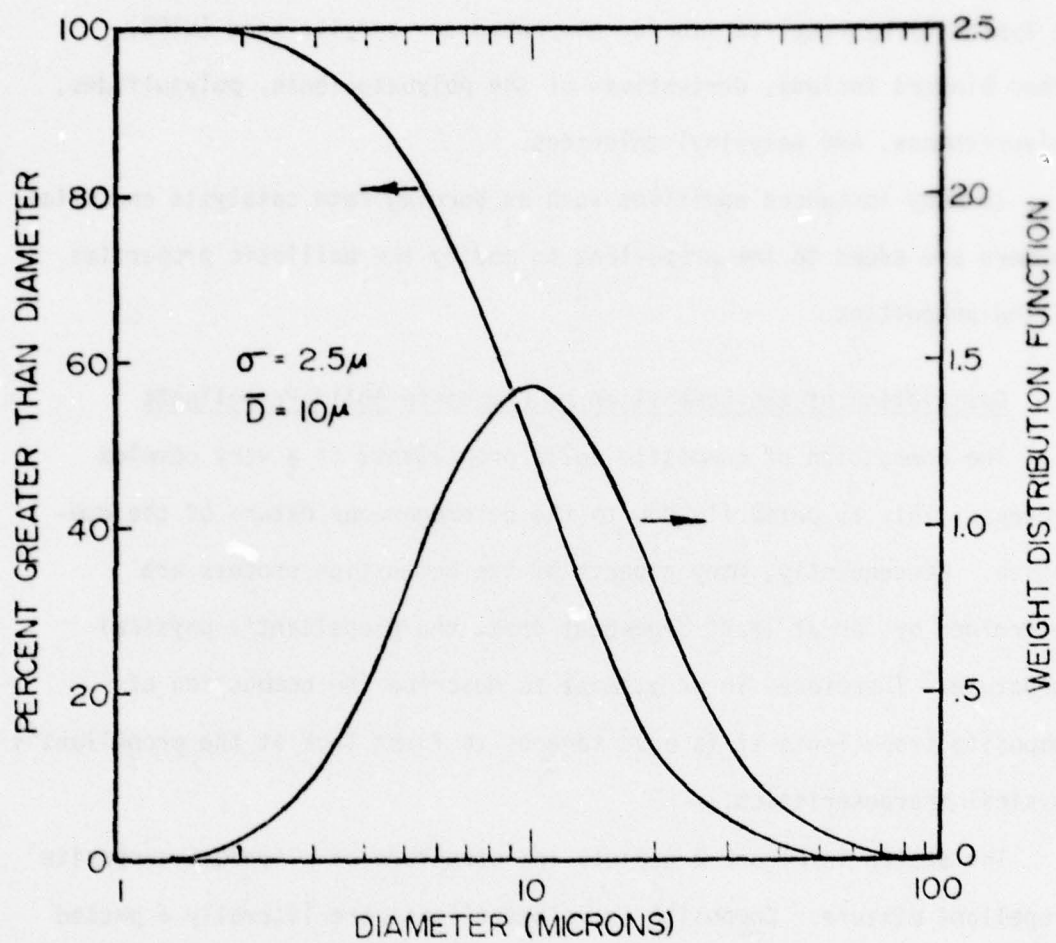


Figure 1. A Typical Particle Size Distribution

typical particle size distribution for a nominal diameter of ten microns. Composite propellants usually contain several distribution modes.

The fuel binder used in the formulation of composite propellants is typically hydroxyl-terminated polybutadiene acrylic acid (HTPB), other binders include, derivatives of the polybutadienes, polysulfides, polyurethanes, and polyvinyl chlorides.

In many instances additives such as burning rate catalysts and metal powders are added to the propellant to modify the ballistic properties of the propellant.

#### Description of the Combustion of Composite Solid Propellants

The combustion of composite solid propellants is a very complex process. This is primarily due to the heterogeneous nature of the composite. Consequently, many aspects of the combustion process are determined by, or at least dependent upon, the propellant's physical structure. Therefore, in an attempt to describe the combustion of composite propellants it is advantageous to first look at the propellant's physical characteristics.

The sketch in Figure 2 depicts the structure of a typical composite propellant mixture. Composite solid propellants are literally a packed bed of polydisperse oxidizer particles where the interstitial voids between the packing of the particles are filled with a continuous binder.

The oxidizer particles are ground to a desired size before the propellant is mixed. However, the oxidizer particles formed during the grinding process are not of one size but rather are a distribution of sizes. This distribution can be characterized by a log normal distribution.



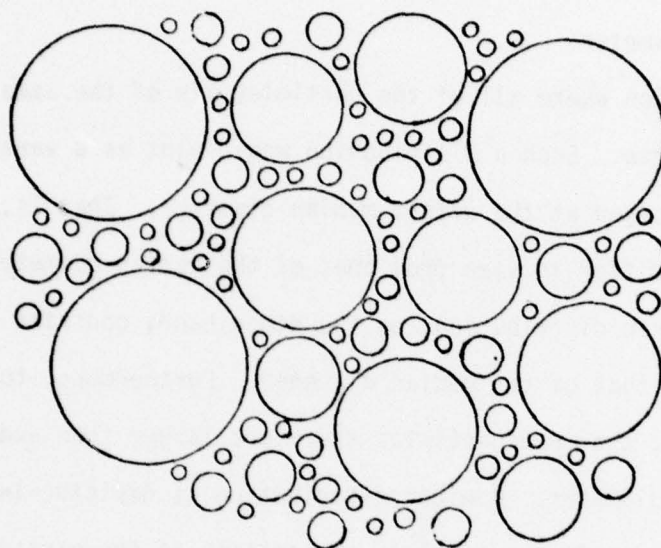


Figure 2. The Structure of a Typical Composite Propellant Mixture

Figure 3 shows the effect of the distribution width parameter on a typical particle size distribution. In Figure 3 particle number density is plotted as a function of diameter. The weight median (or 50%) diameter is given by that diameter where the number density curve reaches a maximum. The width of the distribution is representative of the number of particles differing in size from that of the weight median diameter.

A distribution where all of the particles are of the same size is termed monodisperse. Such a distribution would plot as a vertical straight line located at the weight median diameter. That is, no particles would differ in size from that of the median diameter.

A polydisperse distribution, on the other hand, contains particle sizes other than that of the median diameter. Furthermore, the wider the distribution, the more particles there are larger than and smaller than the median diameter. A wider distribution is depicted in Figure 3 by the dashed line. A more complete explanation of the particle size distribution can be found in Reference (8).

Composite propellants contain a high loading or weight percent of oxidizer particles so that high values of specific impulse can be achieved. In order to contain a high oxidizer loading, the oxidizer must be made up of several different oxidizer grinds in which the smaller particles can fill the voids between the packing of the larger particles. Thus, it should be clear that propellants contain a polydispersion of oxidizer particle sizes. For those propellants it has been demonstrated (9,10) that above some length scale characteristic of the particle size the arrangement of the particles within the propellant is totally random due to complete mixing during the propellant formulation.

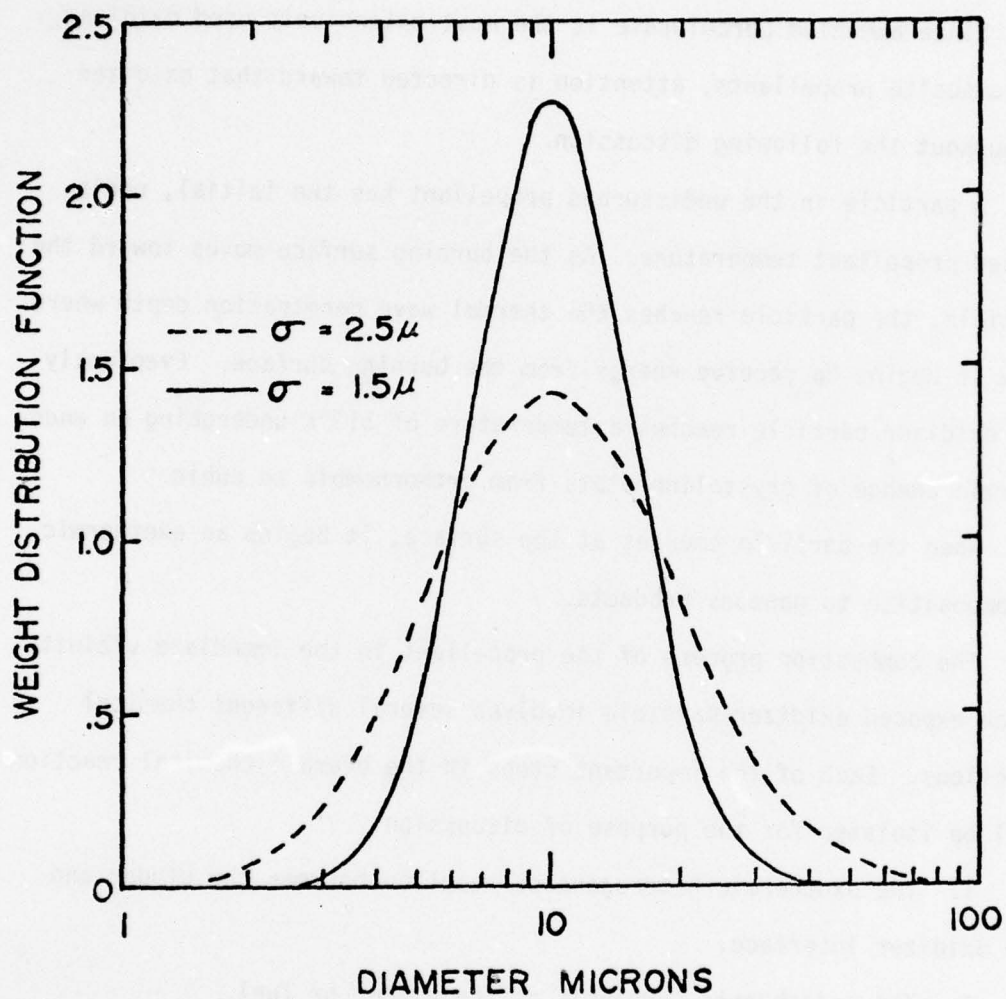


Figure 3. The Effect of the Distribution Width Parameter on the Particle Size Distribution



The combustion process can best be described by following the evolution of one oxidizer particle from deep within the propellant until it emerges at the surface and is consumed in the combustion process.

Since ammonium perchlorate is the most extensively used oxidizer in composite propellants, attention is directed toward that oxidizer throughout the following discussion.

A particle in the undisturbed propellant has the initial, undisturbed propellant temperature. As the burning surface moves toward the particle, the particle reaches the thermal wave penetration depth where upon it begins to receive energy from the burning surface. Eventually the oxidizer particle reaches a temperature of 513°K undergoing an endothermic change of crystalline state from orthorhombic to cubic.

When the particle emerges at the surface, it begins an exothermic decomposition to gaseous products.

The combustion process of the propellant in the immediate vicinity of an exposed oxidizer particle involves several different chemical reactions. Each of the important steps in the overall chemical reaction will be isolated for the purpose of discussion:

1. The exothermic heterogeneous reaction between the binder and the oxidizer interface.
2. The endothermic pyrolysis of the binder or fuel.
3. The exothermic decomposition of the crystal.
4. The monopropellant reaction between the decomposition products of the oxidizer.
5. The exothermic gaseous reaction between the oxidizer decomposition products and the fuel pyrolysis products.

As the oxidizer particle emerges at the burning surface, some of the oxidizer undergoes a heterogeneous subsurface reaction with the surrounding fuel binder (11). There remains, however, a great deal of controversy in the literature pertaining not only to the importance of a subsurface reaction but also to the actual existence of such a reaction.

The strongest case for heterogeneous subsurface reactions comes from ignition studies of Anderson (12,13) and co-workers. In those studies, oxidizers such as fluorine and chlorine trifluoride were used to ignite composite propellants hypergolically. The experiments demonstrated that the ignition process could proceed as a result of spontaneous heterogeneous reactions occurring at the oxidizer-binder interface. However, extensive electron microscope studies at Lockheed (14) on slices of extinguished propellant samples have shown no trace of subsurface heterogeneous reaction. Moreover calculations by Beckstead (14) and co-workers have indicated that heterogeneous subsurface reactions are not required to sustain combustion.

A portion of the fuel or binder surrounding the oxidizer crystal can be associated with that crystal. As the crystal nears the burning surface, the surrounding binder located at the surface pyrolyzes due to the heat transfer to the binder from the various exothermic reactions occurring nearby. The result is the thermal degradation of small fragments of the polymer binder which serve as reactants in the gaseous fuel-oxidizer reaction zone above the burning surface.

At the burning surface the oxidizer initially undergoes a decomposition step from solid crystal to gaseous ammonia and perchloric acid.

The perchloric acid then further decomposes (15) to oxygen, chlorine monoxide, and hydroxyl. The reactions are as follows:



The AP monopropellant flame occurs following the decomposition of the perchloric acid. The AP monopropellant flame is a kinetics controlled reaction between the ammonia (which resulted from the first step in the AP decomposition) and the chlorine monoxide (which resulted from the perchloric acid decomposition). The reaction produces oxygen and inert products.

The final reaction to be considered is the gas phase reaction between the pyrolyzed fuel binder and the decomposed oxidizer. The reaction may result from either or both of two paths. The first is the reaction between the binder pyrolysis products and the perchloric acid from the decomposition of the oxidizer. This results when the perchloric acid and binder pyrolysis products diffuse and mix near the burning surface. The second path is the reaction between the binder pyrolysis products and the products of the AP monopropellant flame. This flame results when the binder pyrolysis products and the products of the AP monopropellant flame diffuse and mix. The heat generation from these two reactions occur at varying distances above the burning surface due to the irregular nature of the propellant burning surface and the inhomogeneities of the reaction zone. Both flames are strongly dependent upon the diffusional mixing of the reactants and, therefore, are very dependent upon the oxidizer particle size.



Quite clearly, the combustion process of composite solid propellants is a very complex situation. Attempts to model this process have evolved from very crude and simple models of the late 50's which only attempt to predict gross trends, to very sophisticated models of the 70's which attempt to predict quantitative results. Of the several models which have attempted to describe the combustion of composite propellants, three models have received the most attention as well as acceptance in the solid propellant propulsion community. Those three models are, in chronological order: the Summerfield Granular Diffusion Flame Model (16), the Heterogeneous Reaction model of Hermance (11,17) and the Multiple Flame Model of Beckstead, Derr and Price (18). A complete description of each of the above models follows.

#### Composite Propellant Combustion Models: Steady State

A comprehensive model which describes the combustion of a solid propellant should be based on the key physical and chemical processes involved in the combustion zone. Those processes should include the heat release and associated kinetics due to steps such as fuel pyrolysis, oxidizer decomposition and gas phase flame reactions including the diffusional mixing process. It should also account for the effect of oxidizer particle size and concentration on propellant burning rate.

#### The Granular Diffusion Flame Model

The granular diffusion flame (GDF) model was formulated by Summerfield (16) to describe the burning characteristics of ammonium perchlorate (AP) based composite propellants and is of historical value since it was the first attempt to model the combustion of composite

propellants. The model was primarily formulated in an attempt to predict the effects of pressure, oxidizer particle size, and the ratio of fuel to oxidizer on the combustion process.

Description of the GDF Model. The physical structure upon which the GDF model is based is presented in Figure 4a. The model is a one dimensional model which assumes that the decomposition process at the propellant surface is controlled by conductive heat feed back from an oxidizer/fuel flame occurring in the gas phase. In the model's original form in 1960 (16), a premixed ammonia/perchloric acid reaction zone (AP monopropellant flame) was assumed to take place at the surface of the propellant followed by a reaction between the oxidizing products from the ammonia/perchloric acid reaction and the fuel products from the pyrolyzed binder.

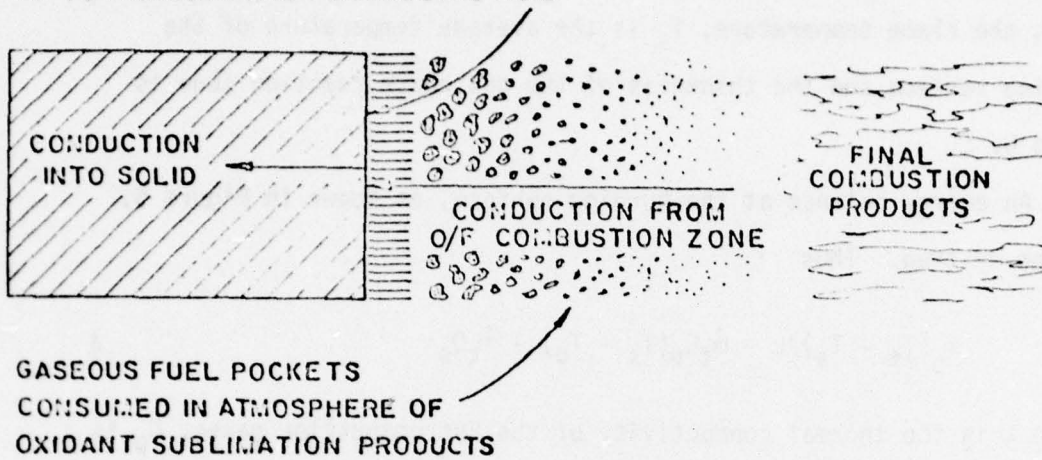
The critical assumption of the model was that vapors of fuel or oxidizer or both are released in the form of pockets of a certain mass content. The average mass content of a pocket was assumed to be much smaller than that of an average oxidizer crystal and to be independent of the temperature and pressure. However, the size of the pockets was assumed to be related to the average oxidizer particle size. The rate at which the pockets are consumed in a chemical reaction as they pass through the flame zone was assumed to be controlled by diffusional mixing and the chemical kinetics. The burning surface was assumed to be dry such that the mixing of the oxidant and fuel occurs only in the gas phase.

Development of the Burning Rate Equation. The propellant burning rate relationship for the GDF model is based on an energy balance at the burning propellant surface. The temperature distribution through

## G D F MODEL

ENDOTHERMIC ZERO-TH ORDER  
PYROLYSIS OF SOLID FUEL AND  
DISSOCIATIVE SUBLIMATION OF  
AP TO AMMONIA AND PERCHLORIC ACID

(a)



(b)

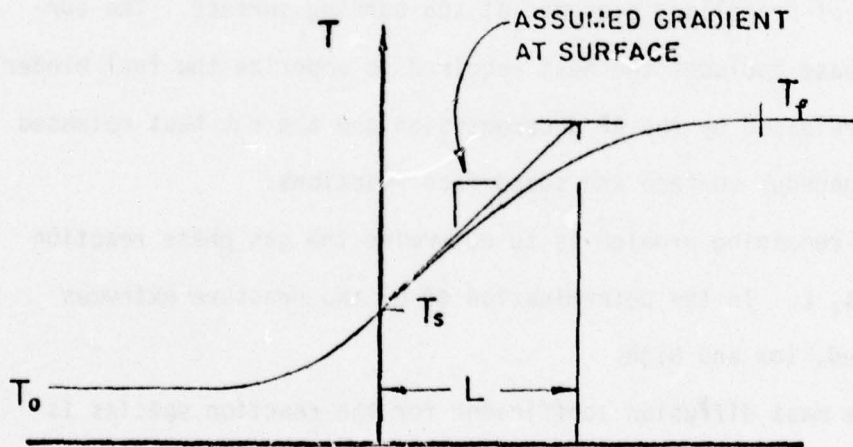


Figure 4. The GDF Physical Description



the propellant and the gas phase reaction zone is presented in Figure 4b. The significant feature of Figure 4b is that a linear temperature profile is assumed in the gas phase reaction zone. Thus, the temperature gradient above the burning surface is given by  $(T_f - T_s)/L$  where  $T_f$  is the flame temperature,  $T_s$  is the average temperature of the burning surface and the thickness of the gas phase reaction zone is given by  $L$ .

An energy balance at the burning surface, as shown in Figure 5, can be written. Thus

$$\lambda_g(T_f - T_s)/L = \dot{m}_t C_p(T_s - T_0) - \dot{m}_t Q_s \quad 3$$

where  $\lambda$  is the thermal conductivity of the hot combustion gases,  $C_p$  is the average specific heat of the propellant,  $T_0$  is the initial temperature of the propellant,  $\dot{m}_t$  is the mass flux of propellant consumed per unit of surface area and  $Q_s$  is the surface heat release per unit area and per pound of propellant consumed at the burning surface. The surface heat release includes the heat required to vaporize the fuel binder, the net heat released by the AP decomposition and the net heat released by the heterogeneous surface and subsurface reactions.

The only remaining problem is to determine the gas phase reaction zone thickness,  $L$ . In the determination of  $L$ , two pressure extremes were considered, low and high.

Since the mass diffusion coefficient for the reaction species is inversely proportional to pressure while the chemical reaction rate is directly proportional to pressure, the molecular diffusion rate is much faster than the chemical reaction rate at low pressure. Thus, at low

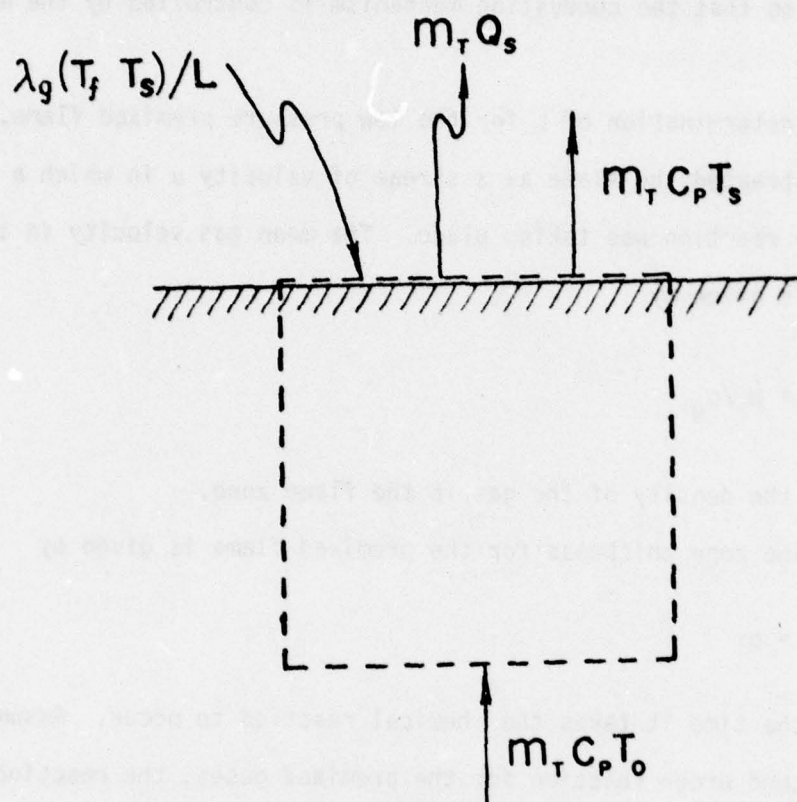


Figure 5. The Summerfield Surface Energy Balance

pressure, the gas phase reaction occurs in a premixed gas and the reaction rate is the controlling mechanism. Conversely, at high pressure the chemical reaction rate is much faster than the intermolecular diffusion rate so that the combustion mechanism is controlled by the mixing process.

In the determination of  $L$  for the low pressure premixed flame, Summerfield treated the flame as a stream of velocity  $u$  in which a second order reaction was taking place. The mean gas velocity in the flame zone is given by

$$u = \dot{m}_t / \rho_g \quad 4$$

where  $\rho_g$  is the density of the gas in the flame zone.

The flame zone thickness for the premixed flame is given by

$$L = u\tau \quad 5$$

where  $\tau$  is the time it takes the chemical reaction to occur. Assuming a global second order reaction for the premixed gases, the reaction time is given by

$$\tau = [(1 - \epsilon)^2 \rho_g A \exp(-E/RT_g)] \quad 6$$

where an Arrhenius expression is assumed for the rate of reaction,  $T_g$  is the average gas phase reaction zone temperature and  $\epsilon$  is a function of the products of reaction, i.e.,  $\epsilon$  is equal to zero at the propellant surface and  $\epsilon$  is equal to unity at the completion of the reaction.

For simplicity, Summerfield assumed that the average value for  $(1 - \epsilon)^2$  over the flame zone is unity. Physically this means that most



of the "overall reaction" takes place near the propellant surface.

Combining equations 4, 5 and 6, yields the following for the flame zone thickness for the low pressure premixed flame:

$$L_1 = \dot{m}_t / [A \exp (-E/RT_g)] \quad 7$$

When equation 3 is solved for the total mass flux and the result substituted into equation 7, the following expression for the thickness of the low pressure flame zone is obtained:

$$L_1 = \frac{\lambda_g (T_f - T_s)}{\rho_g [C_p (T_s - T_o) - Q_s] A \exp (-E/RT_g)} \quad 8$$

For the high pressure diffusion flame, Summerfield assumed that the mass of a pocket could be expressed

$$\mu = \rho_g d^3 \quad 9$$

where  $d$  is the oxidizer particle diameter. The lifetime of a pocket is determined by the rate of gas diffusion to the surrounding flame. The molecular diffusivities of the fuel and the oxidizer are assumed to be the same and are averaged over the gaseous reaction zone. Under these conditions the lifetime of a fuel pocket is

$$\tau = \frac{d^2}{D_g} \quad 10$$

where  $D_g$  is the average diffusivity of the oxidizer and fuel vapors. The thickness of the flame zone is the product of the velocity of the gas stream and the lifetime of the fuel pocket. Thus

$$L_2 = u\tau = \frac{\dot{m}_t}{\rho_g} \frac{d^2}{D_g} \quad 11$$

Combining equations 9 and 11 yields the diffusion flame zone thickness

$$L_2 = \frac{\mu^{2/3} \dot{m}_t}{\rho_g^{5/3} D_g} \quad 12$$

Solving equation 3 for the total mass flux and substituting this into equation 12 yields

$$L_2 = \frac{(\tau_f - \tau_s)^{1/2} \lambda_g^{1/2} \mu^{1/3}}{D_g^{1/2} \rho_g^{5/6} [C_p(\tau_s - \tau_o) - Q_s]^{1/2}} \quad 13$$

Expressions for the flame zone thickness in the two extreme cases can now be written. For the general intermediate case, Summerfield assumed that the flame zone thickness varies with pressure partly as if it were reaction rate controlled ( $L_1$ ) and partly as if it were diffusion controlled ( $L_2$ ), and that the flame zone thickness could be expressed as the sum of the above two. Thus, the general expression for the flame zone thickness becomes

$$L = \frac{\lambda_g^{1/2} (\tau_f - \tau_s)^{1/2}}{[C_p(\tau_s - \tau_o) - Q_s]^{1/2}} \frac{1}{\rho_g [A \exp(-E/RT_g)]^{1/2}} + \frac{\mu^{1/3}}{D_g^{1/2} \rho_g^{5/6}} \quad 14$$

Substituting equation 14 for  $L$  into the energy balance, equation 3, the following expression for the burning rate is obtained:

$$\frac{1}{r} = \left\{ \frac{\rho_p^2 [C_p (T_s - T_o) - Q_s]}{\lambda_g (T_f - T_s)} + \frac{\mu^{1/3} (RT_g)^{5/6}}{p^{1/3}} \right\}^{1/2} \left\{ \frac{RT_g}{P[A \exp(-E/RT_g)]^{1/2}} \right\} \quad 15$$

or by lumping parameters, equation 15 can be simplified to

$$\frac{1}{r} = \frac{a}{p} + \frac{b}{p^{1/3}} \quad 16$$

where a is related to the chemical reaction time and b is related to the diffusion time. Furthermore, all of the parameters which make up the two constants are assumed to be independent of pressure.

Discussion of the GDF Model. Summerfield used equation 16 to correlate experimental burning rate data for a range of styrene base polyester-ammonium perchlorate propellant formulations. The equations provided excellent agreement between theory and experiment in predicting the effect of oxidizer crystal size, fuel to oxidant ratio, and pressure on burning rate.

Although the burning rate equation is empirical in nature and does little more than give a means for curve fitting data, it was the first burning rate equation based on a theoretical premise. Another significant advantage of the Summerfield burning rate expression was that it provided, in a compact equation, a means of estimating the effects of varying the important propellant combustion parameters on burning rate.



The model was later modified by Summerfield et al. (19) to take into account a distended AP monopropellant flame. This was an attempt to make the model applicable to low pressure combustion.

Miller and co-workers (20) extended the GDF model to polydisperse propellants by applying a statistical technique.

#### The Hermance Heterogeneous Reaction Model

The first attempt to develop a model capable of predicting influences on burning rate due to propellant formulation changes was that of Hermance (11).

The model is based on a detailed combination of the steady state decomposition processes of the fuel and oxidizer. The model was first formulated in 1966 and later revised in 1967 (17).

Hermance postulates an exothermic, heterogeneous reaction between the solid fuel and the oxidizer decomposition products and assumes that the gas phase flame position is the sum of the lengths associated with diffusional mixing and chemical reaction. Incorporation of these processes into one-dimensional energy equation allows the calculation of the burning rate as a function of the propellant composition and ambient pressure. Hermance's heterogeneous reaction (HR) model was a significant advance in the state of the art of combustion modeling since it was the first model to deal directly with the heterogeneity of the solid phase by taking into consideration an arbitrary distribution of particle sizes.

Description of the HR Model. The model assumes that the steady state combustion of a composite propellant occurs in three regions; the propellant surface, the gas phase flame zone, and the region between the surface and the flame. The surface chemical processes are

endothermic fuel pyrolysis, exothermic oxidizer decomposition and an exothermic heterogeneous chemical reaction between the fuel binder and decomposed oxidizer in small regions surrounding individual oxidizer crystals. Each of these reactions produces a mass flux from the propellant surface.

In the gas phase flame zone, an exothermic chemical reaction occurs between the oxygen rich products from the decomposed oxidizer and the pyrolyzed fuel. Heat from the flame zone is fed back to the propellant surface by conduction.

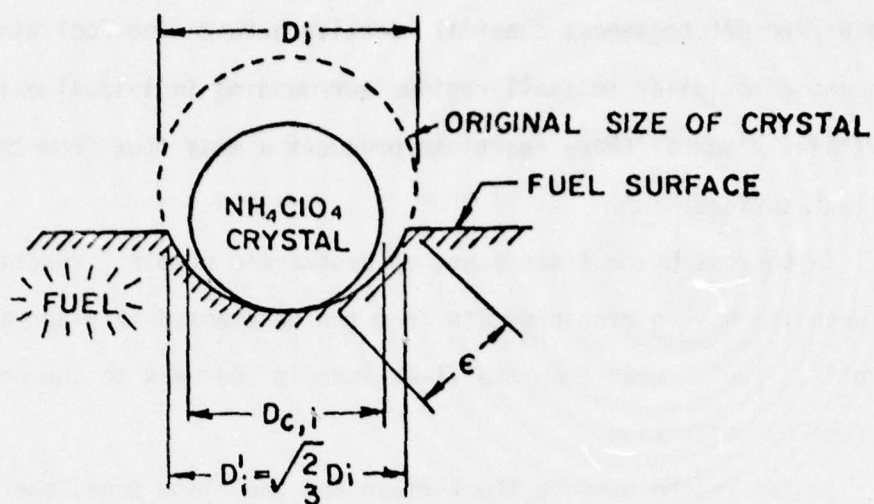
In the region between the surface and the flame zone, the surface decomposition products mix by diffusion and undergo a chemical kinetic delay before ignition at the flame. In the original model (11) only the ignition delay was considered.

The processes depend on the pressure level and/or the temperature at the location of the process and are linked together by the temperature distribution in the gas and solid phases.

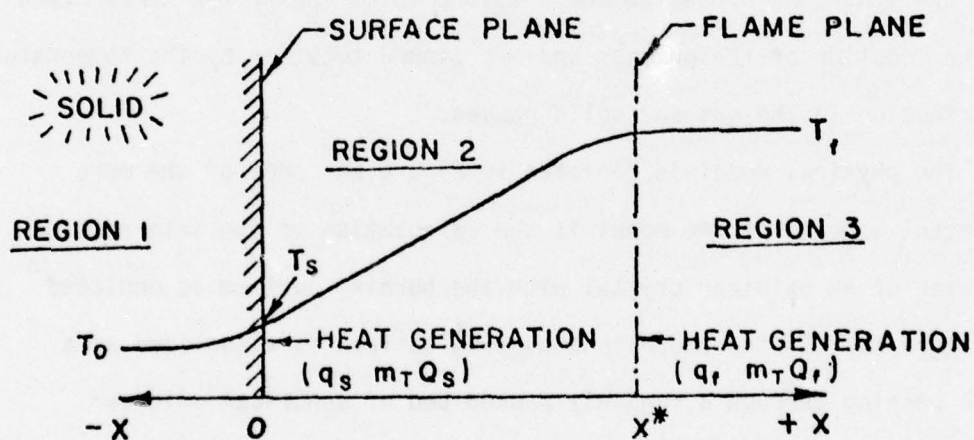
The physical model is depicted in Figure 6a. One of the more important aspects of the model is the calculation of the intersection diameter of an oxidizer crystal with the burning surface as depicted in Figure 6a. If the propellant burning surface is visualized as a plane passing through a randomly packed bed of spherical oxidizer crystals, it can be shown (21) that the statistical average intersection diameter is

$$D_i = \sqrt{2/3} D_o$$

17



A



B

Figure 6. Physical Description of the Hermance Heterogeneous Reaction Model



Development of the Burning Rate Equation. The propellant burning rate can be determined from the total mass flux issuing from the propellant surface. It is the sum of the mass fluxes of gaseous species produced by each of the surface decomposition processes multiplied by the fraction of the total propellant surface area associated with each of the processes. Thus

$$r = \frac{1}{\rho_p} [\dot{m}_f(S_f/S_o) + \dot{m}_{ox}(S_{ox}/S_o) + \dot{m}_{sr}(S_{sr}/S_o)] \quad 18$$

where  $\rho_p$  is the density of the propellant,  $\dot{m}$  is the mass flux and  $S$  is surface area. The subscripts f, ox, o and sr designate fuel, oxidizer, total propellant and surface reaction respectively. Assuming a planar surface, the ratio of fuel and oxidizer surface area to the total propellant surface area can be expressed as a function of the volume fraction of oxidizer in the propellant. Thus

$$\frac{S_f}{S_o} = (1 - \zeta) \quad 19$$

and

$$\frac{S_{ox}}{S_o} = \zeta \quad 20$$

The area on which the surface reaction occurs is calculated by postulating that an oxidizer crystal decreases in size during decomposition as shown in Figure 6a. This size reduction produces a fissure of depth  $\epsilon$  between the oxidizer crystal and the fuel binder which is the region where the heterogeneous reaction takes place. Arrhenius type functions are used to describe the surface regression of both fuel and oxidizer.

The model divides the steady state combustion process of composite propellants into three regions as shown in Figure 6b. The differential form of the energy equation is solved for each region simultaneously. The required boundary conditions result by matching temperature and heat flux at the interface of each section. The analysis results in three equations with three unknowns. They are the burning rate equation, the surface temperature equation and the flame temperature equation. These equations in condensed form are

$$r = a_1 \exp(-E_f/E\theta_s) + \frac{b_1 p^\delta}{\theta_s^{1/2}} \left[ \frac{c_3}{r} - \frac{d_1}{p^m} \right] \exp \left[ \frac{-(E_{ox} + E_{sr})}{E\theta_s} \right] \quad 21$$

$$\theta_s = b_2 + \frac{b_3 p^\delta}{\theta_s^{1/2}} \left[ \frac{c_3}{r} - \frac{d_1}{p^m} \right] \exp \left[ \frac{-(E_{ox} + E_{sr})}{E\theta_s} \right]$$

$$- \frac{a_2}{r} \exp \left( \frac{-E_f}{E\theta} \right) + a_3 \exp(-\xi^*) \quad 22$$

$$\theta_f = \theta_s + a_3 [1 - \exp(-\xi^*)] \quad 23$$

where  $a_1, a_2, a_3, b_1, b_2, b_3, d_1$  are constants containing the physical and chemical properties of the propellants. The burning rate, surface temperature and flame temperature are calculated by numerical iteration using the above three equations.

Discussion of the HR Model. Hermance solved the above three simultaneous equations with a set of input data which represented the combustion properties of a polysulfide - AP composite propellant. He obtained a fairly reasonable fit of the theoretical model to experimental

burning rate data taken over the pressure range from 1 to 400 atmospheres. The model qualitatively predicts the effect of oxidizer particle size on the propellant burning rate at pressures above 200 atmospheres but the model over predicts the effect of initial propellant temperature on burning rate.

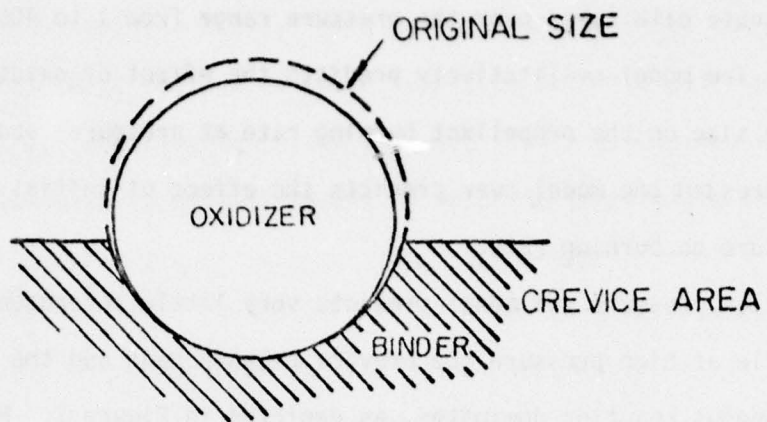
At low pressure the model predicts very little heterogeneous reaction while at high pressure the crevice becomes huge and the heterogeneous reaction dominates, as depicted in Figure 7. Moreover, the calculated surface temperature is almost constant with increasing pressure indicating that the temperature dependent Arrhenius type function will be essentially constant. Thus, the burning rate characteristics predicted by the HR model are determined almost completely by the crevice and its formation. Yet there is no physical evidence to support the formation of a crevice as postulated by Hermance (14).

#### The Beckstead Derr Price Multiple Flame Model

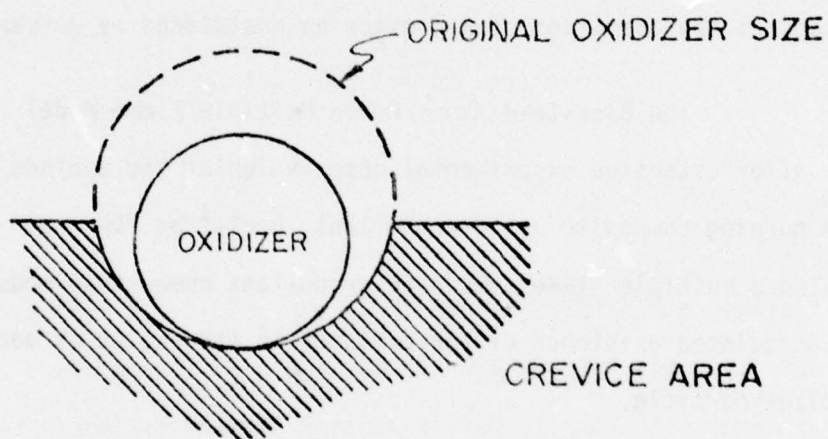
After extensive experimental observation of the surface structure of a burning composite solid propellant, Beckstead, Derr and Price formulated a multiple flame composite propellant combustion model based on the postulated existence of three flames in the region of each exposed oxidizer particle.

Description of the Multiple Flame Model. The model is based on the assumption that the gas-phase heat release can be represented by multiple flames surrounding individual oxidizer crystals. The geometric relationship between the oxidizer crystal and the binder matrix is evaluated statistically as in the Hermance HR model (11). The geometric relationship of the multiple flame is shown in Figure 8. The distance





LOW PRESSURE - VERY SMALL CREVICE AREA



HIGH PRESSURE - VERY LARGE CREVICE AREA

Figure 7. The Pressure Dependence of the Hermance Crevice

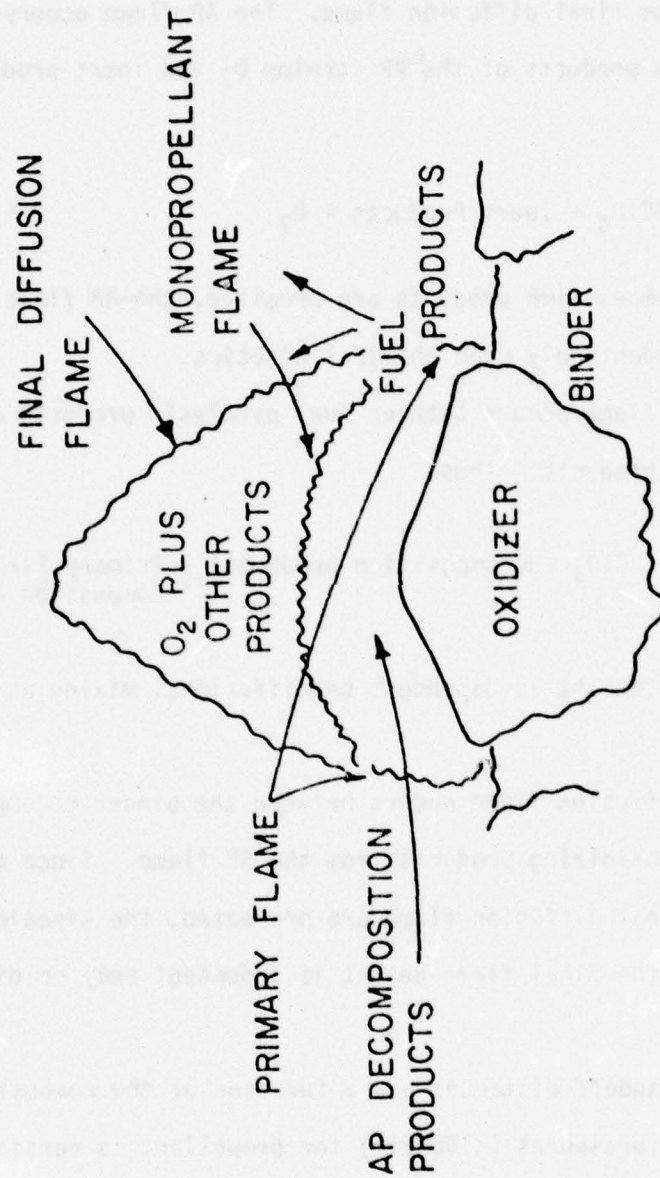
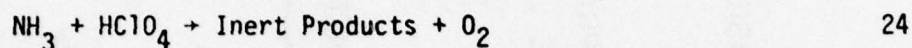


Figure 8. The Flame Structure for an AP Composite Propellant

from the flame to the surface, the standoff distance, is an important consideration in the model.

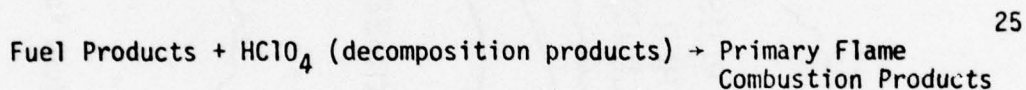
Three flames are considered: the primary flame, the AP monopropellant flame and the final diffusion flame. The AP flame occurs between the decomposition products of the AP forming  $O_2$  and inert products.

Thus



Since the AP decomposition products are premixed, the AP flame standoff distance is dependent only upon chemical kinetics.

The primary flame occurs between fuel pyrolysis products and the AP decomposition products. Thus



The primary flame height is dependent on diffusional mixing as well as kinetics.

The final diffusion flame occurs between the binder decomposition products and the oxidizing products from the AP flame. Since the reactants of the final diffusion flame are preheated, the kinetics are very fast, thus, the final flame height is dependent only on diffusional mixing.

The flame standoff distances are a function of the combustion pressure. At low pressures (<100 atm) the propellant is considered to burn as a premixed flame with the oxidizer and binder decomposition products mixing completely before a reaction occurs. As the pressure



increases, the mixing path length increases, and the reaction path length decreases so that the two reaction paths (ammonia + oxidizing products and binder products + oxidizing products) become competitive. At higher pressures ( $>100$  atm) the ammonia reacts with the oxidizing products before the binder products can diffuse into the oxidizer stream and react. Due to the fuel rich nature of composite solid propellants, a final diffusion flame always occurs above the AP flame. The flame structure variation with pressure is depicted in Figure 9.

At the propellant surface the initial decomposition step of both the binder and the oxidizer is endothermic. However, while still adsorbed on the surface, either set of products can undergo a condensed phase reaction before passing into the gas phase. Products from the surface decompositions then pass into the gas phase and begin mixing and reacting.

The burning surface of the exposed oxidizer particle is assumed to be spherical in shape. Due to an ignition delay, the burning oxidizer surface protrudes above the planar fuel surface at low pressure but is recessed below the planar fuel surface at high pressure. The oxidizer regression is assumed to be the overall rate controlling mechanism, and an overall average temperature is defined for the entire burning surface. In the model's original form, the oxidizer is assumed to be monomodal, monodisperse and spherical. However, the model has since been extended to bimodal and trimodal monodisperse propellants (23,24).

In addition to the above assumptions, radiation heat transfer is neglected, an average value for the solid and the gas phase specific heat is assumed, and the mass diffusion coefficient and thermal

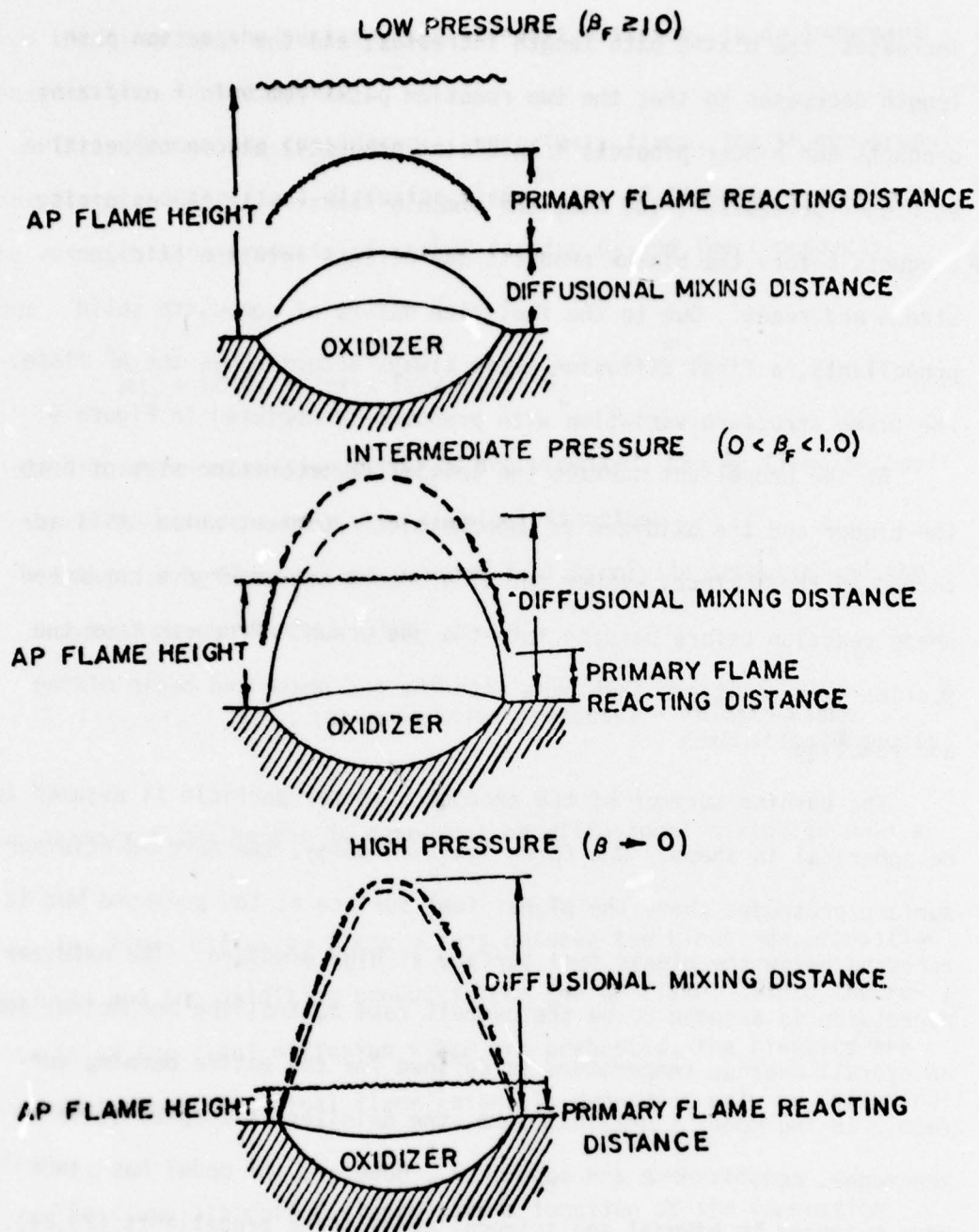


Figure 9. Interaction of Primary Flame and AP Monopropellant Flame at Different Pressures (Dashed Lines indicate hypothetical position)

conductivity of the reacting gases is averaged over the gas phase reaction zone.

Development of the Basic Equations. In the development of the basic equations, the intersection diameter of the statistically average oxidizer particle at the burning surface is (21)

$$D_i = \sqrt{2/3} D_o \quad 20$$

From the equation of continuity for a burning propellant the total mass flux is

$$\dot{m}_t = r \rho_p = \dot{m}_f (S_f/S_T) + \dot{m}_{ox} (S_{ox}/S_T) \quad 26$$

where  $\dot{m}$  is the mass flux,  $r$  is burning rate,  $\rho_p$  is propellant density and  $S$  is the surface area. Subscripts  $f$ ,  $ox$  and  $T$  represent the fuel, oxidizer and total area, respectively. Equation 26 can be simplified further by requiring that stoichiometry be maintained over a long period of time; i.e., the ratio of oxidizer consumption to fuel consumption is equal to the weight ratio of oxidizer to fuel in the propellant. Thus

$$\frac{\dot{m}_{ox} (S_{ox}/S_T)}{\dot{m}_f (S_f/S_T)} = \frac{\alpha}{1 - \alpha} \quad 27$$

The ratio of oxidizer surface area at the burning surface to the total burning surface area is evaluated from geometric relations and from employing the same ignition delay concept used by Hermance. Thus



$$\frac{s_{ox}}{s_T} = \frac{\zeta \left[ 6 \left( \frac{h}{D_o} \right)^2 + 1 \right]}{\left[ 6 \zeta \left( \frac{h}{D_o} \right) + 1 \right]} \quad 28$$

where  $\zeta$  is the volume fraction of oxidizer in the propellant and  $h/D_o$  has the form

$$\frac{h}{D_o} = \frac{1}{2} \left( 1 \pm \frac{1}{\sqrt{3}} \right) \left( 1 - \frac{r_{ox}}{r_f} \right) + r_{ox} \frac{t_{ign}}{D_o} \quad 29$$

The ignition delay is assumed to have the form derived by Shannon (25). Thus

$$t_{ign} = \frac{C_{ign} D_o^{u+1}}{p^m} \quad 30$$

The model utilizes Arrhenius expressions for the mass burning rate of fuel and oxidizer. Thus

$$\dot{m}_f = A_f \exp[-E_f/RT_s] \quad 31$$

and

$$\dot{m}_{ox} = A_{ox} \exp[-E_{ox}/RT_s] \quad 32$$

where  $A$  is the Arrhenius frequency factor,  $E$  is the activation energy  $R$  is the gas constant and  $T_s$  is the average surface temperature. Since the oxidizer regression is rate controlling, the Arrhenius expression for the mass burning rate of fuel is used only in a secondary

sense. That is, it is used for the determination of the area ratio  $(S_{ox}/S_T)$ .

A one-dimensional energy balance at the burning surface as depicted in Figure 10 yields

$$\begin{aligned} \dot{m}_t C_p (T_s - T_o) = & -\dot{m}_{ox} (S_{ox}/S_T) Q_L - \dot{m}_T (S_f/S_T) Q_f + \beta_f Q_{PF} \dot{m}_t \exp(-\xi_{PF}^*) \\ & + (1 - \beta_f) \dot{m}_{ox} (S_{ox}/S_T) [Q_{AP} \exp(-\xi_{AP}^*) + Q_{FF} \exp(-\xi_T^*)] \end{aligned} \quad 33$$

where  $C_p$  is the average specific heat of the gases and the solid, and  $T_o$  is the initial propellant temperature,  $Q_L$  and  $Q_f$  represent the energy required to vaporize the oxidizer and fuel respectively,  $Q_{FF}$ ,  $Q_{AP}$ , and  $Q_{PF}$  represent the energy released in the final flame, and AP flame and the primary flame respectively,  $\beta_f$  is the fraction of reactants that react in the primary flame, and  $\xi_T^*$ ,  $\xi_{AP}^*$  and  $\xi_{PF}^*$  are the nondimensional flame standoff distances for the final flame, AP flame and the primary flame, respectively.

After rearranging equation 33 and combining with equation 27, the equation for the average surface temperature can be written

$$\begin{aligned} T_s = T_o - \alpha Q_L / C_p - (1 - \alpha) Q_f / C_p + (1 - \beta_f) [(Q_{AP} / C_p) \exp(-\xi_{AP}^*) \\ + (Q_{ff} / C_p) \exp(-\xi_T^*)] + \beta_f (Q_{PF} / C_p) \exp(-\xi_{PF}^*) \end{aligned} \quad 34$$

The AP flame heat release is evaluated from the energy balance depicted in Figure 11. Thus

$$Q_{AP} = C_p (T_{AP} - T_o) + Q_L \quad 35$$

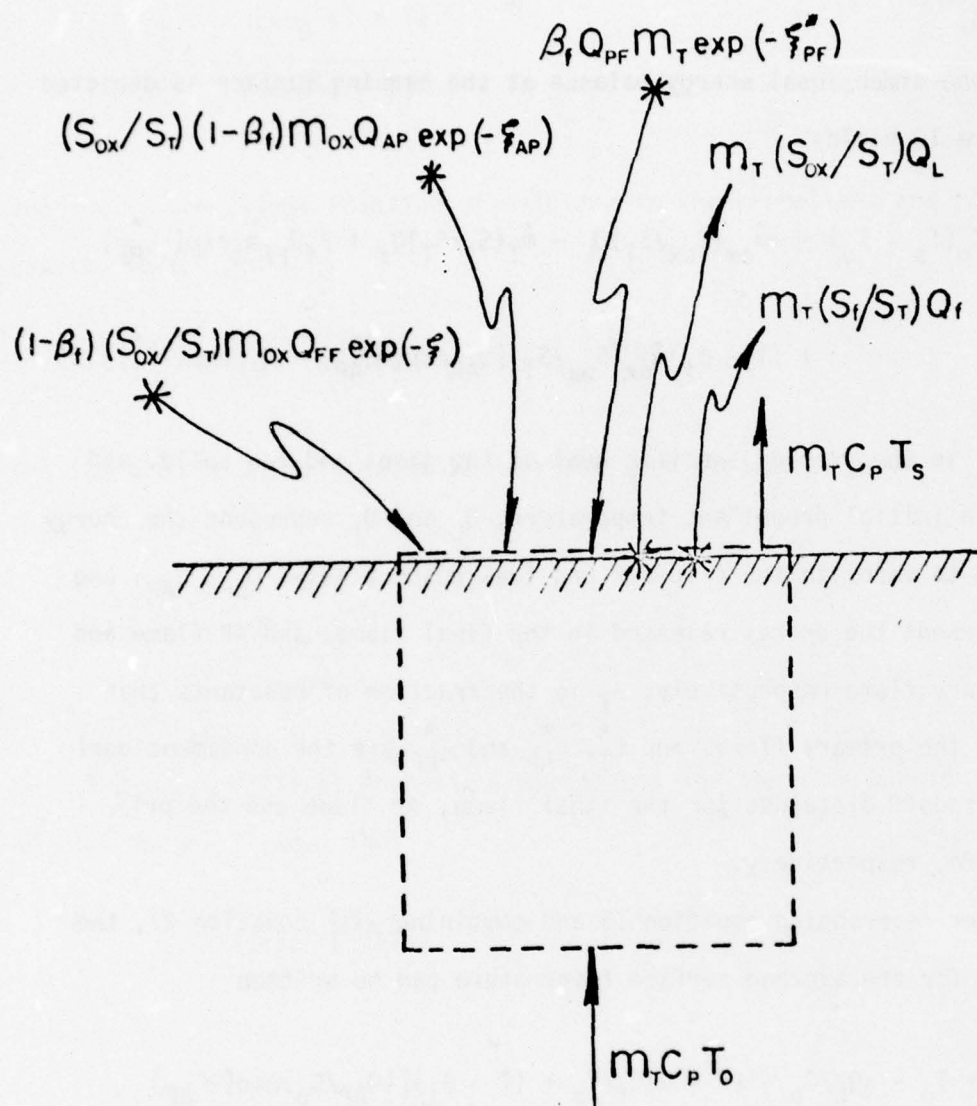


Figure 10. The BDF Surface Energy Balance



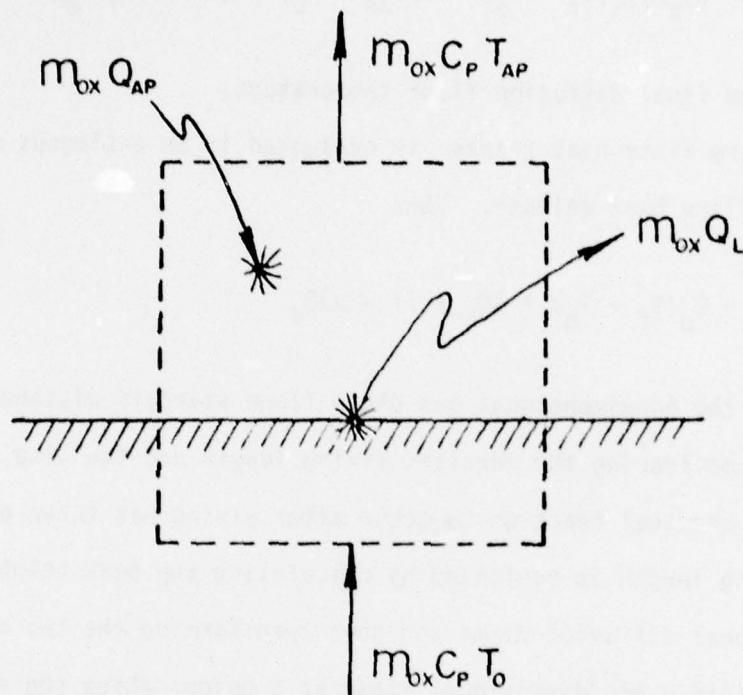


Figure 11. Energy Balance for the AP Flame

where  $T_{AP}$  is the adiabatic AP flame temperature.

The final flame heat release is calculated from an energy balance as depicted in Figure 12. Thus

$$Q_{FF} = (C_p/\alpha)[(T_f - T_o) - \alpha(T_{AP} - T_o) + (1 - \alpha)Q_f/C_p] \quad 36$$

where  $T_f$  is the final diffusion flame temperature.

The primary flame heat release is evaluated in an analogous manner to the final flame heat release. Thus

$$Q_{PF} = C_p(T_f - T_o) + \alpha Q_L + (1 - \alpha)Q_f \quad 37$$

Finally, the nondimensional gas phase flame standoff distances are evaluated by considering the reactant mixing length and the time it takes for the chemical reaction to occur after mixing has taken place.

The mixing length is evaluated by calculating the peak height for a two dimensional diffusion flame and then transforming the two dimensional flame into a one dimensional flame at a height above the surface which is some fraction of the peak height of the two dimensional flame. The height of the one dimensional flame is such that the conductive heat transfer to the surface is approximately the same for the one dimensional flame as for the two dimensional flame.

The chemical kinetic reaction length is evaluated by considering the reaction to take place in a laminar stream moving at some velocity in which a chemical reaction of arbitrary order is taking place.

The AP flame is premixed and is therefore, dependent only on kinetics. The AP flame standoff distance is approximated by

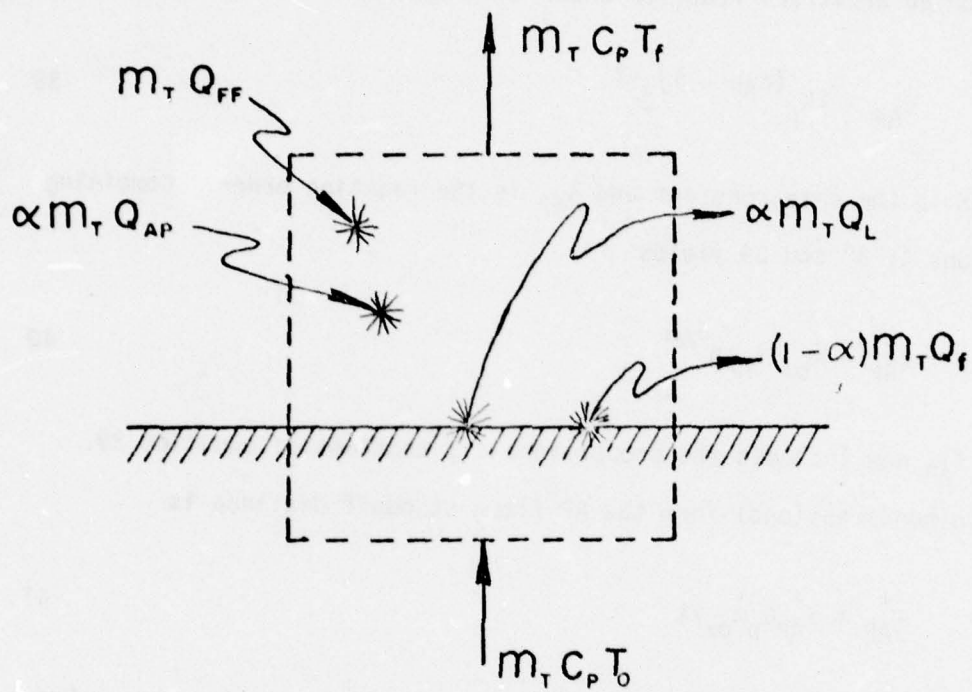


Figure 12. Energy Balance for the Final Flame



$$X^* = u\tau \quad 38$$

where  $X^*$  is the standoff distance,  $u$  is the average gas stream velocity and  $\tau$  is the time it takes for the reactants to react.

For an arbitrary reaction order the reaction time can be written

$$\tau_{AP} \approx [K_p (\delta_{AP} - 1)]^{-1} \quad 39$$

where  $K$  is the rate constant and  $\delta_{AP}$  is the reaction order. Combining equations 4, 38 and 39 yields

$$X_{AP}^* = \dot{m}_{ox} / K_{AP} P^{\delta_{AP}} \quad 40$$

where  $K_{AP}$  now includes the proportionality constant of equation 39.

In nondimensional form the AP flame standoff distance is

$$\xi_{AP}^* = X_{AP}^* C_p \dot{m}_{ox} / \lambda \quad 41$$

where  $\lambda$  is the average thermal conductivity of the reactive and combustion gases.

The reaction distance for the primary flame is evaluated in an analogous manner. Thus

$$X_{PF}^* = \dot{m}_T / K_{PF} P^{\delta_{PF}} \quad 42$$

Burke and Schumann (26,27) solved the differential form of the mass conservation equation for Bunsen burner type of diffusion flame. Because of the similarity of the Bunsen burner to the burning oxidizer

particle in a pyrolyzing fuel/oxidizer matrix, the Burke Schumann analysis was used in the model to determine the diffusion mixing length. The calculated diffusion flame height represents the maximum flame height above the center of the oxidizer crystal. The actual flame shape was not calculated, however, a paraboloid of revolution was assumed for the flame shape.

To avoid the complications of solving a two dimensional heat transfer problem, an average effective flame height was defined,  $A_{fh}$ . The average flame height factor,  $A_{fh}$ , is that fraction of the calculated flame height which corresponds to the distance a one dimensional flame would be from the surface to provide the same energy to the surface as the actual flame. Using this factor the effective heat transfer distance is

$$\bar{x}_D^* = A_{fh} x_D^* \quad 43$$

In the primary flame the components must mix together and then react so that the standoff distance is a diffusional mixing length followed by the distance that it takes the ingredients to react. Thus

$$x_{PF}^* = \bar{x}_{PD}^* + x_{PR}^* \quad 44$$

where  $\bar{x}_{PD}^*$  is the effective mixing length and  $x_{PR}^*$  is the reaction length.

In nondimensional form the primary flame standoff distance is

$$\epsilon_{PF} = (\bar{x}_D^* + x_{PR}^*) C_p m_t / \lambda \quad 45$$

Since a final diffusion flame exists above the AP flame, the final flame standoff distance is composed of the AP reaction distance plus the effective diffusion length for the mixing of the AP flame products and the fuel binder pyrolysis products. Thus

$$X_T^* = (X_{AP}^* + \bar{X}_D^*) \quad 46$$

In nondimensional form, the final flame standoff distance is

$$\xi_T^* = (X_{AP}^* + \bar{X}_D^*) C_{p,ox}^m \lambda \quad 47$$

The only remaining unknown is  $\beta_f$ , the fraction of reactants that react in the primary flame. It was not possible for a rigorous determination of the diffusion flame shape from the Burke-Schumann analysis. Thus, a parabolic shape was assumed for the diffusion flames.

The parameter  $\beta_f$  is determined by assuming that the flow from the oxidizer surface is perpendicular to the planar burning surface. The intersection of the flat AP flame with the parabolic primary diffusion flame can be projected onto the surface of the oxidizer and the area corresponding to each flame determined. The parameter  $\beta_f$  may be considered as that fraction of the AP surface whose products enter the primary flame. This is shown schematically in Figure 13.

The pressure dependence of  $\beta_f$  results from the pressure dependence of the primary and AP flame standoff distances. At low pressures the combined primary flame mixing and reacting distances are less than the AP flame height. Therefore, all of the oxidizing species react directly with the binder products rather than with the ammonia giving a value



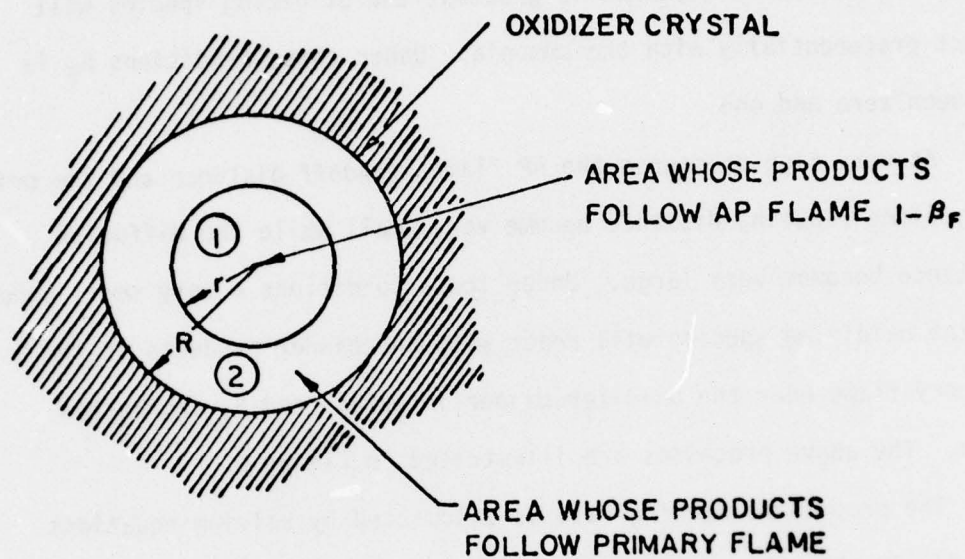


Figure 13. The  $\beta_f$  Determination

of unity for  $\beta_f$ . By increasing the pressure, the AP flame height is reduced, the kinetic distance of the primary flame is reduced and the primary diffusion distance is increased. At higher pressures the diffusion flame intersects the AP flame. Near the center of the crystal where the diffusion distance is greatest the oxidizing species will react preferentially with the ammonia. Under these conditions  $\beta_f$  is between zero and one.

At very high pressures the AP flame standoff distance and the primary flame reacting distance become very small while the diffusion distance becomes very large. Under these conditions a very small amount of the oxidizing species will react with the binder products in the primary flame near the oxidizer binder interface and  $\beta_f$  approaches zero. The above processes are illustrated in Figure 9.

The propellant burning rate is calculated by solving equations 26, 27, 28, 29, 32 and 34, using an iteration procedure.

Discussion of the BDP Model. The purpose of the BDP model was to describe the combustion process of composite propellants in as realistic a manner as possible and then relate the effects of various combustion trends to propellant compositional variations and/or combustion mechanisms. Comparisons were made with a series of unimodal AP-polysulfide propellants. The predicted dependence of burning rate on oxidizer concentration was essentially the same as observed experimentally, while the dependence of the burning rate on the oxidizer particle size was somewhat greater than observed experimentally. The dependence of the burning rate on the initial temperature was found to be in qualitative agreement with the data.

The original BDP model applied solely to an additive free propellant with spherical, monodisperse oxidizer. Cohen, Derr, and Price subsequently extended the model to propellants with aluminum and bimodal oxidizer (24). Beckstead (22,23) has since extended the model to trimodal propellants. However, in all of the above extensions of the model several limitations remain. The limitations will be discussed in detail below.

The first limitation occurs in the calculation of the diffusion flame standoff distances. The original BDP model utilized the Burke-Schumann (26) diffusion flame analysis for the calculation of the diffusion flame standoff distances. The general solution for the position of the diffusion flame front is given by the following series solution:

$$\frac{v-c^2(v+1)}{2(v+1)c} = \sum_{i=1}^{\infty} \left[ \frac{J_1(\phi_i c) J_0(\phi_i \xi)}{\phi_i J_0^2(\phi_i)} \right] \exp \left[ (1 - \sqrt{1 + 4\phi_i^2 \psi^2}) \eta / 2\psi^2 \right] \quad 48$$

where  $v$  is a flame stoichiometry related coefficient,  $\phi_i$  is the  $i^{\text{th}}$  zero of  $J_1$ , a Bessel function of the first kind,  $c$  is the ratio of the oxidizer diameter at the surface to a diameter associated with the fuel binder,  $\psi$  is related to the gas diffusivity, gas velocity and surface geometry, and  $\xi$  and  $\eta$  are nondimensional radial and axial coordinates, respectively.

In the BDP model, only the first term of the series solution is considered. This truncated version of the Burke-Schumann analysis yields the following expression for the nondimensional diffusion flame height  $\eta$ :



$$\eta = -\frac{2\psi^2}{\sqrt{1+4\phi_1^2\psi^2}-1} \ln \left\{ \frac{2(\nu+1)c J_1(\phi_1 c)}{(\nu-c^2(\nu+1)) \phi_1 J_0^2(\phi_1)} \right\} \quad 49$$

for the axial nondimensional coordinate  $\xi$  equal to zero.

Figure 14 depicts the nondimensional standoff distance as a function of the oxidizer volume fraction. The dashed line represents the exact solution to equation 48 while the solid line represents the approximate solution (equation 49). As can be seen, the approximate solution is only valid for over-ventilated flames near stoichiometric conditions.

Real composite propellants, on the other hand, contain oxidizer mass fractions which are much lower than the stoichiometric oxidizer mass fraction. Consequently, substantial errors in the calculated diffusion flame standoff distance may exist. In recent work with the BDP model by Beckstead (22,23), the diffusion flame analysis was replaced by a one-dimensional approximate analysis similar to that of Summerfield (16).

Another limitation of the BDP model involves the assumption of the packing structure for the oxidizer particles. Figure 15 illustrates the packing assumed for the BDP model where each box contains an oxidizer particle and the fuel associated with that oxidizer particle. Letting  $n$  be the number of particles per unit volume, then  $n^{1/3}$  is the number of particles per unit length for the assumed packing structure. It is clear that

$$\delta n^{1/3} + D_i n^{1/3} = 1 \quad 50$$

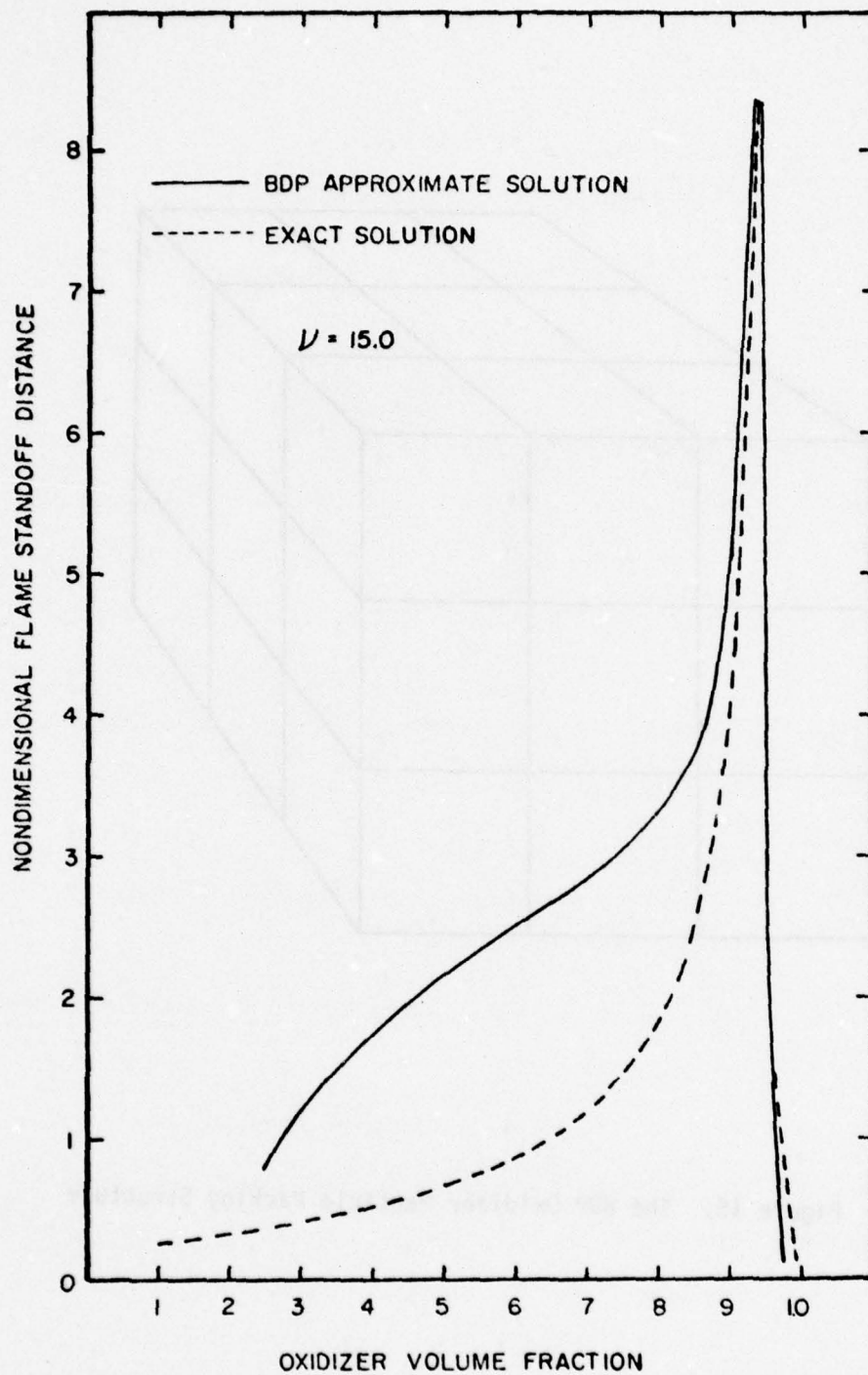


Figure 14. Diffusion Flame Standoff Distance as a Function of Oxidizer Volume Fraction

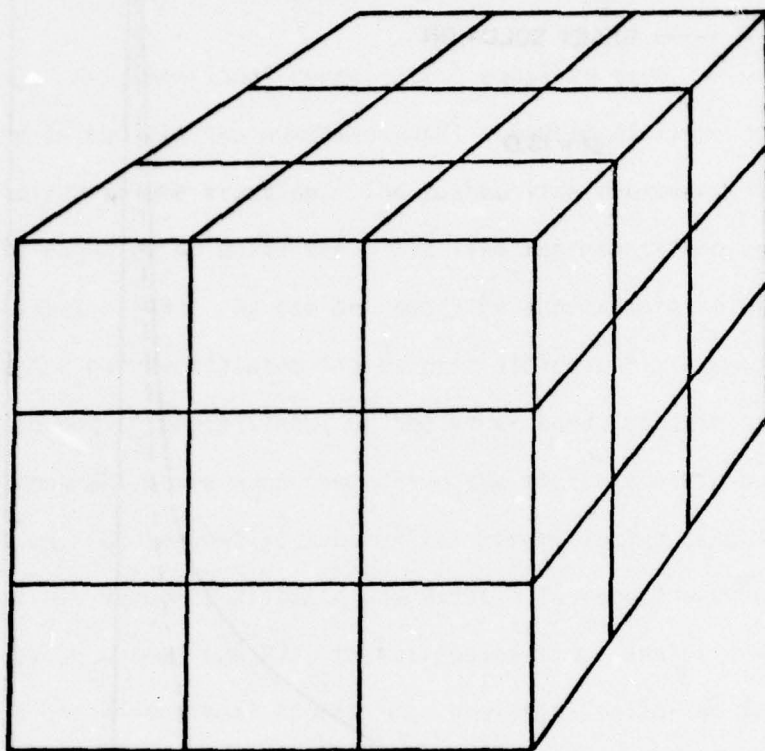


Figure 15. The BDP Oxidizer Particle Packing Structure



where  $\delta$  is the distance between particles at the burning surface and  $D_i$  is the particle intersection diameter at the burning surface. Therefore

$$\delta = 1/n^{1/3} - D_i \quad 51$$

The number of particles per unit volume is

$$n = \frac{\zeta}{V_{ox}} \quad 52$$

where  $\zeta$  is the volume fraction of oxidizer and  $V_{ox}$  is the volume of an oxidizer crystal. Thus

$$n = 6\zeta/(\pi D_0^3) \quad 53$$

Combining equations 20, 51 and 53 yields the following equation for  $\delta$ :

$$\delta = \left(\frac{\pi}{6\zeta}\right)^{1/3} D_0 - \sqrt{2/3} D_0 \quad 54$$

since

$$b = \frac{\delta}{2} + \frac{D_i}{2} \quad 55$$

Combining 51 and 52 yields

$$b = \frac{1}{2} \left(\frac{\pi}{6\zeta}\right)^{1/3} D_0 \quad 56$$

Since the packing structure of composite propellants is not ordered, but rather is a completely random structure, equation 56 for  $b$  is incorrect, for it describes an ordered packing of particles.

This is further illustrated in Figure 16 where  $\delta/D_0$  is plotted as a function of oxidizer volume fraction. Clearly, for oxidizer volume

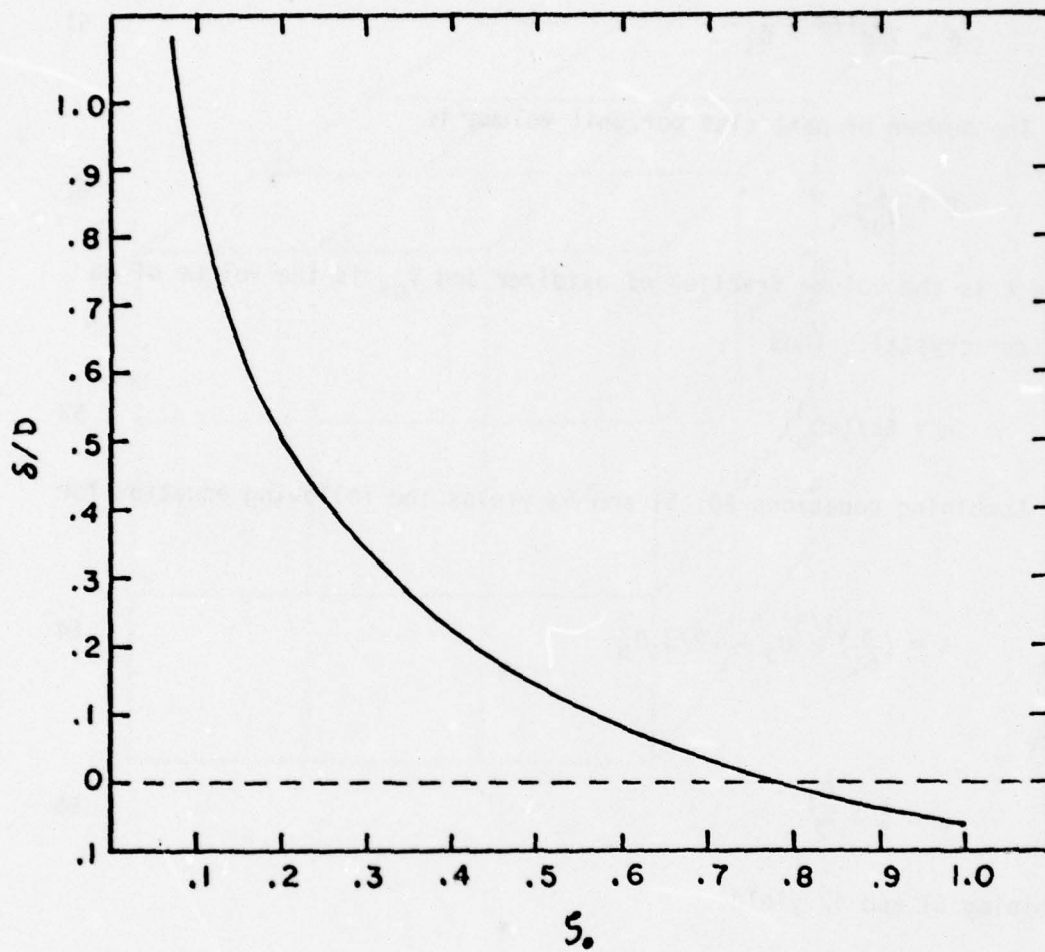


Figure 16. The Ratio of the Distance Between Oxidizer Particles to the Particle Diameter as a Function of Oxidizer Volume Fraction

fractions approaching unity, the ratio  $\delta/D_0$  should approach zero. However, for the BDP method, the ratio of  $\delta/D_0$  actually goes negative at a volume fraction 0.78. This is physically unrealistic.

The final limitation deals with the determination of the mean state of an oxidizer particle undergoing combustion at the burning surface. In the BDP approach, the burning surface is generated mathematically by passing an imaginary plane through a randomly packed monodispersion of spherical oxidizer particles. The mean state in terms of the diameter of particles at the burning surface is assumed to be the average intersection diameter of the particles with the imaginary plane. Since the particles are assumed to undergo an ignition delay, the mean state in terms of the diameter for oxidizer crystals described above is incorrect. A more detailed explanation along with a description of a better determination of the mean state diameter of the oxidizer particle appears in a subsequent section.

#### Description of Erosive Burning

Requirements for ever higher propellant loading in solid propellant rocket motors have led to the development of grain configurations with relatively low port-to-throat area ratios. This, in turn, results in high velocities of propellant combustion gases flowing across the burning propellant surfaces in the aft region of the propellant grains. The presence of a high cross flow velocity over a propellant burning surface causes enhancement of the propellant burning rate and this enhancement of the burning rate is termed erosive burning. For high cross flow velocities the burning rate can be substantially higher than the burning rate of the same propellants not subject to a cross flow velocity.



Moreover, the effects of erosive burning are critical in that the erosive burning rate contributions strongly influence performance level and performance repeatability of propulsion systems.

Since erosive burning is present in many solid propellant propulsion systems and since there is such a strong interaction between the local flow environment and the propellant burning rate, it is necessary to be able to predict this interaction in order to design and calculate the performance of a low port/throat area ratio rocket. At present there is no unifying model which can be used to predict the propellant burning rates under erosive conditions.

#### Experimental Observations of Erosive Burning

There are several general observations of importance which can be attributed to past experimental studies (28-36). A few of the observations follow:

1. Threshold velocities are usually observed, i.e., burning rate is not affected until the core gas reaches a certain velocity.
2. Slower burning propellants are more strongly affected by cross flows than higher burning rate formulations.
3. At high pressure, the burning rate under erosive conditions tends to approach the same value for all propellants (at the same flow velocity) regardless of the burning rate of propellants at zero cross flow.
4. Erosive burning rates do not depend upon the gas temperature of the cross flow.

Most of the above observations were made in systems with cross flow velocities having a Mach number less than 0.3.

### Erosive Burning Models

A large number of erosive burning models have appeared in the literature (37-46). Of those models, all fall into one of four basic categories. They are:

1. Models based on heat transfer from a core gas flowing parallel to the burning surface.
2. Models based on the alteration of transport properties in the region of the gas phase reaction zone.
3. Models based on chemically reacting boundary layer theory.
4. Models based on displacement of the flame by the cross flow.

The only existing model of the third type (45) assumes a homogeneous propellant system. Therefore, since composite propellants are far from homogeneous, no further discussion will be offered for this class of model. The model representative of the 1st type is the Lenoir and Robillard (37) model. Lengellé's (43) erosive burning model is representative of the type two models, and the erosive burning model of King (46) is the only model of the fourth type in existence. A discussion of those three models follows.

#### The Lenoir Robillard Model

Lenoir and Robillard proposed an erosive burning rate law for solid propellants based on the postulate that the erosive component of the burning rate is proportional to the heat transfer rate from the core of the combustion gas stream to the propellant burning surface. A transpiration model for the core gas was used to compute the heat transfer rate.

In the development of the basic equations, it was assumed that the burning rate was dependent upon the amount of heat the propellant receives. The main source of heat was assumed to be from the primary burning zone in the first few microns adjacent to the burning surface. Furthermore, the heat transfer from the primary combustion zone was assumed to be independent of the core gas velocity. The pressure dependence of burning rate was assumed to be controlled by the pressure dependence of the location of the primary combustion zone above the burning surface. As pressure increases, the flame becomes nearer to the surface, heat flow to the burning surface from the flame increases and thus the burning rate increases. A second source of heat was assumed to be from the core of the hot combustion gases. This second source of heat was assumed to act through a convective mechanism and was therefore dependent upon the cross flow gas flow rate. The total burning rate was assumed to be the sum of the two effects, a rate dependent upon pressure and an erosive rate dependent upon combustion gas cross flow rate. Thus,

$$r = r_p + r_e \quad 57$$

The pressure dependent part of the burning rate was assumed to correlate to the well known linear burning rate law

$$r_p = cp^n \quad 58$$

where  $c$  and  $n$  are constants for a particular propellant and are independent of combustion pressure.



The combustion gas cross flow velocity dependent portion of the burning rate was derived by assuming the erosive burning rate to be proportional to the heat transfer coefficient. Thus

$$r_e = kh \quad 58A$$

where  $h$  is the heat transfer coefficient and  $k$  is the proportionality constant. The relationship between the heat transfer coefficient,  $h$ , under conditions of transpiration, to the heat transfer coefficient in the absence of transpiration was expressed in exponential form as

$$h = h_0 \exp(-\beta Q/G) \quad 58B$$

where  $\beta$  is a dimensionless constant,  $Q$  is the mass velocity of the transpiring gas and  $G$  is the mass velocity of the core gas. The heat transfer coefficient under conditions of zero transpiration was assumed to correlate by the Chilton Colburn equation of flow over a flat plate.

$$h_0 = \frac{G^{0.8}}{L^{0.2}} [0.0288 \ C_p^{0.2} \mu^{-0.667}] \quad 58C$$

where  $C_p$  is the specific heat of the combustion gases,  $\mu$  is the viscosity of the combustion gases,  $L$  is the length from the head of the grain, and  $P_r$  is the Prandtl number of the combustion gases. The expression in the brackets of equation 58C was assumed to be insensitive to changes in propellant identity so that the expression in the brackets could be combined with the proportionality constant of equation 58A to form a constant,

$$\alpha = [0.0288 C_p^{0.2} P_r^{-0.667}] k \quad 58D$$

Combining equations 57, 58, 58A, 58B, and 58D, resulted in the following expression for burning rate:

$$r = C P^n + \alpha G^{0.8} / L^{0.2} \exp(-\beta Q/G) \quad 58E$$

The Lenoir Robillard theory has been compared with experimental data and satisfactory agreement indicated. However, the agreement was obtained by matching equation 58E to the experimental data in order to determine the constants  $\alpha$  and  $\beta$ . Thus, the Lenoir Robillard theory is empirical in nature. Furthermore, the model predicts a dependence of burning rate on the mainstream gas temperature. Later experimental work by Marklund and Lake (33) indicated no such dependence. The Lenoir Robillard model has, however, served the test of time and is probably the most widely used model in the solid propellant propulsion community.

#### The Flame Displacement Model

The erosive burning model of King (46) postulates the mechanism for erosive burning to be an enhanced heat transfer to the burning surface. The enhanced heat transfer results from the displacement of the diffusion flames by the cross flow of combustion gases.

The burning rate is hypothesized to be dependent upon the heat feedback from two flame zones. They are the AP monopropellant flame and a diffusion flame between the binder pyrolysis products and the products of the AP monopropellant flame. Thus, the burning rate is

dependent upon three distance parameters associated with the two flames. The three distance parameters considered are the distance from the propellant surface to the average location of the kinetically controlled AP monopropellant heat release, the distance associated with mixing of the oxidizer and fuel for the diffusion flame, and the distance associated with the fuel oxidizer reaction time subsequent to mixing. Those distances are then assumed to be modified in the presence of a cross flow velocity by the following equation:

$$L = L_0 \sin \theta \quad 59$$

where  $L_0$  is the flame standoff distance in the absence of a cross flow and  $\theta$  represents the angle of the average flow vector in the mixing region.

This analysis was combined with an analysis of the boundary layer flow (which gives the cross flow velocity as a function of distance from the propellant surface, mainstream velocity, and propellant burning rate) to permit the calculation of the angle of the average flow vector in the mixing region. The resulting equation for burning rate in the absence of cross flow is

$$r = A_3 P \left[ 1 + \frac{A_4}{1 + A_5 \bar{D}^2 P^2} \right]^{1/2} \quad 60$$

where  $P$  is the pressure and  $\bar{D}$  is the average oxidizer particle size in the propellant. A regression analysis using no-cross flow burning rate data must be performed to obtain best fit values of the constants  $A_3$ ,  $A_4$  and  $A_5$ . The product of  $A_5$  with  $\bar{D}^2$  appearing in burning rate expression may be lumped into one parameter during the regression analysis



such that an average oxidizer particle size need not be defined.

The data of Mickley and Davis (47) were used to develop empirical expressions for the local cross flow velocity as a function of distance from the propellant burning surface, mainstream cross flow velocity, and transpiration rate. The resulting analysis yielded eight equations and eight unknowns for the burning rate of a given composite propellant at a given pressure and cross flow velocity. A computer code was used to solve this system of equations yielding a predicted burning rate for a given pressure, cross flow velocity and set of constant  $A_3$ ,  $A_4$  and  $A_5 \bar{D}^2$ . The model employs no empirical constants other than those from the analysis of the no-cross flow burning rate data.

Discussion of the Flame Displacement Model. King has hypothesized that the flame displacement is due to the cross flow induced distortion of the flow field in the region of the gas phase reaction zone. Inherent in the model is the assumption that transport properties are not affected by the cross flow. Thus, the characteristic kinetic reaction times for the gas phase reactions taking place above the burning surface are the same for both the case of zero cross flow and the case where a strong cross flow is present. However, since the flame is assumed to be conical in shape, the effective distance for diffusional mixing is decreased in the presence of a cross flow velocity. The reduction in the diffusional mixing length is due to a bending of the flame such that its central axis is pointed in a direction parallel to the average velocity vector for the flow of gases near the burning surface. Thus, the flame is "squeezed" such that the radial distance from the central axis of the cone to the outside surface of the cone is reduced. Subsequently, the mixing length is reduced. Thus, the cross flow velocity induced enhancement of

the burning rate is realized by a decrease in the diffusion flame stand-off distance. This effect is exactly the same as the effect due to the enhancement of the diffusion coefficient in the gas phase reaction zone by the presence of a turbulent boundary layer. However, in this case the effect of the turbulence on the thermal conductivity in the gas phase reaction zone was assumed negligible.

#### Lengellé's Erosive Burning Model

The model is based on the combination of Summerfield's (16) granular diffusion flame combustion model with a model for the turbulent boundary layer on a flat plate with injection. The basic assumption adopted was that of a turbulent boundary layer developing above the propellant surface. The transport coefficients of diffusion and heat conduction are then modified in such a way that the heat flux to the surface, and consequently its burning rate, can be enhanced.

The turbulent boundary layer model used in the analysis assumes incompressible flow over a flat plate with injection. The continuity and the momentum conservation equations were simplified by letting  $\frac{\partial u}{\partial x}$  and  $u \frac{\partial u}{\partial x}$  be negligible where  $u$  is the gas velocity parallel to the burning surface. The resulting approximate relationship for the velocity profile is

$$\ln (1 + B\phi) = \eta^n \ln (1 + B) \quad 61$$

where  $B$  is the blowing parameter,  $\phi$  is the ratio of downstream velocity at position  $y$  in the boundary layer to free stream velocity,  $\eta$  is the ratio of  $y$  distance to the boundary layer thickness and  $n$  is the well known empirical velocity profile exponent for the case of no injection.

The implicit relationship for the velocity profile given by equation 61 was awkward for obtaining analytical relations for the turbulent boundary layer parameters. Therefore, the implicit relationship was approximated by the following explicit expression

$$\phi = \eta^\alpha, \quad \alpha = \frac{n(1+B)}{B} \ln(1+B) \quad 62$$

The mixing length hypothesis of Prandtl was combined with the velocity profile given by equation 62 resulting in the following expression for  $\epsilon$ , the coefficient of turbulent diffusivity of momentum:

$$\frac{\rho \epsilon}{\mu} = .16 Re_\delta \alpha \eta^{\alpha+1} \quad 63$$

The average value of the coefficient for turbulent diffusivity of momentum in the flame zone is given by

$$\left(\frac{\rho \epsilon}{\mu}\right)_{ave} = \frac{1}{L} \int_0^L \rho \frac{\epsilon}{\mu} dy = .16 Re_\delta \frac{\alpha}{(2+\alpha)} \left(\frac{L}{\delta}\right)^{\alpha+1} \quad 64$$

where  $L$  is the flame zone thickness and  $Re_\delta$  is evaluated from an approximate expression which relates the ratio of the boundary layer thickness in the case of blowing and the boundary layer thickness in the case of no blowing, to the reduction of the wall shear stress. Thus

$$\frac{C_f}{C_{f0}} = \left(\frac{\alpha}{n}\right)^{0.86} \left(\frac{\delta_0}{\delta}\right)^{0.14} \frac{2(1+\alpha)}{(1+n)} \left[ \frac{B - \log(1+B)}{B^2} \right] \quad 65$$

where

$$\frac{1}{2} C_f = C' \alpha (1+\alpha) \frac{[B - \log(1+B)]}{B^2} \frac{1}{\log(1 + Re_\delta C' \alpha)} \quad 66$$



Lengellé also assumed that the turbulent Lewis and Schmidt numbers are close to unity. Then, the thermal conductivity and mass diffusion coefficient of the combustion gases can be related to the viscosity.

Thus

$$\lambda \approx C_g \rho D \quad 67$$

and  $\rho D \approx \mu (1 + \rho \epsilon / \mu) \quad 68$

where  $\lambda$  is the thermal conductivity,  $D$  is the mass diffusion coefficient and  $\mu$  is the viscosity. Utilizing equations 67 and 68, the transport parameters in the GDF model were expressed in terms of the coefficient for turbulent diffusivity which in turn could be evaluated using equation 63. The resulting expression for burning rate is

$$r = \frac{C_g (T_f - T_s)}{\rho_p Q} \left[ \frac{\mu}{L} + \frac{8.3 \times 10^{-2} \rho_s u_s}{Re_x^{0.1}} \left( \frac{L}{\delta} \right)^{n_\psi} \right] \quad 69$$

where

$$\psi = \frac{\ln(1+B)}{B} \left[ 1 + B \left( \frac{L}{\delta} \right)^\alpha \right] / (2+\alpha) \quad 70$$

$\rho_s$  is the core gas density,  $u_s$  is the core gas velocity and the velocity profile exponent has been approximated by

$$n \approx .52 Re_x^{-0.1} \quad 71$$

The predicted results of the model compared favorably to the experimental results of Marklund and Lake. The appearance of a threshold velocity, below which the normal burning rate is not effected, was

determined to be due to the blocking effect of the transpiring gases. The well known observation that high burning rate propellants give rise to high threshold velocities and low burning rate propellants give rise to low threshold velocities, was also explained on the basis of the blowing parameter.

It should be noted that, although the philosophy behind the erosive burning mechanism of Lengellé's model is sound, the model is little more than a curve fitting device due to the empiricism of the GDF model. It should also be noted that the model is in serious error due to the assumed independence between burning rate and the blowing coefficient. In order for the model to be correct, the value of the burning rate must be determined by an iteration process accounting for the change in the blowing parameter with changes in the burning rate. Thus, the conclusion by Lengellé that the erosive burning effect is additive (i.e., the overall burning rate is the sum of a nonerosive rate and a contribution due to erosive burning) is incorrect.

#### Nonsteady State Combustion

In evaluating a propellant's combustion stability characteristics, there are two parameters of importance: pressure coupled response and velocity coupled response. The pressure coupled response represents the coupling mechanism between the gaseous pressure oscillations and the combustion processes, while the velocity coupled response represents the coupling mechanism between the cross flow velocity transients and the combustion processes. The interaction occurs principally in a relatively thin region near the burning surface.

Following traditional acoustics practice it has usually been assumed for the pressure coupling that the fluctuation of velocity,  $v'$ , normal to the surface is proportional to the fluctuation of pressure  $p'$  at the burning surface. The coefficient of proportionality, in normalized form, is the admittance function,  $A_b$ , for the burning surface. Thus

$$A_b = \bar{M} \left[ \frac{(m'/\bar{m})}{(p'/\gamma \bar{p})} - \frac{(p'/\bar{p})}{(p'/\gamma \bar{p})} \right] \quad 72$$

where  $\bar{M}$  is the average Mach number of the flow leaving the surface,  $\rho$  is the gas density,  $p$  is pressure,  $\gamma$  is the ratio of specific heats and  $m$  is mass flux. The primes denote fluctuating values and the superscript bars denote average values.

The admittance function is, in general, a complex quantity depending on the properties of the materials involved and the frequency of the oscillations. The real part of the admittance function gives that portion of the normal velocity fluctuation which is in phase with the pressure. Thus the attenuation or growth constant for steady waves has a part proportional to the real part of the admittance function such that the waves are driven if the real part of the admittance function is positive. A larger value of the real part of the admittance function implies a greater tendency for combustion to drive the waves.

A similar interpretation of the admittance function arises in connection with the velocity fluctuation  $u'$  parallel to the burning surface. Due to its possible erosive influence on the burning rate the velocity fluctuation parallel to the surface causes a fluctuation of velocity normal to the burning surface.



If one assumes that the oscillations are isentropic the second term in equation 72 is unity and the admittance function becomes dependent only on the value of the first term. The first term, divided by the product  $(M \gamma)$ , is usually referred to as the response function of the propellant and is given the symbol  $R$ . The real part of the response function has the same characteristics as the real part of the admittance function. Thus, waves are driven if the real part of the response function is greater than  $1/\gamma$  and a larger value of the response function implies a greater tendency for the combustion process to drive the waves.

The pressure coupled response is

$$R_p = \frac{(m'/\bar{m})}{(p'/\bar{p})} \quad 73$$

and the velocity coupled response is

$$R_v = \frac{(m'/\bar{m})}{(v'/\bar{v})} \quad 74$$

#### Nonsteady State Models

It is the objective of the nonsteady state combustion models to predict the effect of propellant composition on the propellant response function. In the past, models attempting to describe the nonsteady combustion of propellants (48) have, in general, addressed only homogeneous propellants. Although the homogeneous models have been applied to heterogeneous propellants with a limited degree of success, there is a formidable deficiency in the models. That is, the models are entirely

unable to predict the effect of oxidizer particle size and particle size distribution on the pressure coupled response.

Several of the more pertinent models which have appeared in the literature are: the Denison and Baum (DB) model (49), the Cohen (C) model (51), the Zel'dovich Novozhilov (ZN) model (50) and the velocity coupling model of Lengellé (43). A discussion of these models follows.

#### The Denison and Baum Model

The DB model was an early attempt to model the pressure coupled response of propellants. The model is based upon the solution of the nonsteady energy equation for the solid phase.

The model assumes a quasi-steady gas phase with harmonic pressure oscillations and a planar flame front.

The energy equation for the solid phase is, for the case of no heat generation,

$$\lambda_p (\partial^2 T / \partial x^2) - \bar{m} C_p (\partial T / \partial x) - \rho_p C_p (\partial T / \partial t) = 0 \quad 75$$

The crucial boundary condition is the matching of the heat flux at the solid/gas phase interface.

The resulting expression for the pressure coupled response is

$$\frac{1}{n} (R_{pr} + i R_{pi}) = \frac{AB}{\lambda + (A/\lambda) - (1+A) + AB} \quad 76$$

where  $R_{pr}$  and  $R_{pi}$  are respectively the real and imaginary parts of the pressure coupled response normalized with respect to the burning rate pressure exponent. The parameter,  $\lambda$ , is a complex function of the

nondimensional frequency,  $\Omega$ . The real part of  $\lambda$  is

$$\lambda_r = \frac{1}{2} [1 + (1/\sqrt{2})(1 + 16\Omega^2)^{1/2} + 1]^{1/2} \quad 77$$

while the imaginary part of  $\lambda$  is

$$\lambda_i = [1/2 \sqrt{2}] [(1 + 16\Omega^2)^{1/2} - 1]^{1/2} \quad 78$$

where the nondimensional frequency can be written

$$\Omega = \lambda_p \rho_p \omega / m^2 C_p \quad 79$$

The constants A and B are related to propellant properties. The parameter A is related to the surface pyrolysis

$$A = E_s (1 - T_0/\bar{T}_s) / R\bar{T}_s \quad 80$$

where  $E_s$  is the activation energy associated with the surface pyrolysis,  $T_0$  is the initial propellant temperature,  $\bar{T}_s$  is the average surface temperature and R is the gas constant.

The parameter B is dependent on the temperature sensitivity of the propellant. Thus

$$B = (T_0/\bar{T}_s) / j(1 - T_0/\bar{T}_s) \quad 81$$

where j is the initial temperature index in the burning rate law

$$r = C_p^n T_0^j \quad 82$$



The model must be classified empirical, at most, since the A and B parameters are adjusted for the fitting of experimental data. Furthermore, the model has not met with a great deal of success at fitting the experimental data of composite propellants. This is probably due to the homogeneous nature of the model.

#### The Cohen Model

The most complete attempt at accounting for the oxidizer particle size effects on the pressure coupled response was developed by Cohen et al. (1). Cohen postulated that the combustion response will peak at a frequency given by some characteristic transit time for an oxidizer particle in the condensed phase. Thus

$$f_p \sim \frac{r}{D} \quad 83$$

where  $f_p$  is the frequency at which the response function for a particular mode peaks,  $r$  is the propellant burning rate and  $D$  is the average particle diameter for the mode.

Furthermore, Cohen postulated that the magnitude of the peak response is proportional to the concentration of oxidizer in the propellant. Thus

$$\frac{R_{pp}}{n} \sim \frac{\alpha}{D} \quad 84$$

where  $R_{pp}/n$  is the normalized peak value of the pressure coupled response and  $\alpha$  is the mass fraction of oxidizer in the particular mode.

Cohen assumed that the response function is only a function of propellant type and may be obtained from data for a representative

propellant type. Propellant data for A-13 were used to construct a calibration response function which could then be used to obtain the response function for each weight mean diameter particle size distribution mode in a propellant of interest. The response function of each mode in the propellant was then superimposed to obtain the total propellant response function. This method has potential but is still deficient in that it treats a multimodal polydisperse propellant only as being a multimodal monodisperse propellant.

#### The Zel'dovich Novozhilov Model

The ZN approach to nonsteady modeling employs the same assumptions as those of the DB model. However, the ZN technique allows the pseudo-propellant response functions to be related to steady state propellant combustion parameters in a more realistic manner.

In the derivation of the ZN pressure coupled response the propellant mass flux,  $\dot{m}$ , can be written as a function of burning surface temperature,  $T_s$ , combustion pressure,  $p$ , temperature gradient at the burning surface in the condensed phase,  $f$ , temperature gradient at the condensed/gas phase interface in the gas phase,  $f'$ , and the surface heat release,  $Q_s$ . Thus

$$\dot{m} = \dot{m}(T_s, p, f, f', Q_s) \quad 85$$

Similarly for the surface heat release.

$$Q = Q_s(T_s, p, f, f') \quad 86$$

Conservation of energy at the condensed/gas phase interface yields

$$\kappa f = \kappa' f' + \dot{m} Q_s \quad 87$$

where  $\kappa$  and  $\kappa'$  are the thermal conductivity of the solid and gas respectively.

The mass flux in the gas phase,  $m'$ , can be characterized by the surface temperature, the temperature gradient in the gas phase, the heat release in the gas phase,  $Q'_s$ , and the combustion pressure. The heat release in the gas phase can be characterized by the surface temperature, the temperature gradient in the gas phase and the combustion pressure. Thus the mass flux and heat release can be written

$$\dot{m} = \dot{m}'(T_s, f', Q', p) \quad 88$$

$$Q' = Q'(T_s, f', p) \quad 89$$

Since the gas phase is assumed quasi-steady, mass continuity yields

$$\dot{m}' = \dot{m} \quad 90$$

Thus, there are six equations for seven unknowns:  $f$ ,  $f'$ ,  $T_s$ ,  $Q_s$ ,  $Q'$ ,  $m$  and  $m'$  (the pressure is assumed to be a known function of time). Therefore, it is possible to express any value as a function of pressure and the temperature gradient in the condensed phase at the burning surface. Specifically,

$$\dot{m} = \dot{m}(f, p) \quad 91$$

$$T_s = T_s(f, p) \quad 92$$



Thus,

$$\frac{d\dot{m}}{dt} = \left(\frac{\partial \dot{m}}{\partial f}\right)_p \frac{df}{dt} + \left(\frac{\partial \dot{m}}{\partial p}\right)_f \frac{dp}{dt} \quad 93$$

and

$$\frac{dT_s}{dt} = \left(\frac{\partial T_s}{\partial f}\right)_p \frac{df}{dt} + \left(\frac{\partial T_s}{\partial p}\right)_f \frac{dp}{dt} \quad 94$$

Nondimensionalizing, and taking a first order approximation for the perturbations yields

$$v_1 = \left(\frac{\partial v}{\partial \phi}\right)_\eta \phi_1 + \left(\frac{\partial v}{\partial \eta}\right)_\phi \eta_1 \quad 95$$

$$\psi_1 = \left(\frac{\partial \psi}{\partial \phi}\right)_\eta \phi_1 + \left(\frac{\partial \psi}{\partial \eta}\right)_\phi \eta_1 \quad 96$$

where  $v_1$ ,  $\phi_1$ ,  $\eta_1$  and  $\psi$  are the nondimensional perturbation amplitudes in burning rate, temperature gradient, combustion pressure, and surface temperature respectively.

Equations (95) and (96) provide the means for obtaining the desired functional relation between the burning rate perturbation amplitude and the pressure perturbation amplitude.

With the aid of Jacobians and an energy balance in the condensed phase at the burning surface, the partial derivatives appearing on the right hand side of equations (95) and (96) can be expressed in terms of the following steady state parameters:

$$u = (T_s^0 - T_0) \left( \frac{\partial \ell n r^0}{\partial T_0} \right)_p \quad 97$$

$$v = \left( \frac{\partial T_s^0}{\partial T_0} \right)_p \quad 98$$

$$n = \left( \frac{\partial \ell n r^0}{\partial \ell n p} \right)_{T_0} \quad 99$$

$$\mu = - \frac{1}{(T_s^0 - T_0)} \left( \frac{\partial T_s^0}{\partial \ell n p} \right)_{T_0} \quad 100$$

where the superscript 0 indicates steady state,  $T_s$  is the surface temperature and  $T_0$  is the initial propellant temperature.

The remaining needed relation between the nondimensional burning rate, the nondimensional surface temperature, the nondimensional temperature gradient, and the nondimensional pressure perturbation amplitudes can be determined by solving the linearized energy equation in the solid phase. The result is

$$\psi_1 (1 + 1/Z_1) - \phi_1 Z_1 + i v_1 / \Omega = 0 \quad 101$$

where  $Z_1$  is a complex function of nondimensional frequency given by

$$Z_1 = \frac{1}{2} \left\{ \Omega \left[ \frac{1}{8} (16\Omega^2 + 1)^{1/2} - 1 \right] + i \left[ \frac{1}{8} (16\Omega^2 + 1)^{1/2} - 1 \right] \right\}^{1/2} \quad 102$$

The desired relation between the burning rate perturbation amplitude and the pressure perturbation amplitude can now be written. Thus

$$v_1 = \frac{n + (nv - \mu u)Z_1}{1 - u + (v - iu/\Omega)Z_1} \quad 103$$

Assuming an isentropic fluctuation in the combustion pressure, the response function is defined

$$R_p = \frac{r_1}{r^0} \frac{p^0}{p_1} \quad 104$$

where  $r_1$  and  $p_1$  are the fluctuation amplitude of burning rate and pressure respectively. Thus

$$r_1 = v_1 r^0 \quad 105$$

$$p_1 = \eta_1 p^0 \quad 106$$

Therefore, the pressure coupled response for the ZN technique is

$$R_p = \frac{n + (nv - \mu u)Z_1}{1 - u + (v - iu/\Omega)Z_1} \quad 107$$

Equation 107 can be used to determine a pressure coupled response function by evaluating the steady state parameters for the propellant. The problems with this approach are that some of the steady state parameters can not be evaluated experimentally (specifically those involving the surface temperature) and the assumptions employed in the model break down for heterogeneous propellants when the characteristic thermal wave penetration depth is not much larger than the scale of heterogeneity in the solid phase.



### Lengellé's Model

Lengellé formulated a nonsteady combustion model for velocity coupling based on the linear perturbation of an erosive burning model based upon the GDF combustion model. The erosive burning model was discussed in a prior section of this review and will not be discussed here.

The gas phase reaction zone was assumed to respond quasi-steadily to external oscillations so that only the condensed phase introduced inertia into the process.

The energy equation for the condensed phase with harmonic perturbations was solved for the heat flux penetrating into the solid phase. Thus

$$q_s = C_p \bar{m} [(\bar{T}_s - T_0) + T'_s + \frac{m'}{m} (\bar{T}_s - T_0)/s] \quad 108$$

where  $\bar{T}_s$  is the average surface temperature,  $T_0$  is the initial propellant temperature,  $T'_s$  is the amplitude of perturbation of the surface temperature and  $C_p$  is the propellant specific heat. The parameter  $s$  is

$$s = [1 + (1 + 4i\Omega)^{1/2}]/2 \quad 109$$

where  $\Omega$  is the nondimensional frequency and  $i$  designates an imaginary number.

From the GDF model, with transport properties modified to account for turbulence, the following may be written:

$$q_{+s} \approx C_g(T_f - \bar{T}_s)(\mu + \rho\epsilon)/L \quad 110$$

$$L \approx mM^{2/3}/\rho^{2/3}(\mu + \rho\epsilon) \quad 111$$

$$\rho\epsilon \approx \rho u_e \frac{c'n}{2+n} L \left(\frac{L}{\delta_0}\right)^n \quad 112$$

where the terms were defined in the previous section on erosive burning.

Equations 110, 111 and 112 were then perturbed. The Arrhenius law was also perturbed to relate transient mass flux to transient surface temperature. Thus

$$\frac{m'}{\bar{m}} = \frac{E_s}{R} \frac{T'_s}{\bar{T}_s} \quad 113$$

Combining the perturbed versions of equation 110, 111 and 112 with equations 108, 110, 111 and 112 results in the following relation between pressure and velocity coupling:

$$\frac{1}{R_v} = \frac{1}{0.9\beta AB} \{[s - 1 + A(1/s-1) + ABC'] - (1/3+0.9\beta)AB/R_p\} \quad 114$$

where

$$B = \frac{C_g}{C_p} [\bar{T}_f/(\bar{T}_s - T_0)] [(\bar{T}_f/\bar{T}_s)C(0.5 + \beta) + \frac{1}{6} - 0.9\beta] \quad 115$$

$$C' = 1 + \beta + C(0.5 + \beta)\bar{R}\bar{T}_s/E_s \quad 116$$

$$C = \bar{T}_s/(T_f - \bar{T}_s) + C_g\bar{T}_s/Q \quad 117$$

and  $Q$  is the energy required to heat the propellant to the surface temperature and to transform it into gases. The parameter  $A$  is defined the same as for the Denison and Baum model, i.e., it is related to the surface pyrolysis.

Thus the linearized response of the burning rate of propellants to small pressure and velocity oscillations around a mean turbulent boundary layer flow was obtained. The results of calculations by Lengellé showed that the pressure coupled response is rather strongly amplified when the erosive effect becomes more and more pronounced. The velocity coupled response follows the same trend.

Lengellé's nonsteady state combustion model represents the only attempt to model theoretically the phenomenon of velocity coupling. An important implication derived from Lengellé's work is that erosive conditions must exist before velocity coupling can manifest itself. There exists some disagreement in the solid propellant propulsion community regarding whether or not erosive conditions must be present in order for velocity coupling to occur. This argument is based on claimed evidence of velocity coupling in T-burners operating in the velocity coupled mode in the absence of erosive conditions. The T-burner results are, however, subject to interpretation.

Lengellé's technique offers the most logical and physically plausible mechanism for velocity coupling. The nonsteady model formulated by Lengellé is, however, based on a burning rate model which is primarily empirical in nature and thus leads to a nonsteady model which is empirical in nature and has little predictive capability.



## THE PETITE ENSEMBLE MODEL

### Introduction

Conventional analyses of nonmetalized composite solid propellant combustion are restricted to either one flame or one spatial dimension. Thus, the details of the combustion process that are related to the physical structure of composite propellants are smeared or lost in the analyses and the calculated results are qualitative at best. Statistical analysis of composite propellants combustion, on the other hand, offers the possibility of quantitative results. The history of this approach began when C. E. Hermance (11) combined statistical concepts with a detailed quasi-one dimensional physiochemical model in an analysis of the steady state combustion of composite solid propellants. In this work, statistical concepts were employed to relate the characteristic dimension in the physiochemical model to the oxidizer particle size.

In 1970 Beckstead, Derr, and Price (18) continued the same "statistical plus physiochemical model" approach adopting Hermance's statistics but advancing an improved physiochemical model.

Unfortunately, the Hermance and Beckstead, Derr and Price approaches are questionable on two accounts, the physical validity of replacing the behavior of an ensemble of different flames by that of a single characteristic flame and the statistical process employed to select the characteristic dimension.

In 1970 Miller, Hartman, and Myers (20) overcame the aforementioned problems by assuming that the burning surface was an ensemble of quasi-one-dimensional flamelets. Miller, Hartman and Myers approached the statistical aspect by showing that, for a planar burning surface, the population of particles at the burning surface was the same as in the propellant. Thus, it was assumed that the area associated with each particle size at the surface was related to the distribution of particle sizes in the propellant. The Summerfield GDF model was imbedded in this statistical frame work resulting in a model capable of correlating the effect of oxidizer particle size distribution. The analytical results of this model agree well with experimental data. However, the model is based on an empirical burning rate model. Thus, it is itself empirical.

The statistical formalism presented in this paper was originally conceived by Glick (51). The combining of Glick's statistical frame work with a physiochemical model similar to that of the BDP model was first reported by Glick and Condon (10) in 1974. In that model the macro flame structure above the burning surface of a composite propellant was treated as a collection of different, non-interacting, quasi-one-dimensional flames and the burning surface was treated as a fuel plane dotted with concave and/or convex oxidizer surfaces. The model has been termed the Petite Ensemble Model (PEM). A complete description of the model follows.

#### The Physical Model

The burning surface of a composite propellant can be visualized as a random arrangement of polydisperse oxidizer particles/fuel surface

pairs. A planar section along with an elevation depicting the burning surface of a polydisperse propellant appears in Figure 17. The polydisperse propellant burning surface is comprised of individual oxidizer crystals protruding above or recessed below the planar burning surface depending on the combustion pressure. There exists a distribution of particle sizes at the burning surface due to the random mixing of the various oxidizer particles during the propellant mixing process.

Each oxidizer particle at the burning surface has associated with it some portion of the available fuel at the burning surface. The diffusion flame above the surface consumes the decomposed gaseous AP and fuel binder. As a result, each oxidizer/fuel surface pair will produce a unit flame.

If it is assumed that all oxidizer/fuel surface pairs or unit flames burn independently of each other, the propellant surface can be rearranged into imaginary families of monodisperse propellants (pseudo-propellants) containing one oxidizer type. This rearrangement into subareas is depicted in Figure 18.

Since the burning rate of the propellant is a necessary parameter for both the steady and unsteady models, the burning rate of a polydisperse propellant is calculated from the sum of the monodisperse subarea mass fluxes as determined from an appropriate unit flame combustion model. The unit flame combustion model selected should be capable of predicting the effects of oxidizer size, oxidizer mass fraction, oxidizer volume fraction and pseudopropellant density on the combustion processes of a unit flame. These desired characteristics are satisfied by a highly modified version of the original Beckstead Derr Price (BDP)



AD-A056 892

PURDUE UNIV LAFAYETTE IND SCHOOL OF MECHANICAL ENGI--ETC F/6 21/9.2  
THE EFFECT OF OXIDIZER PARTICLE SIZE DISTRIBUTION ON THE STEADY--ETC(U)  
JUN 78 J A CONDON, J R OSBORN F04611-76-C-0067

UNCLASSIFIED

AFRPL-TR-78-17

NL

2 OF 3

AD  
A056 892



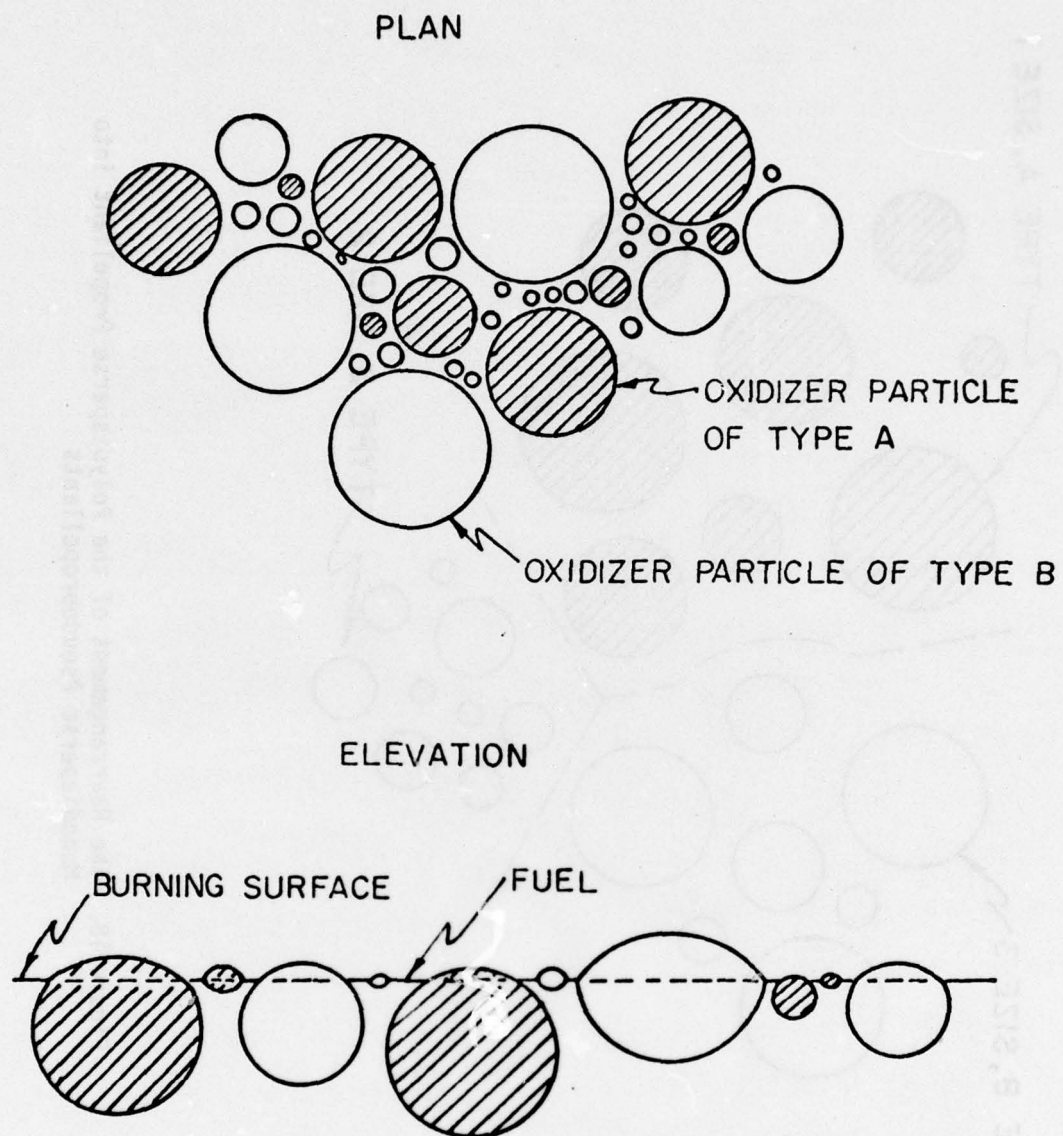


Figure 17. The Packing Structure and Burning Surface of a Polydisperse Propellant

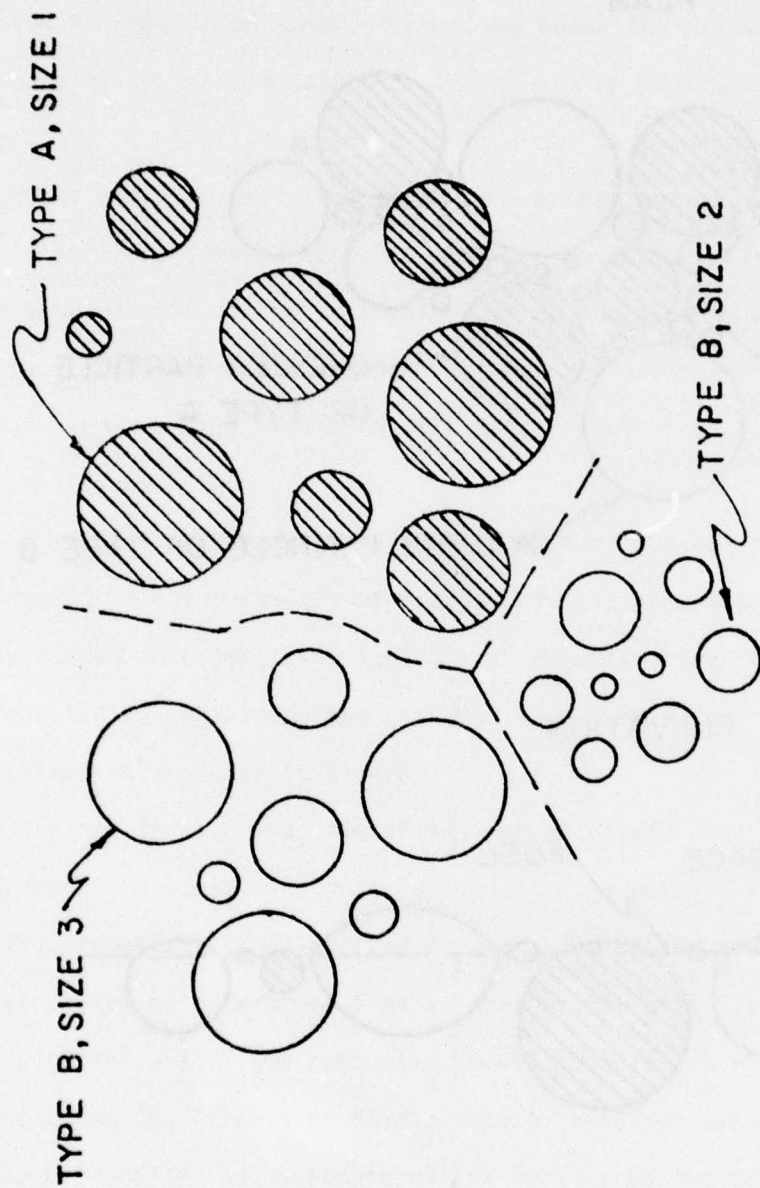


Figure 18. The Rearrangement of the Polydisperse Propellant into Monodisperse Pseudopropellants



multiple flame combustion model (18).

In order to treat the distribution of oxidizer particle sizes on the surface correctly, the statistical formalism for describing the heterogeneous surface structure of composite propellants derived by Glick (51) will be used in deriving the burning rate for the steady state model.

#### The Theoretical Steady State Model

The theoretical model for the steady state combustion of a poly-disperse composite propellant is concerned primarily with specifying a relationship for the burning rate of the propellant as a function of the requisite physical and chemical parameters outlined in the physical model.

#### Derivation of the Statistical Formalism

The derivation is initiated by applying the conservation of mass equation at the burning propellant surface. Thus

$$\bar{m}_t = \int_{S_b} m'' \frac{dS}{S_p} = \bar{r} \rho_p \quad 118$$

where  $\bar{m}_t$  is the average mass flux per unit area from the burning surface  $m''$  is the mass flux per unit surface area,  $S$  denotes surface area,  $\bar{r}$  is the average burning rate,  $\rho_p$  is the propellant density, and the subscripts  $b$  and  $p$  designate burning and planar areas respectively.

The oxidizer particle/fuel surface pairs with common particle diameters and species can be rearranged into pseudopropellants so that those with common particle diameters and species are neighbors. Each oxidizer particle/fuel surface pair is then assumed to burn independently

of all other oxidizer particle/fuel surface pairs. By rearranging the burning surface area into  $Q$  monodisperse pseudopropellants with  $s$  oxidizer types, equation 118 becomes

$$\bar{m}_t'' = \sum_{\ell=1}^Q \left( \sum_{k=1}^S \int_{\Delta S_{b,d,k}} m_{d,k}'' ds \right) / S_p \quad 119$$

where  $\bar{m}_t''$  is the average total mass flux per unit area,  $\Delta S_{b,d,k}$  is the portion of the burning surface occupied by the pseudopropellant and  $m_{d,k}''$  is the mass flux from pseudopropellants possessing oxidizer particles with diameters between  $D_0$  and  $D_0 + dD_0$  and oxidizer specie  $k$ .

Application of the mean value theorem for integrals to the right side of equation 119 yields

$$\bar{m}_t'' = \sum_{\ell=1}^Q \left( \sum_{k=1}^S \bar{m}_{d,k}'' \Delta S_{b,d,k} \right) / S_p \quad 120$$

The mass flux term  $\bar{m}_{d,k}''$  is based on the burning surface area. The mass flux based on the planar area,  $\bar{m}_{p,d,k}''$ , can be written

$$\bar{m}_{d,k}'' \Delta S_{b,d,k} = \bar{m}_{p,d,k}'' \Delta S_{p,d,k} \quad 121$$

where  $\Delta S_{p,d,k}$  is the projection of the monodisperse pseudopropellant burning subarea  $\Delta S_{b,d,k}$  on the propellant planar surface.

If  $\Delta N_{p,d,k}$  is the number of oxidizer particles on  $S_p$ , the planar surface, having diameters between  $D_0$  and  $D_0 + dD_0$  and oxidizer specie  $k$  per unit planar area, then

$$\Delta S_{p,d,k} / S_p = \bar{\Delta S}_{p,d,k} \Delta N_{p,d,k} \quad 122$$

where  $\Delta \bar{S}_{p,d,k}$  represents the average value.

A distribution function,  $F_{p,d,k}$ , can be defined such that

$$dN_{p,d,k} = N F_{p,d,k} dD_o \quad 123$$

where  $N$  is the total number of particles on the burning surface.

Combining equations 120 through 123 yields

$$\bar{m}_t'' = N \sum_{k=1}^S \left( \sum_{\ell=1}^Q \bar{m}_{p,d,k}'' \Delta \bar{S}_{p,d,k} F_{p,d,k} \Delta D_o \right) \quad 124$$

Evaluating the sum over all  $\ell$  as  $Q \rightarrow \infty$  yields

$$\bar{m}_t'' = N \sum_{k=1}^S \int_{D_o} \bar{m}_{p,d,k}'' \Delta \bar{S}_{p,d,k} F_{p,d,k} dD_o \quad 125$$

Equation 125 is the statistical formalism that enables the mean burning rate of a propellant with several different polydisperse oxidizers to be computed from the mean burning rates of a sequence of monodisperse pseudopropellants assuming the combustion of each unit flame to burn independently of adjacent ones. The above development permits consideration of the real propellant having an oxidizer size distribution as well as having several different oxidizers. It represents an improvement over the conventional requirement that a single particle be selected to represent a polydispersion of oxidizer particle sizes.

Equation 125 is not, however, in a useful form since the average planar surface area of a pseudopropellant subarea,  $\Delta \bar{S}_{p,d,k}$ , and the distribution function,  $F_{p,d,k}$ , have not been related to propellant formulation variables. Moreover, relations for the pseudopropellant properties: oxidizer mass fraction, oxidizer volume fraction and



pseudopropellant density must be formulated since they along with oxidizer particle size, determine the mass flux,  $m_{d,k}^*$ , emanating from a pseudopropellant subarea.

In order to derive the above relations the mean statistical characteristics of the fuel surface in each monodisperse subarea must be determined. This requires that a statistical determination be made of the arrangement of the smaller particles inside the packing of the larger particles. Such information is unavailable. However, an examination of the characteristics of regular geometric packings (52) suggests that the mean volume of fuel associated with a particle should be roughly proportional to its surface or

$$\Delta \bar{V}_{f,d} \propto D_0^2 \quad 126$$

where  $\Delta \bar{V}_{f,d}$  is the average volume of fuel associated with an oxidizer particle of diameter between  $D_0$  and  $D_0 + dD_0$ . To permit some variation of fuel volume for a sphere, it will be assumed that

$$\Delta \bar{V}_{f,d} = C D_0^n \quad 127$$

where  $C$  is the proportionality constant and  $n$  is an empirical constant. Once a value is assumed for  $n$ ,  $C$  can be determined in terms of propellant formulation variables and pseudopropellant properties by considering conservation of mass.

Since particle diameter alone is important in a packing, the average volume of fuel associated with an oxidizer particle is independent of the composition. Thus

$$\Delta \bar{V}_{f,d,k} = \Delta \bar{V}_{f,d} \quad 128$$

Finally, the volume fraction of fuel associated with particles having diameters between  $D_0$  and  $D_0 + dD_0$  and oxidizer type  $k$  is

$$dV_{f,d} = \Delta \bar{V}_{f,d} dN_{v,d} \quad 129$$

where  $dN_{v,d}$  is the number of oxidizer particles per unit volume with diameters between  $D_0$  and  $D_0 + dD_0$ .

Similarly, the volume fraction of oxidizer particles with diameters between  $D_0$  and  $D_0 + dD_0$  is

$$d\zeta = \Delta \bar{V}_{o,d} dN_{v,d} \quad 130$$

and the mean volume of oxidizer particles with diameters between  $D_0$  and  $D_0 + dD_0$  is

$$\Delta \bar{V}_{o,d} = \pi D_0^3 / 6 \quad 131$$

Combining equations 130 and 131, the number of oxidizer particles per unit volume with diameters between  $D_0$  and  $D_0 + dD_0$  can be written

$$dN_{v,d} = 6d\zeta / \pi D_0^3 \quad 132$$

If the fraction of particles with diameters between  $D_0$  and  $D_0 + dD_0$  and oxidizer type  $k$  in the propellant is  $\eta_{d,k}$ , the number of these particles per unit planar surface area is

$$dN_{p,d,k} = (6/\pi D_0^3) \eta_{d,k} d\zeta_d = (6/\pi D_0^3) d\zeta_{d,k} \quad 133$$

The total volume fraction of fuel is  $(1-\zeta)$  where  $\zeta$  is the total volume fraction of oxidizer. The total volume fraction of fuel is also given by the integral of equation 129 over all oxidizer particle diameters. Thus

$$(1-\zeta) = \int_{D_0} dV_{f,d} \quad 134$$

Employing equations 127, 129, 131, 132, and 134 and rearranging yields an expression for the proportionality constant  $C$ .

$$C = \{\pi(1-\zeta)/6\} / \int_{D_0} D^{n-3} d\zeta_d \quad 135$$

With both particle diameter and mean volume of fuel associated with that particle diameter known, the volume and mass fractions and the density of a pseudopropellant formed from an oxidizer particle/fuel surface pair can now be computed. The pseudopropellant volume fraction of oxidizer is

$$\zeta_{d,k}^* = \Delta \bar{V}_{o,d,k} / (\Delta \bar{V}_{o,d,k} + \Delta V_{f,d,k}) \quad 136$$

Thus

$$\zeta_{d,k}^* = (1 + 6CD^{n-3}/\pi)^{-1} \quad 137$$

The mass fraction of oxidizer is

$$\alpha_{d,k}^* = \Delta \bar{V}_{o,d,k} \rho_{o,k} / (\Delta \bar{V}_{o,d,k} \rho_{o,k} + \Delta \bar{V}_{f,d,k} \rho_F) \quad 138$$



Thus

$$\alpha_{d,k}^* = \{1 + 6C_p D_0^{n-3} / \pi \rho_{o,k}\}^{-1} \quad 139$$

and the pseudopropellant density is

$$\rho_{d,k}^* = \rho_{p,k} \zeta_{d,k}^* / \alpha_{d,k}^* \quad 140$$

The above pseudopropellant properties ( $\alpha_{d,k}^*$ ,  $\zeta_{d,k}^*$ , and  $\rho_{d,k}^*$ ) along with the particle diameter,  $D_0$  are used in the unit flame combustion model to determine the mass flux ( $\bar{m}''_{p,d,k}$ ) emanating from the pseudopropellant subareas.

In order to relate the average planar surface area of a pseudopropellant subarea,  $\Delta \bar{S}_{p,d,k}$ , to propellant properties, it is first necessary to consider the statistical characteristics of the intersection of a plane with a randomly packed polydispersion of spheres. It can be shown that the mean statistical characteristics of the intersection of a plane with a randomly packed polydispersion of spheres is the same as that for a randomly packed monodispersion of spheres. Namely, if one considers all particles being intersected that have diameters between  $D_0$  and  $D_0 + dD_0$ , the Blum and Wilhelm (21) mean intersection diameter applies. Thus

$$\bar{D} = \sqrt{2/3} D_0 \quad 141$$

where  $\bar{D}$  is that mean intersection diameter.

The average oxidizer particle intersection diameter can now be determined. Thus,

$$\Delta \bar{S}_{o,d,k} = \pi D_o^2 / 6 \quad 142$$

Since the volume fraction of oxidizer in the pseudopropellant subarea is

$$\zeta_{d,k}^* = S_{o,d,k}^* / S_{p,d,k}^* = \Delta \bar{S}_{o,d,k} / \Delta \bar{S}_{p,d,k} \quad 143$$

equation 142 becomes

$$\Delta \bar{S}_{p,d,k} = \pi D_o^2 / 6 \zeta_{d,k}^* \quad 144$$

Equation 144 provides the necessary relationship for determining the average planar surface area of a pseudopropellant subarea with oxidizer particles having diameters between  $D_o$  and  $D_o + dD_o$  and for oxidizer species  $k$ .

During the derivation of the expressions for the pseudopropellant properties a new unknown,  $d\zeta_{d,k}$ , the volume fraction of oxidizer having particle sizes between  $D_o$  and  $D_o + dD_o$ , was introduced. It now becomes necessary to relate  $d\zeta_{d,k}$  and the only other remaining unknowns  $F_{p,d,k}$  (the distribution function) and  $\rho_t$  (the propellant density) to the independent propellant formulation variables  $\alpha_{k,j}$ , the mass fraction of oxidizer of specie  $k$  and mode  $j$ ,  $F_{k,j}$  the distribution function of oxidizer particle size of oxidizer specie  $k$  and mode  $j$ ,  $M_k$  the number of modes for specie  $k$  and  $s$  the number of oxidizer species.

The volume fraction of oxidizer specie  $k$  having diameters between  $D_o$  and  $D_o + dD_o$  is defined

$$d\zeta_{d,k} = dV_{o,d,k} / V_t \quad 145$$

Since

$$dV_{o,d,k} = dm_{o,d,k} / \rho_{o,k} \quad 146$$

and

$$V_t = m_t / \rho_t \quad 147$$

Combining equations 145, 146, and 147 yields

$$dz_{d,k} = (dm_{o,d,k} / m_t) (\rho_t / \rho_{o,k}) \quad 148$$

The distribution function can be defined

$$F_{k,j} = dm_{o,d,k,j} / (m_{o,k,j} dD_o) \quad 149$$

where the element of mass of oxidizer of specie k and mode j and of sizes between  $D_o$  and  $D_o + dD_o$  is

$$dm_{o,d,k} = \sum_{j=1}^{M_k} dm_{o,d,k,j} \quad 150$$

Combining equations 148, 149, and 150 yields

$$dz_{d,k} = (\rho_t / \rho_{o,k}) \sum_{j=1}^{M_k} \alpha_{k,j} F_{k,j} dD \quad 151$$

Since the volume of oxidizer with diameters between  $D_o$  and  $D_o + dD_o$  is given by the summation of volumes associated with each specie, then

$$dz_d = \sum_{k=1}^S (\rho_t / \rho_{o,k}) F_k dD \quad 152$$



where

$$F_k = \sum_{j=1}^{M_k} F_{k,j} \alpha_{k,j} \quad 153$$

The volume fraction of oxidizer is

$$\zeta_o = V_o/V_t \quad 154$$

but

$$V_o = \sum_{k=1}^S \sum_{j=1}^{M_k} V_{o,k,j} \quad 155$$

Combining equations 147, 154, and 155 yields

$$\zeta_o = \rho_t \sum_{k=1}^S \sum_{j=1}^{M_k} (V_{o,k,j}/m_t) \quad 156$$

Since

$$\zeta_{k,j} = m_{o,k,j}/m_t \quad 157$$

and

$$\rho_{o,k} = m_{o,k,j}/V_{o,k,j} \quad 158$$

Combining equations 155, 157, and 158, the volume fraction of oxidizer can be written

$$\zeta_o = \rho_t \sum_{k=1}^S \sum_{j=1}^{M_k} (\alpha_{k,j}/\rho_{o,k}) \quad 159$$

The propellant density can be written as follows:

$$\rho_t = m_t/V_t \quad 160$$

where

$$V_t = \sum_{k=1}^S \sum_{j=1}^{M_k} V_{o,k,j} + V_f \quad 161$$

Since

$$\rho_t = \left\{ \sum_{k=1}^S \sum_{j=1}^{M_k} (V_{o,k,j}/m_t) + (V_f/m_t)(m_f/V_f \rho_f) \right\}^{-1} \quad 162$$

Combining equation 162 with equations 157 and 158 and noting that

$$(1 - \alpha) = m_f/m_t \quad 163$$

yields

$$\rho_t = \left\{ \sum_{k=1}^S \sum_{j=1}^{M_k} \alpha_{k,j}/\rho_{o,k,j} + 1/\rho_f + \alpha/\rho_f \right\}^{-1} \quad 164$$

but

$$\alpha = \sum_{k=1}^S \sum_{j=1}^{M_k} \alpha_{k,j} \quad 165$$

Therefore

$$\rho_t = \left\{ 1/\rho_f + \sum_{k=1}^S \sum_{j=1}^{M_k} (1/\rho_{o,k} - 1/\rho_f) \alpha_{k,j} \right\}^{-1} \quad 166$$

Employing equations 123, 133, 144, and 152, equation 125 can be re-written

$$\bar{m}_t'' = \rho_t \sum_{k=1}^S \rho_{o,k}^{-1} \int_{D_o} (\bar{m}_{p,d,k}'' / \zeta_{d,k}^*) F_k dD \quad 167$$

Therefore

$$\bar{r} = \sum_{k=1}^S \rho_{o,k}^{-1} \int_{D_o} (\bar{m}_{p,d,k}'' / \zeta_{d,k}^*) F_k dD_o \quad 168$$

Equation 168 expresses the polydisperse propellant burning rate in terms of propellant formulation variables and the mean state subarea mass fluxes.

In order to implement the computation indicated by equation 168, it is necessary to specify a mathematical relationship for the distribution function,  $F_k$ , representing the distribution of oxidizer particle sizes.

A log normal distribution was selected as representative of the particle size distribution. The assumption of a log normal distribution permits each particle size distribution to be characterized by two parameters: the weight median diameter,  $\bar{D}$ , of particles in the distribution mode and a parameter,  $\sigma$ , which reflects the width of the distribution of particle sizes about the weight median diameter of particles in the mode.

The log normal distribution may be represented by the following relationship:

$$y = 1/(\sigma \sqrt{2\pi}) \exp \left[ -1/2 \left( \frac{x-\bar{m}}{\sigma} \right)^2 \right] \quad 169$$



where

$$x = \ln D \quad 170$$

$$m = \ln \bar{D}_m \quad 171$$

$$\sigma = \ln \sigma^* \quad 172$$

$$y = F_{k,j} D_0 \quad 173$$

Thus, the weight percent of particles less than a given diameter is

$$\left(1/(2\pi\ln\sigma)\right) \int_0^D \frac{1}{D} \exp \left[ -\frac{1}{2} \left( (\ln D - \ln \bar{D}) / \ln \sigma \right)^2 \right] dD \quad 174$$

This two parameter method of representing the particle size distribution of a mode is in excellent agreement with experimental particle size data for most oxidizer grinds.

Figure 19 depicts a comparison of the log normal distribution to particle size measurements made by Miller (6,7) for several different particle size distribution modes. The standard deviations of the experimental data from the log normal distributions which result when the weight percent of particles less than a diameter is plotted as a function of particle diameter was never more than 3.1% and on the average was only 1.7%. Thus, it is apparent that the log normal approximation is in good agreement with the actual distribution.

The formalism has now been written for computing the burning rate of a polydisperse composite propellant given the average mass flux from each pseudopropellant.

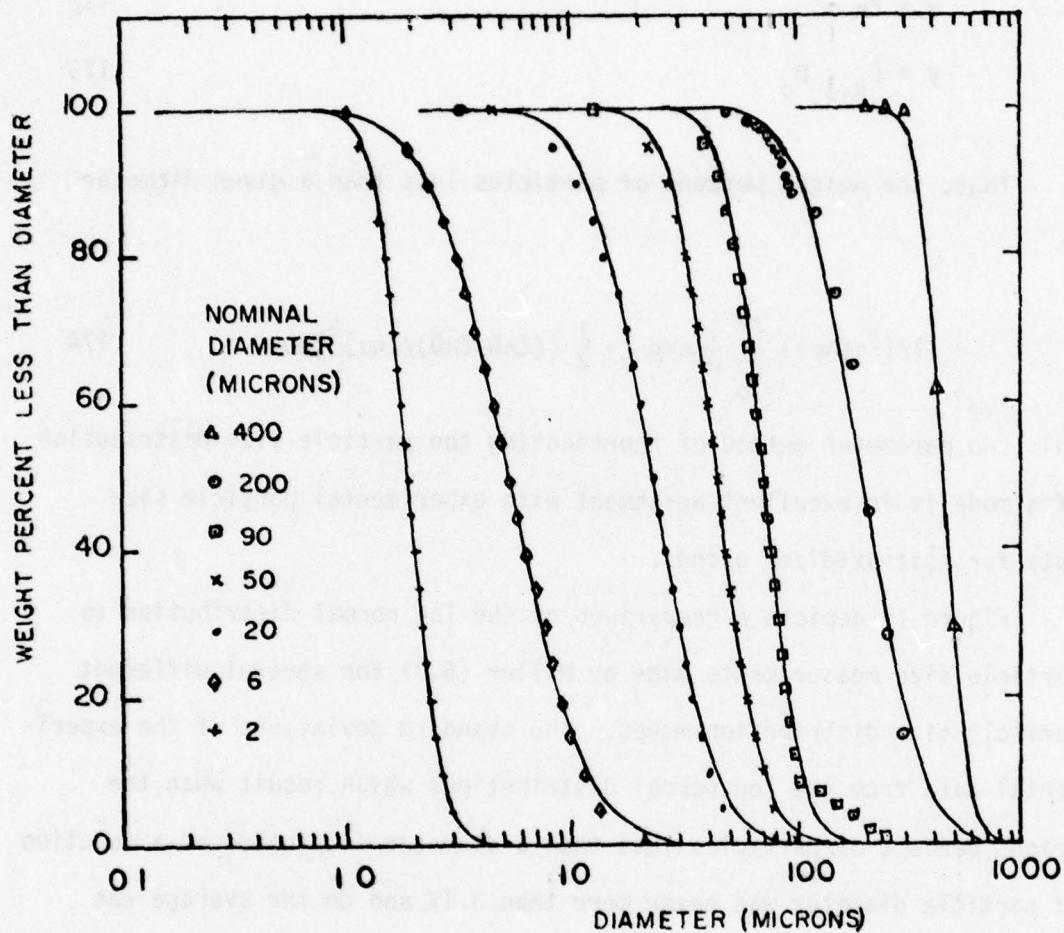


Figure 19. Weight Percent Less than Diameter Versus Diameter, Comparison of Log Normal Distributions to Measured Data of Several AP Grinds

### Derivation of the Physiochemical Model

The BDP multiple flame model was used as a foundation upon which to build a more realistic physiochemical model. A complete description of the BDP model can be found in the literature review. The major similarity between the BDP and PEM models is the assumed flame structure. However, the assumed surface geometry and statistical approach differ extensively. The diffusion flame standoff distance and the AP flame rate constant calculations also differ from the BDP approach. A complete derivation of the physiochemical model will follow.

The Mean Deflagrating State. A critical problem in statistical combustion modeling is to define an oxidizer particle's mean deflagrating state. The method employed is to calculate the burning rate of the oxidizer particle as a function of time during the entire lifetime of the particle from its birth at the propellant burning surface until the particle is fully consumed. The regression rate is calculated at specific increments during the regression of the particle in order that a rate versus time curve can be generated. The mean mass flux can then be determined by the numerical integration of the curve.

$$\bar{m} = \frac{1}{\tau} \int_0^{\tau} m dt \quad 175$$

where  $\tau$  is the lifetime of the particle at the burning surface. This process is illustrated in Figure 20. The calculation of the pseudopropellant mass flux at the indicated increments is based on the assumption that the mixture ratio of oxidizer to fuel remains constant during the combustion of the oxidizer particle. A complete description of the



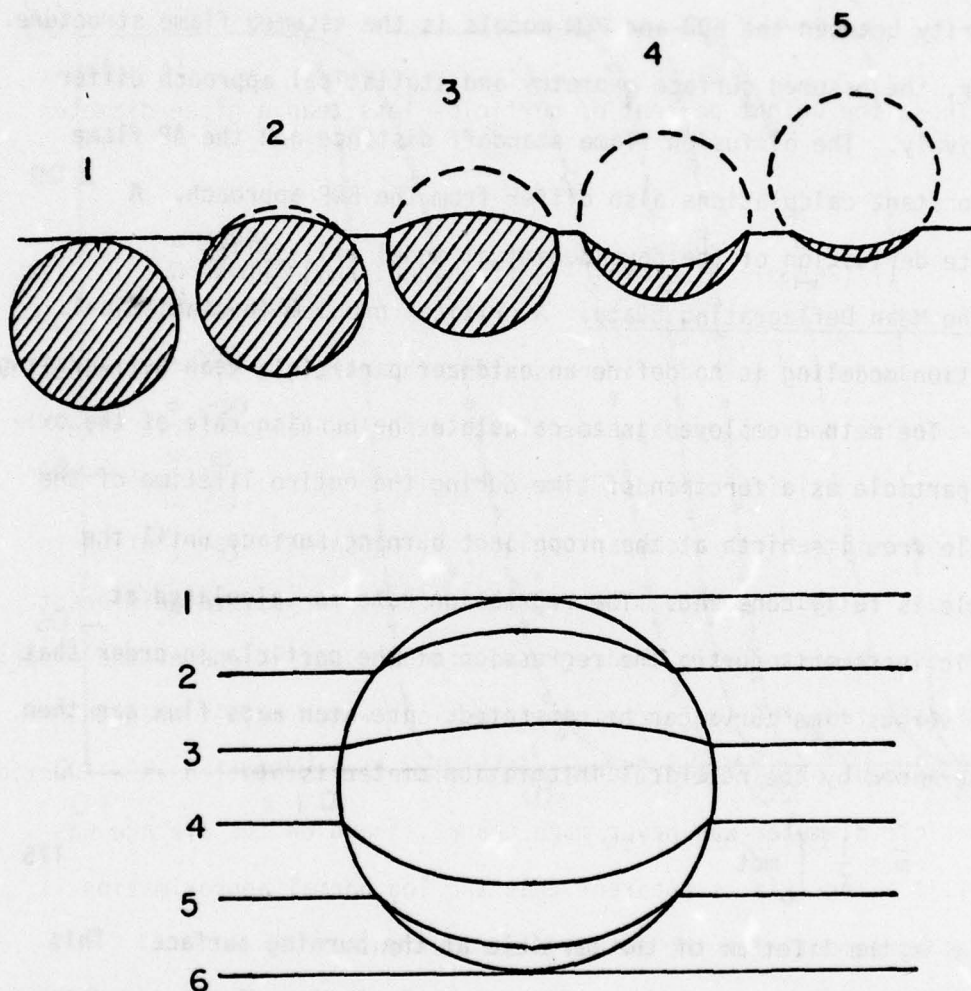


Figure 20. The Birth and Consumption of an Oxidizer Particle

equations used to calculate the mass flux as well as the solution methodology will follow.

The Flame Structure. The flame structure is depicted in Figure 8. A complete description of the structure was given in the BDP section of the literature review and will not be discussed here.

The Conservation of Mass. For a burning propellant, the equation of continuity may be written

$$\dot{m}_T = r\rho_p = \dot{m}_f(S_f/S_T) + \dot{m}_{ox}(S_{ox}/S_T) \quad 176$$

where  $\dot{m}$  represents the mass flux,  $S$  the surface area, and the subscripts  $f$ ,  $ox$  and  $T$  stand for fuel, oxidizer and total surface area respectively. This equation can be simplified further since it is assumed that the ratio of oxidizer consumption to fuel consumption remains constant during the consumption of the oxidizer particle.

$$\frac{\dot{m}_{ox}(S_{ox}/S_T)}{\dot{m}_f(S_f/S_T)} = \frac{\alpha^*}{1-\alpha^*} \quad 177$$

where  $\alpha^*$  is the mass fraction of oxidizer in the pseudopropellant. Thus

$$\dot{m}_T = (S_{ox}/S_T)\dot{m}_{ox}/\alpha^* \quad 178$$

or

$$\dot{m}_T = (S_f/S_T)\dot{m}_f/(1-\alpha^*) \quad 179$$

Thus, the burning rate can be calculated from either equation 178 or equation 179. Since it is assumed that the oxidizer regression controls the overall burning rate, equation 178 is chosen as the continuity equation.

The Pseudopropellant Surface Geometry. To evaluate the area ratio in equation 178, the geometric relationship between the oxidizer and the binder must be established. The oxidizer surface area at any point during its consumption is calculated by assuming that the regressing oxidizer surface is spherical in shape as depicted in Figure 21, where  $R$  is the radius of curvature of the surface. It is assumed that the fuel binder regresses continually, but the oxidizer is assumed to undergo an ignition delay upon reaching the burning propellant surface. The ignition delay time is assumed to have the form derived by Shannon (25). Thus

$$t_{\text{ign}} = C_{\text{ign}} D_o^{U+1} / P^W \quad 180$$

where  $C_{\text{ign}}$ ,  $U$  and  $W$  are constants.  $D_o$  is the oxidizer particle diameter and  $P$  is the pressure. Therefore, the distance  $d_{\text{ox}}$  in Figure 21 is

$$d_{\text{ox}} = 1/\rho_{\text{ox}} \int_0^{t_b - t_{\text{ign}}} \dot{m}_{\text{ox}} dt \quad 181$$

the distance  $d_f$  is

$$d_f = 1/\rho_f \int_0^{t_b} \dot{m}_f dt \quad 182$$



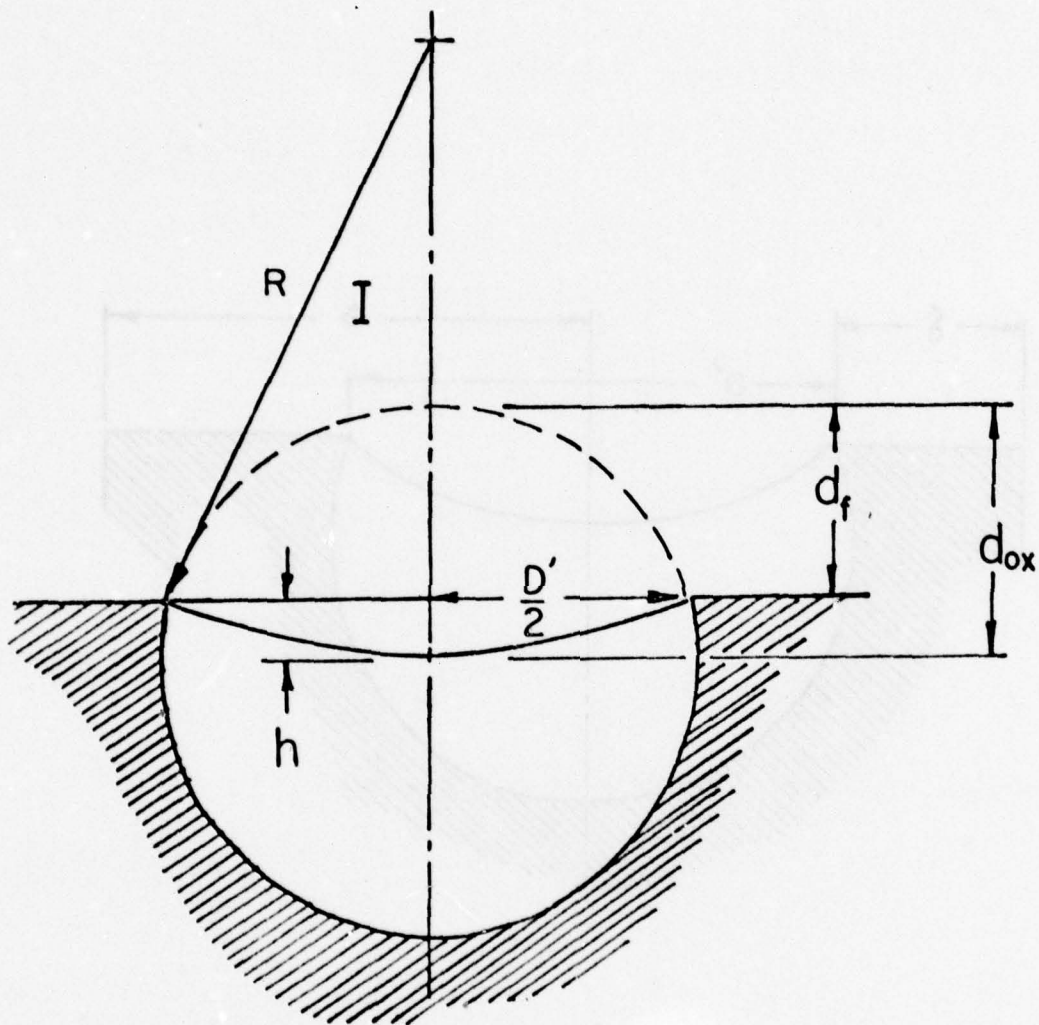


Figure 21. The Pseudopropellant Burning Geometry

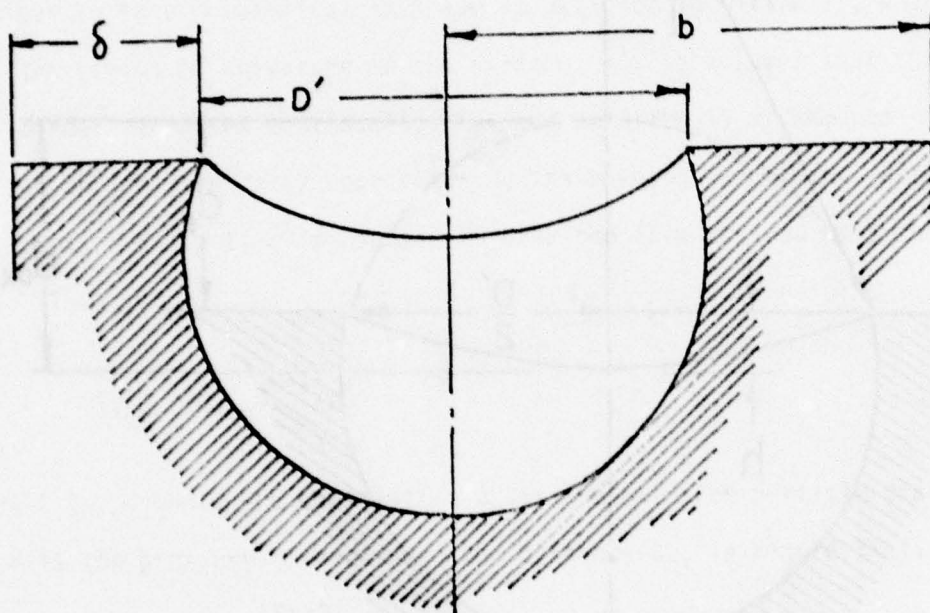


Figure 22. The Pseudopropellant Surface Geometry

and  $h$  in Figure 21 is

$$h = d_{ox} - d_f \quad 183$$

The radius of curvature,  $R$ , can be determined by triangle I in Figure 21. Thus

$$R^2 = (R - h)^2 + (D'/2)^2 \quad 184$$

where  $D'$  is the intersection diameter of the oxidizer particle with the fuel plane at any instant. Therefore,

$$R = h/2 + (D'/2)^2/2h \quad 185$$

The surface area of the spherical segment representing the burning AP surface is

$$S_{ox} = 2\pi R|h| \quad 186$$

Combining equations 185 and 186 yields

$$S_{ox} = \pi[h^2 + (D'/2)^2] \quad 187$$

The intersection diameter,  $D'$ , can be determined from geometric considerations

$$D' = 2[d_f D_o - d_f^2]^{1/2} \quad 188$$



The total burning surface area for the pseudopropellant is given by the sum of the planar fuel area with the oxidizer surface area. Since the mixture ratio of oxidizer to fuel is assumed to be constant throughout the combustion of the oxidizer particle, the planar surface area of the fuel binder associated with the pseudopropellant can easily be determined. From Figure 22, it is clear that

$$\frac{S_{ox}^p}{S_f^p + S_{ox}^p} = \zeta^* \quad 189$$

where  $\zeta^*$  is the volume fraction of oxidizer in the pseudopropellant and  $S_{ox}^p$  is the projection of the oxidizer surface on the fuel plane. The planar oxidizer area is

$$S_{ox}^p = \pi(D'/2)^2 \quad 190$$

and

$$S_{ox}^p + S_f^p = \pi b^2 \quad 191$$

Combining equations 189, 190, and 191 yields

$$b = D'/(2\sqrt{\zeta^*}) \quad 192$$

The planar fuel surface area can now be determined. Thus

$$S_f^p = \pi(D'/2)^2 [1/\zeta^* - 1] \quad 193$$

and the total surface area is

$$S_T^p = S_f^p + S_{ox}^p = \pi([h^2 + (D'/2)^2] + (D'/2)^2[1/\zeta^* - 1]) \quad 194$$

The ratio of oxidizer surface area to total pseudopropellant surface area is

$$(S_{ox}/S_T) = [h^2 + (D'/2)^2]/([h^2 + (D'/2)^2] + (D'/2)^2[1/\zeta^* - 1]) \quad 195$$

Surface Pyrolysis. The mass flux of the oxidizer,  $\dot{m}_{ox}$  is calculated by assuming that global kinetics adequately describes the decomposition of the oxidizer and the fuel. Thus, utilizing an Arrhenius expression, the mass flux of oxidizer can be expressed

$$\dot{m}_{ox} = A_{ox} \exp(-E_{ox}/RT_s) \quad 32$$

Similarly for the fuel pyrolysis the mass flux can be expressed

$$\dot{m}_f = A_f \exp(-E_f/RT_s) \quad 31$$

where  $A$  is the pre-exponential constant,  $E$  is the effective activation energy,  $R$  is the gas constant and  $T_s$  is the surface temperature. It should be noted that equation 31 is used only in the determination of the surface geometry and is not used directly for the burning rate calculation. The surface temperature used in equations 31 and 32 is assumed to be the average surface temperature for the entire pseudopropellant surface.

The Conservation of Energy at the Surface. It is apparent from equation 32 that the surface temperature plays an important role in determining the pseudopropellant mass flux. The surface temperature is determined by an energy balance at the burning surface. The energy balance is depicted in Figure 23. The energy required to raise the propellant from the initial propellant temperature,  $T_0$ , to the surface temperature,  $T_s$ , plus the energy required to vaporize the oxidizer, plus the energy required to vaporize the fuel binder is equal to the energy arriving at the surface from the gas phase flame zone. Assuming constant specific heat, the energy balance at the surface can be written

$$\dot{m}_T C_p (T_s - T_0) + \alpha \dot{m}_T Q_L + (1 - \alpha) \dot{m}_T Q_f = \text{ENERGY ARRIVING FROM FLAME ZONE} \quad 196$$

where  $Q_f$  is the heat of pyrolysis of the fuel binder and  $Q_L$  is the heat of gasification of the oxidizer. The heat of gasification of the oxidizer includes the endothermic decomposition step plus an exothermic decomposition step plus the exothermic reactions which occur on the decomposing surface.

In order to evaluate the amount of energy received by the surface from the flame zone, it is assumed that the two dimensional flame shape can be represented by quasi one dimensional flames for the purpose of a heat transfer analysis. This is illustrated in Figure 24.

If it is assumed that the gas phase energy release is concentrated only at the flame location, the 1-D energy equation for the region between the final flame and the AP flame becomes



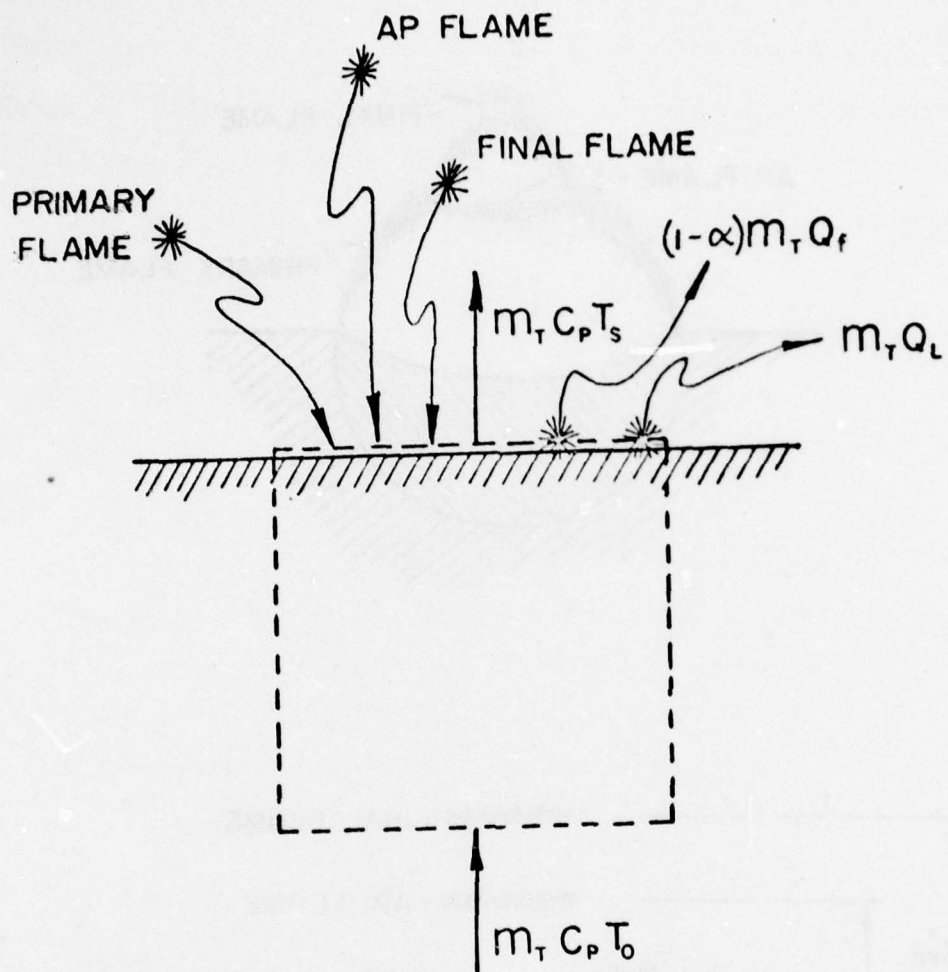


Figure 23. The Pseudopropellant Surface Energy Balance

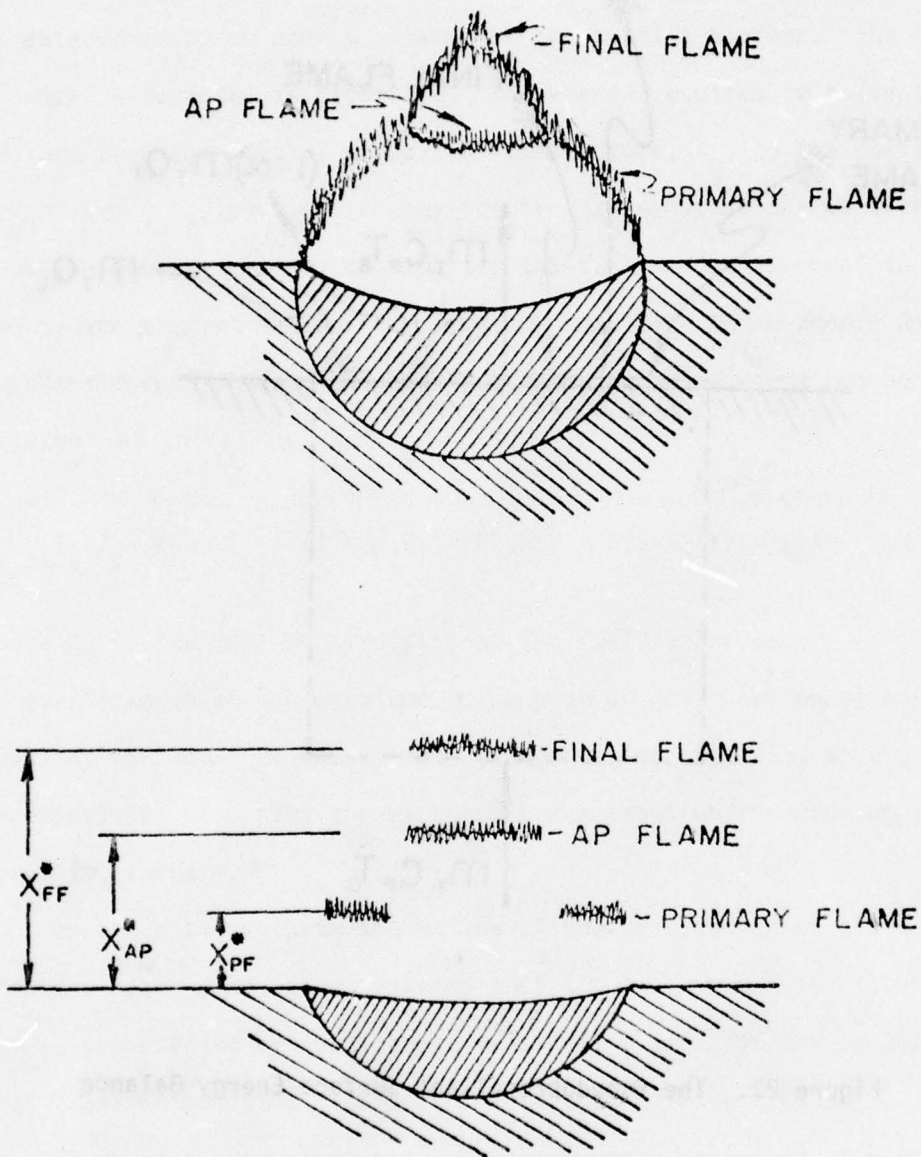


Figure 24. The PEM One Dimensional Flame Structure

$$\frac{\partial^2 T}{\partial X^2} - \frac{\dot{m}C_p}{k} \frac{\partial T}{\partial X} = 0 \quad 197$$

The boundary conditions are

$$@ X = X_{AP} \quad T = T(X_{AP}) \quad 198$$

$$@ X = X_{FF} \quad T = T_{FF} \quad 199$$

where  $X_{AP}$  and  $X_{FF}$  are defined in Figure 24,  $T_{FF}$  is the adiabatic final flame temperature and  $T(X_{AP})$  is the temperature at the location of the AP flame. With the above boundary conditions, the solution to equation 197 becomes

$$\begin{aligned} T = T_{FF} + (T_{FF} - T(X_{AP})) & \left[ \frac{\exp(\dot{m}_{ox} C_p X / k) - \exp(\dot{m}_{ox} C_p X_{FF} / k)}{\exp(\dot{m}_{ox} C_p X_{FF} / k) - \exp(\dot{m}_{ox} C_p X_{AP} / k)} \right] \end{aligned} \quad 200$$

An energy balance at the final flame yields

$$\dot{m}_{ox} Q_{FF} = k \left. \frac{\partial T}{\partial X} \right|_{X = X_{FF}} \quad 201$$

where  $Q_{FF}$  is the heat release in the final flame per unit of mass flux of oxidizer.

Evaluating the derivative of equation 200 with respect to  $X$  and letting

$$\xi = \dot{m} C_p X / k \quad 202$$



yields

$$\dot{m}_{ox} Q_{FF} = \dot{m}_{ox} C_p (T_{FF} - T(x_{AP})) \exp(\xi_{FF}) / (\exp(\xi_{FF}) - \exp(\xi_{AP})) \quad 203$$

Equation 203 can be rearranged to yield an expression for the AP flame temperature.

$$T(x_{AP}) = T_{FF} - Q_{FF} (1 - \exp(\xi_{AP} - \xi_{FF})) / C_p \quad 204$$

The energy equation (197) can also be solved for the region between the AP flame and the burning surface with the following boundary conditions

$$@ x = x_{AP} \quad T = T(x_{AP}) \quad 205$$

$$@ x = 0^+ \quad T = T_s \quad 206$$

The solution is

$$T = T_s + (T(x_{AP}) - T_s) (\exp(\xi) - 1) / (\exp(\xi_{AP}) - 1) \quad 207$$

The energy received by the surface from the final flame and the AP flame may now be determined

$$\dot{m}_{ox} Q_{surf}^{AP,FF} = k \left. \frac{\partial T}{\partial x} \right|_{x=0^+} \quad 208$$

Evaluating the derivative of equation 207 and combining the result with equation 208 yields

$$Q_{\text{surf}}^{\text{AP,FF}} = (T(x_{\text{AP}}) - T_s) / (\exp(\xi_{\text{AP}}) - 1) \quad 209$$

The surface temperature in equation 209 can be eliminated by performing an energy balance at the AP flame

$$k \left. \frac{\partial T}{\partial x} \right|_{x=x_{\text{AP}}^+} + \dot{m}_{\text{ox}} Q_{\text{AP}} = k \left. \frac{\partial T}{\partial x} \right|_{x=x_{\text{AP}}} \quad 210$$

where  $Q_{\text{AP}}$  is the heat released in the AP flame per unit of mass flux of oxidizer. The derivative on the left hand side is evaluated with equation 200 while the derivative on the right hand side is evaluated with equation 207. Equation 210 becomes

$$T(x_{\text{AP}}) - T_s = Q_{\text{AP}}(\exp(\xi_{\text{AP}}) - 1) / \exp(\xi_{\text{AP}}) + Q_{\text{FF}}(\exp(\xi_{\text{AP}}) - 1) / \exp(\xi_{\text{FF}}) \quad 211$$

Combining equation 211 with equation 209 the heat flux to the surface from the final flame and the AP flame becomes

$$\dot{m}_{\text{ox}} Q_{\text{surf}}^{\text{AP,FF}} = \dot{m}_{\text{ox}} Q_{\text{AP}} \exp(-\xi_{\text{AP}}) + \dot{m}_{\text{ox}} Q_{\text{FF}} \exp(-\xi_{\text{FF}}) \quad 212$$

In a similar fashion, the heat flux to the surface from the primary flame is

$$\dot{m}_{\text{T}} Q_{\text{surf}}^{\text{PF}} = \dot{m}_{\text{T}} Q_{\text{PF}} \exp(-\xi_{\text{FF}}) \quad 213$$

The surface energy balance can now be written

$$\begin{aligned} \dot{m}_T C_p (T_f - T_o) = & -\alpha \dot{m}_T Q_L - (1-\alpha) \dot{m}_T Q_f + \beta_f Q_{PF} \dot{m}_T \exp(-\epsilon_{PF}) \\ & + (1-\beta_f) \dot{m}_T \alpha [Q_{AP} \exp(-\epsilon_{AP}) Q_{FF} \exp(-\epsilon_{FF})] \end{aligned} \quad 214$$

where the parameter,  $\beta_f$ , appearing in equation 214 represents the fraction of the reactants that react in the primary flame. Equation 214 can be rearranged so that the average pseudopropellant surface temperature becomes

$$\begin{aligned} T_s = T_o - \alpha Q_L / C_p - (1-\alpha) Q_f / C_p + (1-\beta_f) \alpha / C_p [Q_{AP} \exp(-\epsilon_{AP}) \\ + Q_{FF} \exp(-\epsilon_{FF})] + \beta_f Q_{PF} \exp(-\epsilon_{PF}) / C_p \end{aligned} \quad 215$$

The energy balances for the gas phase heat releases ( $Q_{AP}$ ,  $Q_{PF}$ , and  $Q_{FF}$ ) were presented in the review of the BDP model. Thus

$$Q_{AP} = C_p (T_{AP} - T_o) + Q_L \quad 216$$

$$Q_{FF} = C_p (T_f - T_o) - \alpha C_p (T_{AP} - T_o) + (1 - \alpha) Q_f \quad 217$$

and

$$Q_{PF} = C_p (T_f - T_o) + \alpha Q_L + (1 - \alpha) Q_f \quad 218$$

where  $T_{AP}$  is the adiabatic flame temperature of the AP flame. Thus, the energy equation at the surface yields a value for the average pseudopropellant surface temperature which is a necessary parameter for the burning rate calculations.

Flame Standoff Distances. The nondimensional flame standoff distances appearing in the surface energy balance are defined



$$\epsilon_{AP}^* = \dot{m}_{ox} C_p X_{AP}^*/k \quad 219$$

$$\epsilon_T^* = \dot{m}_{ox} C_p (X_{AP}^* + X_{FF}^*)/k$$

$$\epsilon_{PF}^* = \dot{m}_T C_p (X_{PD}^* + X_{PF}^*)/k \quad 221$$

where  $X_{AP}^*$  and  $X_{PF}^*$  are the kinetics distances for the AP and primary flame respectively. The diffusion distances for the primary and final flame are, respectively,  $X_{PD}^*$  and  $X_{FF}^*$ .

The kinetics distances were evaluated by integration of the reaction rate for a reaction of arbitrary order. Thus

$$X^* = \dot{m}/KP^\delta \quad 222$$

where  $K$  represents a pseudo rate constant and is evaluated by an Arrhenius expression. The primary flame rate constant may be written

$$K_{PF} = A_{PF} \exp(E_{PF}/RT_{FF}) \quad 223$$

where  $T_{FF}$  is the adiabatic flame temperature. Similarly, the AP flame rate constant is

$$K_{AP} = A_{AP} \exp(-E_{AP}/RT(X_{AP})) \quad 224$$

where  $T(X_{AP})$  is the temperature of the AP flame given by equation 205 (not necessarily the adiabatic flame temperature).

The diffusion distances are evaluated by a Burke Schumann Bunsen burner type of analysis (26). The geometry for the analysis is depicted in Figure 25 where the dimensions  $\delta$ ,  $D'$  and  $b$  were described previously in the section on surface geometry. Burke and Schumann solved the mass

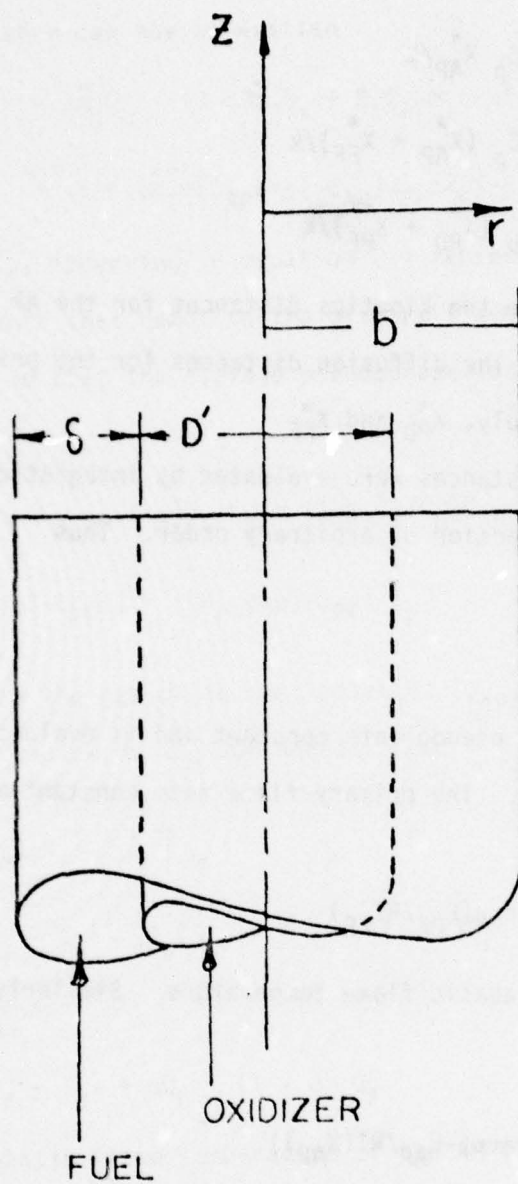


Figure 25. The Burke-Schumann Bunsen Burner Configuration

conservation equation for a Bunsen burner type of flame.

The diffusion equation can be written

$$\frac{\partial^2 \beta}{\partial z^2} + \frac{1}{r} \frac{\partial}{\partial r} \left( r \frac{\partial \beta}{\partial r} \right) = \frac{u}{D} \frac{\partial \beta}{\partial z} \quad 225$$

where  $\beta$  is a concentration term. In the original solution to equation 225 by Burke and Schumann the second derivative of  $\beta$  with respect to  $z$  was assumed negligible. This assumption is valid for tall flames where the peak flame height is large compared to the burner dimensions. The Burke-Schumann solution of equation 225 is

$$\frac{v - (1+v)c^2}{2(1+v)c^2} = \sum_{i=1}^{\infty} \frac{J_1(c\phi_i)}{\phi_i} \frac{J_0(\phi_i \xi)}{[J_0(\phi_i)]^2} \exp(-\phi_i^2 \eta) \quad 226$$

where  $J$  represents a Bessel function,  $v$  is a stoichiometric ratio,  $c$  is related to the burner geometry,  $\phi_i$  represents roots of the first order Bessel function,  $\xi$  is the non-dimensional radial distance,  $\eta$  is the nondimensional axial distance and the burner geometry parameter,  $c$ , may be defined

$$c = D'/2b \quad 227$$

The solution to equation 226 was modified by Beckstead et al. (18) to include the second derivative of  $\beta$  with respect to the axial direction, thus yielding a solution that is valid for short flames.

$$\frac{v - (1+v)c^2}{2(1+v)c^2} = \sum_{i=1}^{\infty} \frac{1}{\phi_i} \frac{J_1(c\phi_i)}{[J_0(\phi_i)]^2} J_0(\phi_i \xi) \exp \left[ - \frac{([1 + (2\psi\phi_i)^2]^{1/2} - 1)\eta}{2\psi^2} \right] \quad 228$$



which is identical to equation 226 with the exception of the term in the exponent, and where

$$\psi = \frac{D}{Ub}$$

229

Equation 228 could be used to calculate the actual flame shape, however it is not necessary since the heat transfer to the burning surface from the flame is assumed to be one dimensional. Also, a calculation of the actual flame shape would be prohibitive in terms of computational time. Thus, a parabolic flame shape is assumed and equation 228 is used only to calculate the peak height of the diffusion flame. The value of the peak height calculated by equation 228 is then multiplied by a constant factor so that the result is the approximate height of a one dimensional flame above the surface in order to transfer the same amount of heat to the surface as the parabolic flame.

The equation for the flame height at the center of the flame becomes

$$\frac{v - (1+v)c^2}{2(1+v)c} = \sum_{i=1}^{\infty} \frac{1}{\phi_i} \frac{J_1(c\phi_i)}{[J_0(\phi_i)]^2} \exp \left[ - \frac{([1 + (2\psi\phi_i)^2]^{1/2} - 1)\eta}{2\psi^2} \right] \quad 230$$

If, however, the flame is underventilated, the equation for the flame height becomes

$$\frac{v - (1-v)c^2}{2(1+v)c} = \sum_{i=1}^{\infty} \frac{1}{\phi_i} \frac{J_1(c\phi_i)}{J_0(\phi_i)} \exp \left[ - \frac{([1 + (2\psi\phi_i)^2]^{1/2} - 1)\eta}{2\psi^2} \right] \quad 231$$

The diffusion mixing distance then becomes

$$x_D^* = b\eta/\psi \quad 232$$

Determination of the Fraction of Reactants that React in the Primary Flame. The only remaining unknown in the surface energy balance is  $\beta_f$ , the fraction of reactants that react in the primary flame. The  $\beta_f$  parameter is determined in the same manner in the present model as in the BDP model. This method was discussed in the review of the BDP model and will not be repeated here.

Summary of the Basic Equations. The equations of the physiochemical model have now been derived and the main equations are summarized below.

Total Mass Flux from Surface of Pseudopropellant

$$\dot{m}_T = (S_{ox}/S_T) \dot{m}_{ox}/\alpha^* \quad 178$$

Surface Geometry

$$(S_{ox}/S_T) = [h^2 + (D'/2)^2]/[h^2 + (D'/2)^2 + (D'/2)^2 [1/\xi^* - 1]] \quad 195$$

Oxidizer Mass Flux

$$\dot{m}_{ox} = A_{ox} \exp(-E_{ox}/RT_s) \quad 196$$

Surface Temperature

$$T_s = T_o - \alpha Q_L/C_p - (1 - \alpha)Q_f/C_p + (1 - \beta_f)\alpha/C_p [Q_{AP} \exp(-\xi_{AP}^*) + Q_{FF} \exp(-\xi_{FF}^*)] + \beta_f Q_{PF} \exp(-\xi_{PF}^*)/C_p \quad 215$$

Solution of the Basic Equations. The simultaneous set of equations which make up the model are solved numerically by a secant iteration on the surface temperature. Embedded within the iteration on the surface temperature are two inner iteration loops. One is a Newton iteration on the solution of equation 228 for the diffusion flame standoff distance. The other is an iteration on the AP flame standoff distance. Once the surface temperature has been determined, the mass flux from a pseudopropellant at a given instant in time can be determined using equation 178.

This process is repeated at time increments over the lifetime of a particle in a particular pseudopropellant. The mean state or average mass flux for the pseudopropellant can then be evaluated by equation 175

$$\bar{m}'' = \frac{1}{\tau} \int_0^{\tau} \dot{m}_T dt \quad 175$$

This entire process is then repeated at increments in oxidizer particle diameter such that the total oxidizer particle size distribution is represented by a series of pseudopropellants.

Having obtained the mean states for each of the pseudopropellants, as well as the physical properties of the pseudopropellants, the overall composite propellant burning rate is determined by equation 168.

$$\bar{r} = \sum_{k=1}^{\delta} \rho_{o,k}^{-1} \int_{D_o} (\bar{m}_{pdk} / \tau_{dk}^*) F_k dD_o \quad 168$$



### Modification of the Model to Include Burning Rate Catalysts

The equations of the PEM were modified so that the effect of burning rate catalysts could be evaluated.

There are two flame zones in the PEM model in which the catalyst can manifest itself. One of those is the primary flame which is the reaction of the oxidizer decomposition products with the fuel binder products. The other is the AP monopropellant flame which is the reaction between the AP decomposition products to form oxygen and inert products. An Arrhenius expression was assumed for both the primary flame and the AP flame rate constants. Thus

$$K_{PF} = A_{PF} \exp (E_{PF}/RT_{FF}) \quad 233$$

$$K_{AP} = A_{AP} \exp (E_{AP}/RT_{AP}) \quad 234$$

where A is the Arrhenius frequency factor, E is the activation energy, R is the gas constant and T is the flame temperature.

The action of a catalyst on solid propellant combustion was assumed to be through the decrease of the activation energies of either or both of the AP and primary flames.

The catalyst is assumed not to affect the final flame kinetics (the reaction between the binder decomposition products and the products of the AP monopropellant flame). The reason being that the reactants for the final flame are preheated to at least the AP flame temperature, thus, the kinetics are instantaneous compared to the mixing time.

A primary problem in including the effects of catalysts in a propellant combustion model is a lack of knowledge of where a particular catalyst acts.

Since the primary flame is more predominant at low pressures and for small oxidizer particles, one would expect that a catalyst which acts on the primary flame kinetics would have a more pronounced effect on the burning rate at low pressure than at high pressure. Moreover, a shift in particle size distribution to finer oxidizer in a catalyzed propellant would be expected to produce a more pronounced effect on the burning rate than the same shift in particle size in a comparable uncatalyzed propellant. The AP flame, on the other hand, is more predominant at high pressure and for large oxidizer particles. Thus, one would expect that a catalyst which acts on the AP flame kinetics would have a more pronounced effect on the burning rate at high pressure than at low pressure. Moreover, a shift in particle size distribution to coarser oxidizer in a catalyzed propellant would be expected to produce a more pronounced effect on burning rate than the same shift in particle size distribution in a comparable uncatalyzed propellant.

Thus, a small amount of experimental data could be employed to determine the action site of various burning rate catalysts.

Experimental evidence (53) suggests that there are two parameters of importance, other than the type of catalyst employed, in determining the effect of catalysts on propellant burning rate. They are the mass fraction of catalyst present in the propellant and the specific surface area of the catalyst. Furthermore, continued increases in either of the above two parameters in a specific propellant produces diminishing returns in terms of an increase in burning rate. A point is finally reached where further increases in the mass fraction of catalyst produce reduced burning rates.

The actual effect of burning rate catalyst on the chemical reaction kinetics is not completely understood and, at the present time, is beyond the scope of this modeling effort. However, once the site of the catalyst action is determined, the effect of catalyst on the reaction kinetics can be handled in a semi-empirical fashion.

The catalysts are accounted for in the present combustion model by modifying the rate constants through polynomial expressions for the activation energies. The constants in the polynomial expressions are determined by a regression analysis in which the parameters of importance are the mass fraction and the specific surface area of the catalyst.

Since catalysts comprise a distribution of particles, the addition of catalyst particles to a propellant shifts the particle size distribution of the oxidizer particles such that there is a redistribution of the fuel binder associated with each particle. This particular aspect has not been accounted for in the present model. However, since the amount of catalyst usually present in a propellant is quite small (on the order of 1% or less by weight) this effect is expected to be negligible.

The only other modification to the steady state model to account for catalysts is in the energy balance at the burning surface.

#### The Erosive Burning Model

The erosive burning model is based on the hypothesis that the erosive burning effect is due to enhancement of the transport properties in the region of the gas phase reaction zone as suggested by Lengellé (43). The enhancement of the transport properties is assumed to be due to the presence of a turbulent boundary layer.



The turbulent boundary layer is modeled by an approximate solution of the Navier-Stokes and continuity equations in the region near the burning surface for flow over a flat plate with injection. In the analysis it is assumed that a turbulent boundary layer develops above the propellant surface and that the transport coefficients of diffusion and heat conduction are modified in such a way that the heat flux to the surface and, consequently, the propellant burning rate are enhanced.

The model for the turbulent boundary layer is coupled with the PEM to form the erosive burning model. The basic assumptions and the development of the PEM have been discussed in a prior section. A discussion of the turbulent boundary layer model and the development of the equations which relate transport properties to the cross flow velocity will follow.

The Turbulent Boundary Layer. The turbulent boundary layer model is based on an approximate analysis of the flow over a flat plate with injection. The basic equations used in this analysis are the Navier-Stokes equations representing conservation of momentum and continuity. These equations are applied to turbulent flow by representing the dependent quantities in the equations as the sum of a time averaged quantity plus an instantaneous quantity. When the resulting equations are time averaged and the usual boundary layer assumptions are imposed the resulting boundary layer equations are (54):

$$\frac{\partial}{\partial x} (\bar{\rho} \bar{u}) + \frac{\partial}{\partial y} (\bar{\rho} \bar{v} + \overline{\rho' v'}) = 0 \quad 235$$

$$\bar{\rho} \bar{u} \frac{\partial \bar{u}}{\partial x} + (\bar{\rho} \bar{v} + \overline{\rho' v'}) \frac{\partial \bar{u}}{\partial y} = \frac{\partial}{\partial y} (\bar{\mu} \frac{\partial \bar{u}}{\partial y} - \overline{\rho' u' v'}) \quad 236$$

where the barred quantities represent time averages and the primed quantities represent instantaneous values of the fluctuating quantities. The coordinate system and a physical description of the model are depicted in Figure 26.

For the present analysis it is assumed that the fluid properties of viscosity and density remain constant throughout the flow field. In order to achieve an engineering solution to the problem it is also assumed that the variations of the dependent variables with respect to  $x$  are negligible compared to their variations with respect to  $y$ . The latter assumption allows the partial differential equations for conservation of momentum and mass to be replaced by ordinary differential equations. It has been found (54) that this assumption combined with assumptions concerning the mechanism of turbulence can lead to solutions for the skin friction coefficients which agree well with experimental results. Moreover, the present analysis is concerned primarily with the inner region of the boundary layer where gradients in the  $y$  direction are much larger than gradients in the  $x$  direction. Thus, the assumptions should be valid even in the case of an imposed velocity and pressure gradient parallel to the surface, as is the case within a rocket motor chamber.

With the above assumptions equations 235 and 236 can be simplified to

$$\frac{d(\rho \bar{v})}{dy} = 0 \quad 237$$

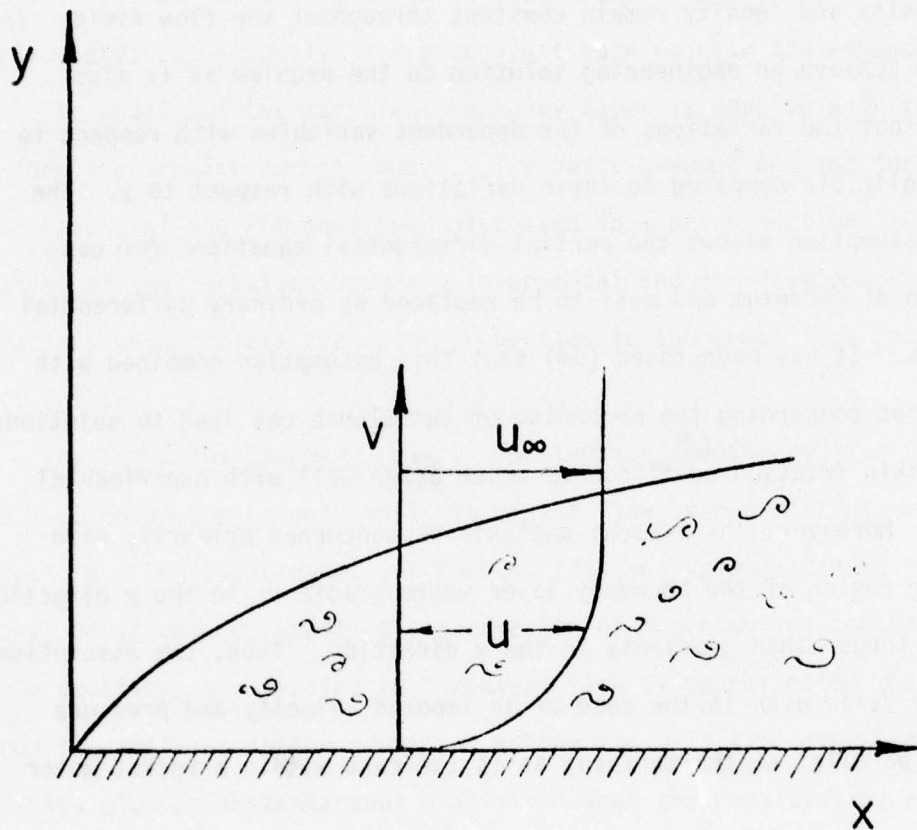


Figure 26. The Physical Model for the Turbulent Boundary Layer



$$\rho \bar{v} \frac{d\bar{u}}{dy} = \mu \frac{d^2 \bar{u}}{dy^2} - \rho \frac{d\overline{u'v'}}{dy} \quad 238$$

Integration of equation 238 yields

$$\rho \bar{v} = \text{constant} = (\rho v)_w \quad 239$$

where  $(\rho v)_w$  is the mass flux from the burning propellant surface. Thus, equation 238 becomes

$$(\rho v)_w \frac{d\bar{u}}{dy} = \mu \frac{d^2 \bar{u}}{dy^2} - \rho \frac{d\overline{u'v'}}{dy} \quad 240$$

The fluctuating terms in equation 240 can be dealt with by employing the Boussinesq relation for the eddy viscosity.

$$-\rho \overline{u'v'} = \rho \epsilon \frac{\partial \bar{u}}{\partial y} \quad 241$$

where  $\epsilon$  is the eddy diffusivity of momentum.

Combining equations 240 and 241 yields

$$(\rho v)_w \frac{d\bar{u}}{dy} = (\mu + \rho \epsilon) \frac{d^2 \bar{u}}{dy^2} \quad 242$$

Note that the bars representing time-averaged quantities have been dropped as all of the terms are mean values and the fluctuating terms no longer appear.

If it is assumed that the Prandtl mixing length hypothesis is valid for the case of blowing, the eddy momentum diffusivity can be written

$$\epsilon = c' y^2 \frac{du}{dy} \quad 243$$

Substituting equation 243 into equation 242 results in a non-linear second order differential equation. It was anticipated that a solution of this non-linear boundary value problem would be too prohibitive in terms of computer time to be of value in the erosive burning rate iteration. Thus, an approximate solution of equations 242 and 243 was deemed appropriate for the present analysis

The governing equation can be approximated (43,66)

$$(\rho v)_w u \approx (\mu + \rho \epsilon) \frac{du}{dy} - \tau_w \quad 244$$

for the case of constant properties where the no slip condition at the wall

$$@ y = 0 \quad u = 0 \quad 245$$

has been used and  $\tau_w$  is the shear stress at the wall.

Substituting equation 243 into equation 244 results in the following non-linear first order ordinary differential equation relating the parallel and normal components of velocity:

$$\rho c' y^2 \left( \frac{du}{dy} \right)^2 + \mu \frac{du}{dy} - (\tau_w + (\rho v)_w u) = 0 \quad 246$$

Equation 246 can be linearized by use of the quadratic equation

$$\frac{du}{dy} = -\frac{\mu}{2\rho c'y^2} \pm \left[ \left( \frac{\mu}{2\rho c'y^2} \right)^2 + (\tau_w + (\rho v)_w u)/(\rho c'y^2) \right]^{1/2} \quad 247$$

Since adverse pressure gradients or flow reversal are never considered, negative velocity gradients are physically unrealistic. Thus, only the plus sign of the "plus or minus" in equation 247 needs to be considered. Thus

$$\frac{du}{dy} = \left[ \left( \frac{\mu}{2\rho c'y^2} \right)^2 + (\tau_w + \rho v)_w u/(\rho c'y^2) \right]^{1/2} - \frac{\mu}{2\rho c'y^2} \quad 248$$

The boundary condition for equation 248 is

$$@ y = \delta \quad u = u_\infty \quad 249$$

where  $\delta$  is the boundary layer thickness and  $U_\infty$  is the free stream velocity. Obviously, a numerical solution is still required. However, by assuming a value for  $\tau_w$ , the above system can be treated as an initial value problem with the initial condition

$$@ y = 0 \quad \frac{du}{dy} = \tau_w/\mu \quad 250$$



A numerical solution of equation 248 can be determined by employing a marching scheme. The solution must be determined at several downstream positions in the vicinity of the position of interest in order that a relation between the shear stress at the wall and the x position can be described. The resulting velocity profiles can then be used to check on the assumed value for the surface shear stress by use of the von Karman momentum integral equation. For the case of surface blowing at constant pressure, the von Karman momentum integral can be written

$$\tau_w + (\rho v)_w u_\infty = \frac{d}{dx} \int_0^\delta \rho u(u_\infty - u) dy \quad 251$$

The derivative in equation 251 can be determined numerically after performing the indicated integration at several locations about the position of interest. If the calculated value for the wall shear does not agree with the assumed value, the wall shear stress must be determined by an iteration process.

A less rigorous but acceptable alternative to the iteration process is to use an empirical relation for the wall shear.

At this point it is convenient to define the skin friction coefficient

$$\frac{1}{2} C_f = \frac{\tau_w}{\rho u_\infty^2} \quad 252$$

For the case of no blowing the skin friction coefficient is well represented by the empirical relation (55),

$$\frac{1}{2} C_{f_0} = 0.0296 Re_x^{-0.2} \quad 253$$

where  $Re_x$  is the Reynolds number based on down stream position. The relation for skin friction given by equation 253 is valid for Reynolds numbers in the following range

$$5 \times 10^5 < Re_x < 1 \times 10^7 \quad 254$$

Another empirical relation for the skin friction coefficient is the Schultz-Grunow equation (56)

$$\frac{1}{2} C_{f_0} = 0.185 (\log_{10} Re_x)^{-2.584} \quad 255$$

which is valid to Reynolds numbers based on length to as high as  $10^9$ .

The reduction in shear stress at the wall due to blowing can be expressed by the empirical relation (43,57,58)

$$C_f/C_{f_0} = \ln(1 + B)/B \quad 256$$

where  $C_f$  is the local skin friction coefficient with blowing and  $B$  is the blowing parameter defined

$$B = (\rho v)_w / (\frac{1}{2} C_f \rho_\infty u_\infty) \quad 257$$

Figure 27 compares the prediction of equation 256 to the experimental data of Simpson and McQuaid as indicated by Mills (59).

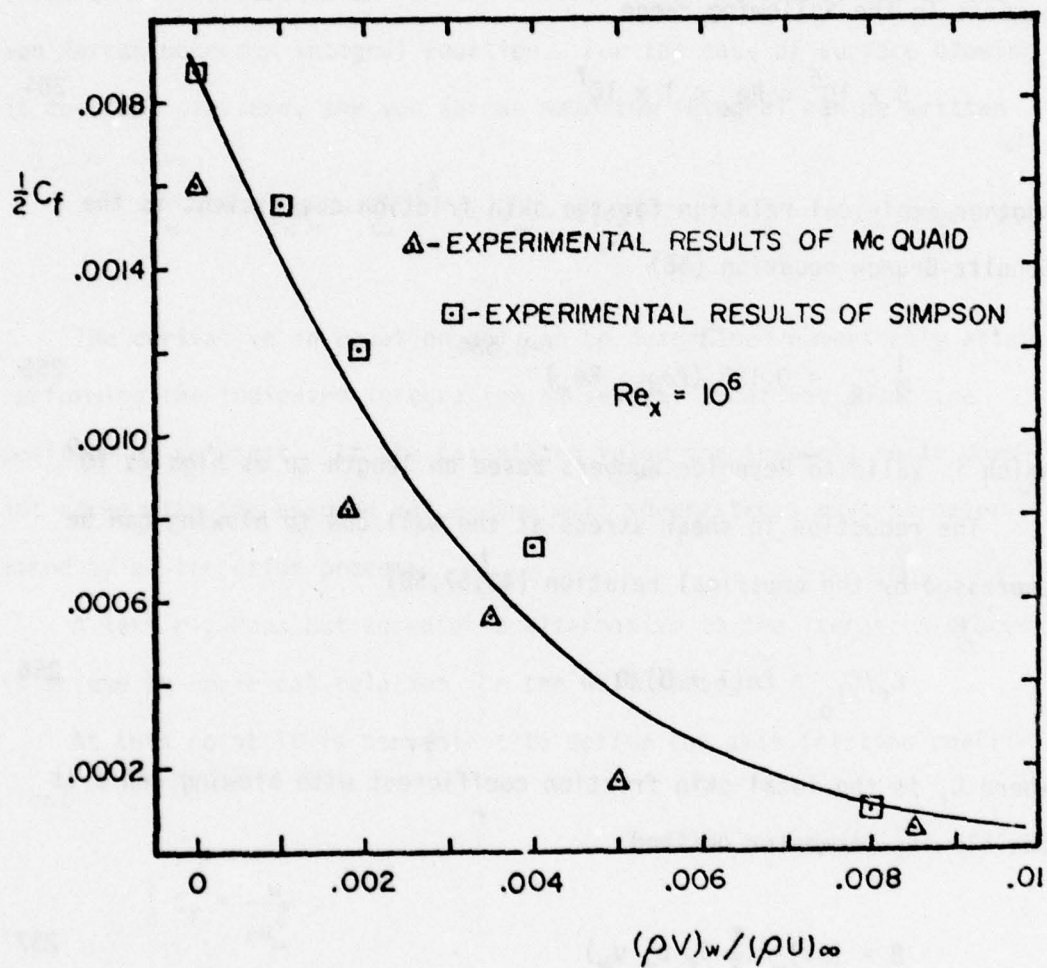


Figure 27. The Reduction in Shear Stress at the Wall Due to Injection



Combining equations 256 and 257, the blowing parameter can be written

$$B = \exp [(\rho v)_w / (\frac{1}{2} C_{f0} \rho_\infty u_\infty)] - 1 \quad 258$$

It is now possible to obtain an empirical relation for the wall shear stress  $\tau_w$ . Rearranging equation 252 and combining with equations 255, 256, and 258 yields

$$\tau_w = u_\infty (\rho v)_w / [\exp((\rho v)_w / (0.185 (\log_{10} Re_x)^{-2.584} u_\infty \rho_\infty)) - 1] \quad 259$$

An approximate solution to equation 248 can now be formulated in terms of an empirical expression for the shear stress at the burning surface. The boundary condition given by equation 245 is changed to

$$@ y = 0 \quad \frac{du}{dy} = \tau_w / \mu \quad 260$$

After evaluating the wall shear,  $\tau_w$ , with equation 259, equation 248 can be solved by a numerical marching scheme. In the present analysis a modified Euler predictor corrector (60) scheme is employed.

Figure 28 depicts several velocity profiles calculated at various blowing rates and free stream velocities. It can be seen that as the blowing rate is increased or the free stream velocity is decreased, the velocity gradient in the region near the burning surface decreases (as would be expected). It is apparent that the behavior of the predicted velocity profile is at least qualitatively correct.

Having obtained a solution for the velocity profile, the eddy momentum diffusivity in the region near the wall is computed by

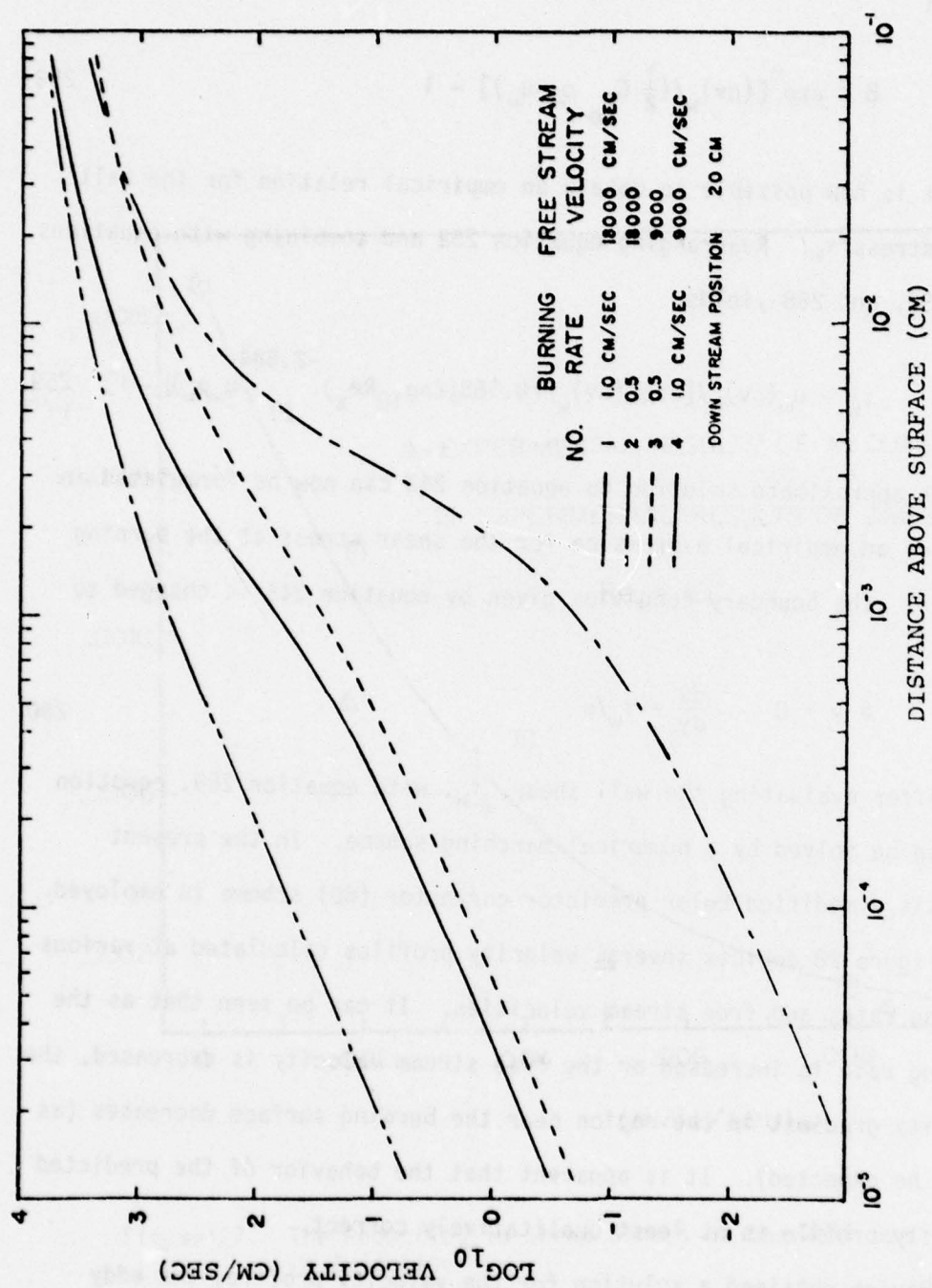


Figure 28. The Boundary Layer Velocity Profile

employing the Prandtl mixing length hypothesis

$$\epsilon = c'y^2 \frac{du}{dy} \quad 243$$

Thus the eddy diffusivity varies with ordinate in the flame zone. An average value for the eddy diffusivity in the flow region between the propellant surface and the flame of interest can be determined by the following expression:

$$(\epsilon)_{av} = 1/L \int_0^L \epsilon \, dy \quad 261$$

where  $L$  is the pseudo one dimensional flame height. Figure 29 depicts the average eddy diffusivity as a function of distance above the surface for the velocity profiles presented in Figure 28. It can be seen that the effect of blowing at the surface has a dramatic effect on the calculated values for the eddy diffusivity. Increased blowing by means of an increase in propellant burning rate or by means of a decrease in the cross flow velocity results in a drastic decrease in the average eddy diffusivity in the region near the propellant surface.

The effect of cross flow velocity on the propellant burning rate can now be determined. It is assumed that in the normal, nonerosive, combustion regime, the transport coefficients of thermal conductivity and mass diffusion are the molecular ones. However, under erosive conditions the transport coefficients are modified by turbulent components which are dependent upon the nature of the flow. Moreover, in the present analysis it is assumed that the ratio of the molecular transport property to the transport property in the presence of



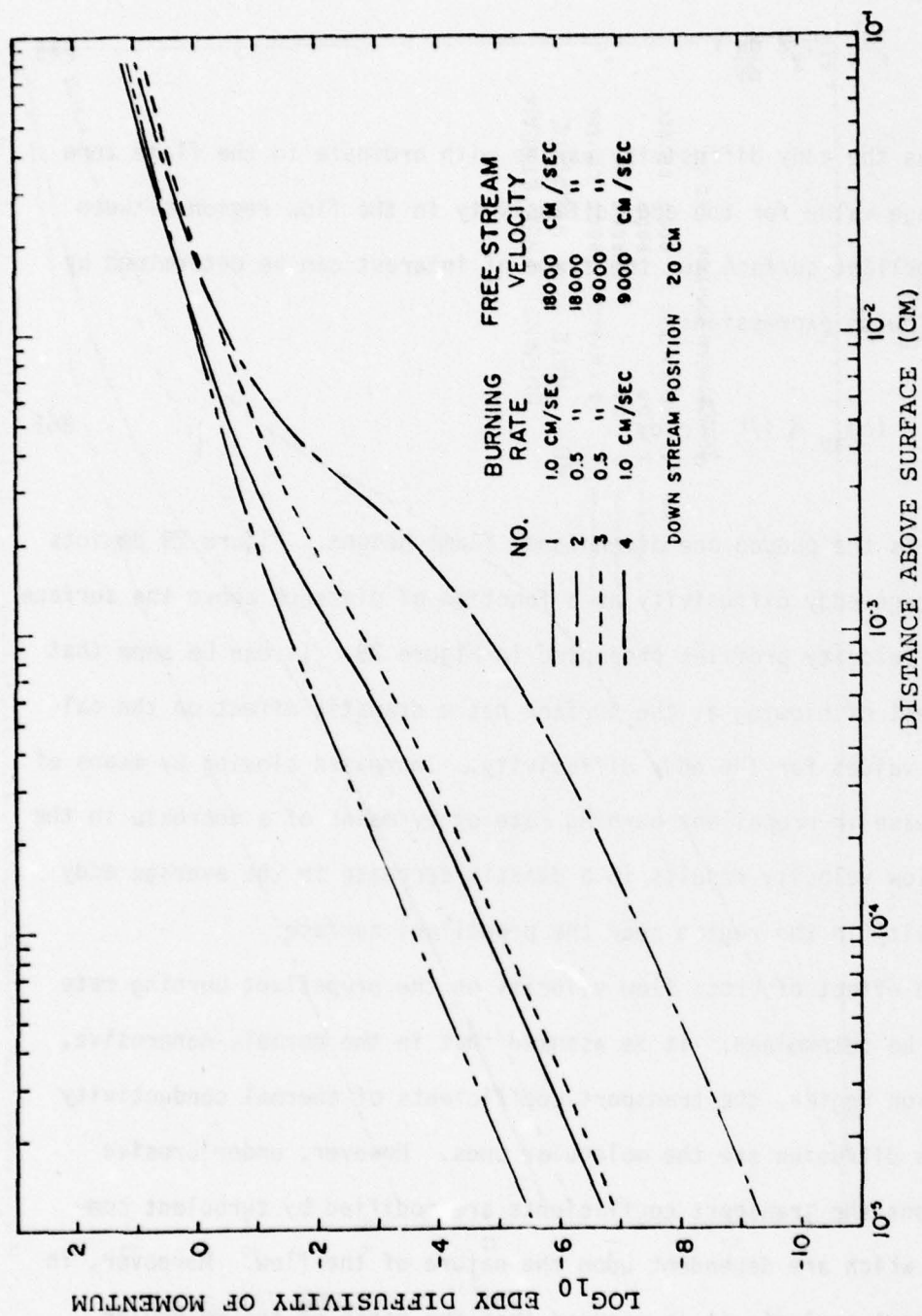


Figure 29. The Integrated Average Eddy Momentum Diffusivity Profile

turbulence is proportional to the ratio of the laminar viscosity to the average value of the total viscosity in the presence of turbulence.

Thus

$$\frac{\rho_m}{\rho_t} \propto \frac{\mu}{(\mu + \rho\epsilon)} \quad 262$$

Since there are three flames considered in the propellant combustion model, and, in general, all are of differing heights above the surface, separate average turbulent transport properties must be calculated for each flame. Thus, there are turbulent thermal conductivities associated with the AP monopropellant flame, the primary flame and the final diffusion flame,

$$\lambda_{AP}^t = k_c(1 + \rho\epsilon/\mu)\lambda \quad 263$$

$$\lambda_{PF}^t = k_c(1 + \rho\epsilon/\mu)\lambda \quad 264$$

$$\lambda_{FF}^t = k_c(1 + \rho\epsilon/\mu)\lambda \quad 265$$

and there are mass diffusion coefficients associated with the primary flame and the final diffusion flame

$$D_{PF}^t = k_D(1 + \rho\epsilon/\mu)D \quad 266$$

$$D_{FF}^t = k_D(1 + \rho\epsilon/\mu)D \quad 267$$

where  $k_c$  and  $k_D$  are the proportionality constants for equation 262,  $\epsilon$  is the average eddy diffusivity of momentum evaluated by equation 262,

and  $\lambda$  and  $D$  are the molecular thermal conductivity and mass diffusivity respectively.

Since the PEM burning rate calculation is an iterative solution of several simultaneous equations, a closed form solution for the erosive burning rate is not possible. Furthermore, the transport properties used in the burning rate calculation are a function of the propellant burning rate with a strong coupling between the propellant blowing effect, the burning rate and the transport property calculation.

An iterative solution for the erosive burning rate in which the transport properties were averaged between the values for consecutive iterations was found to be successful. The scheme employed for the solution was as follows:

1. Calculate the burning rate using the molecular transport properties.
2. With this burning rate, calculate the blowing parameter and the velocity profile in the turbulent boundary layer.
3. Using the calculated velocity profile, calculate the transport properties for the three flames.
4. Averaging the latest calculated values of the transport properties with the values computed for the prior iteration, recycle to step 1.

The process described above is repeated until the desired convergence is reached. Step 4 of the above method has proved to be extremely significant in obtaining a solution since convergence is often speeded up by a factor of ten or more (61).



The erosive burning model described above was derived for the purpose of velocity coupling calculations and was not expected to predict quantitative erosive burning results. However, as will be pointed out in the results section, the model has several unique and desirable features. For example, the model predicts a threshold velocity. Furthermore, it predicts the correct dependence of the threshold velocity on the combustion pressure and burning rate. In addition, the model is able to predict the effect of oxidizer particle size on the erosive burning characteristics.

#### The PEM Nonsteady State Combustion Model

As discussed in the introduction, the two parameters of importance in the nonsteady state combustion of composite propellants are the pressure coupled response and the velocity coupled response. Those parameters were defined and discussed in the nonsteady state combustion section of the literature review.

In order to evaluate the nonsteady state burning characteristics of a composite propellant, a nonsteady state statistical combustion model was derived from the steady state PEM.

#### Derivation of the Statistical Nonsteady State Model

The total propellant mass flux from a burning composite propellant is

$$\dot{m}_t = \rho_t \sum_{k=1}^S \rho_{o,k}^{-1} \int_{D_0} (m_{p,d,k} / \zeta_{d,k}^*) F_k dD \quad 167$$

The linear perturbation of the above equation with respect to time yields

$$\dot{m}'_t = \rho_t \sum_{k=1}^S \rho_{o,k}^{-1} \int_{D_0} (\dot{m}'_{p,d,k} / \zeta_{d,k}^*) F_k dD \quad 268$$

where the primes denote perturbed quantities.

The pressure coupled response function is

$$R_p = \frac{(\dot{m}'/\bar{m})}{(\dot{p}'/\bar{p})} \quad 73$$

Combining equation 73 and 268 yields

$$R_p = \rho_t \bar{m}^{-1} \sum_{k=1}^S \rho_{o,k}^{-1} \int_{D_0} R_{p,d,k}^* \bar{m}_{d,k} F_k / \zeta_{d,k}^* dD \quad 269$$

where  $R_{pdk}^*$  is the pressure coupled response of the pseudopropellant with diameter between  $D_0$  and  $D_0 + dD_0$  and of oxidizer type  $k$ .

Similarly for the velocity coupled response

$$R_v = \rho_t \bar{m}^{-1} \sum_{k=1}^S \rho_{o,k}^{-1} \int_{D_0} R_{v,d,k}^* \bar{m}_{d,k} F_k / \zeta_{d,k}^* dD \quad 270$$

Equations 269 and 270 provide the formalism for computing the overall composite propellant response functions. All that remains is to determine the pseudopropellant response functions. Note that the use of equations 269 and 270 provides the contingency for predicting oxidizer particle size effects on the nonsteady state combustion. Furthermore, the equations reduce the large scale heterogeneity of the burning

surface such that, to a good approximation, a homogeneous nonsteady model can be employed to calculate the pseudopropellant pressure coupled responses.

#### The Pseudopropellant Pressure Coupled Response Function

Several methods are available for calculating the pressure coupled response of each pseudopropellant: (a) a small perturbation technique can be applied directly to the steady state PEM to determine the pseudopropellant response; (b) the Denison and Baum model for nonsteady burning can be used by calculating the "A" and "B" parameters directly from the steady state combustion model; or (c) the "A" and "B" parameters of the Denison and Baum model can be calculated from the Cohen postulates; and (d), the pseudopropellant response functions can be calculated using the technique of Zeldovich and Novozhilov.

With the exception of the first approach, the above models were discussed in the literature review. The first approach, that of perturbing the steady state PEM, was not employed in the present research program. Method (b) reduces to method (d) and, therefore, was also not included in the present program.

The Cohen Postulate Method. For calculations utilizing method (c), the Cohen postulates were applied to the Denison and Baum pressure coupled response function to obtain the pseudopropellant response functions. The expression for the Denison and Baum pressure coupled response is

$$\frac{1}{n} (R_r + iR_i) = AB/[\lambda + (A/\lambda) - (1 + A) + AB] \quad 76$$



where  $R_r/n$  and  $R_i/n$  are the real and imaginary parts of the pressure coupled response normalized with respect to the burning rate pressure exponent, and the parameter  $\lambda$  is a complex function of the nondimensional frequency,  $\Omega$ . The real part of the complex frequency is

$$\lambda_r = \frac{1}{2} \{1 + (1/\sqrt{2})[(1 + 16\Omega^2)^{1/2} + 1]^{1/2}\} \quad 77$$

The imaginary part is

$$\lambda_i = (1/2\sqrt{2})[(1 + 16\Omega^2)^{1/2} - 1]^{1/2} \quad 78$$

where

$$\Omega = k\rho_t\omega/\dot{m}^2C_p \quad 79$$

$k$  is the thermal conductivity of the propellant,  $\rho_t$  is the total propellant density,  $C_p$  is the specific heat of the propellant and  $\dot{m}$  is the mass flux from the burning surface.

Separating the real and imaginary parts of equation 76, the resulting relation for the real part of the pressure coupled response is

$$\begin{aligned} R_r = & AB(\lambda_r^2 + \lambda_i^2) \{ (\lambda_r^2 + \lambda_i^2)[\lambda_r - (1 + A) + AB] + A\lambda_r \} / \\ & \{ [(\lambda_r^2 + \lambda_i^2)[\lambda_r - (1 + A) + AB] + A\lambda_r]^2 + \\ & [(\lambda_r^2 + \lambda_i^2)[\lambda_r - (1 + A) + AB]^2 + 2(\lambda_r^2 - \lambda_i^2)A\lambda_r \\ & [(\lambda_r - (1 + A)) + AB]^2 \} \end{aligned} \quad 271$$

The frequency at which the response function peaks and the magnitude of the peak of the response function are given by the Cohen postulates

Thus

$$f_p = H r/D_0 \quad 272$$

$$R_p/n = G\alpha/D_0 \quad 273$$

where H and G are proportionality constants and  $\alpha$  is the mass fraction of oxidizer in a particular particle size distribution mode.

Differentiating equation 271 with respect to nondimensional frequency and setting the result equal to zero, results in a fourth equation valid at the frequency where the response peaks. Thus

$$\frac{dR}{d\Omega} = 0 \quad 274$$

Thus, the system reduces to a set of two implicit equations with the two unknowns A and B. The system can be solved by a numerical secant iteration technique to determine A and B for each pseudopropellant in the polydisperse propellant. The resulting pressure coupled response function for each pseudopropellant is then integrated over all particle diameters using equation 269 to determine the pressure coupled response of a polydisperse propellant at a specific frequency. This integration is repeated at finite frequency increments to determine the response as a function of frequency.

The ZN Technique. Method (d), the ZN technique, allows the pseudopropellant response functions to be related to steady state propellant combustion parameters. The ZN technique was described in the literature

review. The expression for the pressure coupled response given by the ZN technique is

$$R_p = \frac{n + (nv - \mu u)Z_1}{1 - u + (v - iu/\Omega)Z_1} \quad 107$$

where

$$u = (T_s^0 - T_0) \left( \frac{\partial \ln r^0}{\partial T_0} \right)_p \quad 97$$

$$v = \left( \frac{\partial T_s}{\partial T_0} \right)_p \quad 98$$

$$n = \left( \frac{\partial \ln r^0}{\partial \ln p} \right) T_0 \quad 99$$

$$\mu = \frac{1}{(T_s^0 - T_0)} \left( \frac{\partial T_s^0}{\partial \ln p} \right) \quad 100$$

The superscript o indicates steady state,  $T_s$  is the surface temperature and  $T_0$  is the initial propellant temperature.

Equation 107 can now be used to determine the pseudopropellant pressure coupled response functions by evaluating the steady state parameters of each pseudopropellant with the steady-state polydisperse petite ensemble combustion model. The polydisperse propellant pressure coupled response can then be determined using equation 269.

#### The Pseudopropellant Velocity Coupled Response Function

The subject of velocity coupled response, although not new, has received very little theoretical treatment in the open literature. The present state of the art of understanding the mechanism for velocity



coupled response is further exemplified by the following statement taken from the JANNAF Erosive Burning/Velocity Coupling Workshop (62):  
".... Velocity coupling could not be discussed due to a lack of knowledge on the subject and/or the unwillingness of researchers working on the subject to present their results...."

The work of Lengellé (43) is one of the few comprehensive treatments of the subject; see the literature review section. The mechanism of velocity coupling proposed by Lengellé represents a logical and physically realistic approach to the velocity coupling problem. Therefore a similar approach was taken in the present research effort. The only difference between the present approach and the approach taken by Lengellé is that the present model is based on a more physically realistic and more complete erosive burning model.

Several methods are available for determining the pseudopropellant velocity coupled response by the Lengellé philosophy. The most rigorous approach is to perturb the steady state PEM erosive burning model, and thus follow the same formalism Lengellé used on the Summerfield (modified for erosive burning by Lengellé) combustion model. This approach involves a very lengthy analysis and was not included in the present research program for that reason.

Another method involves the utilization of the ZN technique. This method can be implemented by replacing all of the pressure terms in the ZN formalism by cross flow velocity. The velocity coupled response is then related to the following steady state erosive burning parameters:

$$u = (T_s^0 - T_0) \left( \frac{\partial \ln r}{\partial T_0} \right)_v \quad 275$$

$$v = \left( \frac{\partial T_s^0}{\partial T_0} \right)_v \quad 276$$

$$n = \left( \frac{\partial \ln r}{\partial \ln v} \right)_{T_0} \quad 277$$

$$\mu = \left( \frac{\partial T_s^0}{\partial \ln v} \right)_{T_0} / (T_s^0 - T_0) \quad 278$$

and the velocity coupled response of a pseudopropellant can be written

$$R_v = \frac{n + (nv - \mu u)Z_1}{1 - u + (v - iu/\Omega)Z_1} \quad 279$$

The present approach for velocity coupling was to employ the closed form relation between pressure coupled response and velocity coupled response in the presence of erosive conditions derived by Lengellé. It is realized that this does not represent an advancement in the state of the art of the modeling of the velocity coupled response. However, this method does offer the capability to estimate the oxidizer particle size effects on the velocity coupled component of the response function (an effect which has not been calculated previously).

The expression which relates pressure and velocity coupled response can be written

$$R_v = 0.9\beta_e AB / \{[\lambda - 1 + A(1/\lambda - 1) + ABC'] - (1/3 + 0.9\beta_e) AB/R_p\} \quad 280$$

where  $\beta_e$  is the erosive strength,  $A$  is the Denison and Baum constant which is dependent on the solid phase, and  $\lambda$  is the complex frequency. The parameter  $C'$  arose in the Lengellé formalism due to the inclusion of surface coupled reactions. Thus

$$C' = 1 + \beta_e + C(1/2 + \beta_e)RT_s/E_s \quad 281$$

where  $R$  is the gas constant,  $T_s$  is the surface temperature and  $E_s$  is the surface decomposition activation energy. The parameter  $C$  is related to the surface heat of pyrolysis and typically has a value less than unity.

In the present analysis it is assumed that the term on the right in equation can be neglected since the parameter  $C$  is less than unity and the surface activation energy is of the order  $10^4$ . Thus, equation 281 becomes

$$C' = 1 + \beta_e \quad 282$$

The above assumption is necessary since the Denison and Baum analysis used to compute the pressure coupled response did not include surface coupled reactions. With the above assumption, the Lengellé pressure coupled response for the case of no cross flow velocity reduces to the Denison and Baum pressure coupled response. Thus, by



utilizing equation 282 for the parameter  $C'$ , equation 280 remains compatible with the pressure coupled response calculation in the limiting case of zero cross flow velocity.

The Velocity Coupled Response Solution Methodology. The erosive burning rate is first calculated by the erosive burning model described in a previous section. The  $A$  and  $B$  constants in equation 280 are then determined for each pseudopropellant by the method used for determining the pressure coupled response. The pressure coupled response,  $R_p$ , of each pseudopropellant is computed by employing the Cohen postulates as in the case of no erosive burning. The erosive strength of each pseudopropellant is calculated with the following expression

$$\beta_e = (r_e - r_n)/r_n \quad 283$$

where  $r_e$  is the pseudopropellant burning rate in the presence of erosive conditions and  $r_n$  is the pseudopropellant burning rate in the absence of a cross flow velocity. The parameter  $C'$  is also calculated for each pseudopropellant.

The velocity coupled response of each pseudopropellant can then be calculated by equation 280. The overall polydisperse propellant velocity coupled response is computed by integrating the pseudopropellant velocity coupled response over all pseudopropellants by equations 270.

Thus

$$R_v = \rho_t^{-1} \sum_{k=1}^S \rho_{0,k}^{-1} \int_{D_0} R_{v,d,k}^* m_{d,k}^* F_k / \zeta_{d,k} dD_0 \quad 270$$

The integration indicated above is repeated at finite frequency increments to determine the velocity coupled response as a function of frequency.

## ANALYTICAL RESULTS

### Introduction

The results of calculations with the theoretical model for the combustion of composite solid propellants are divided into four parts. They are the steady state burning rate, the erosive burning rate, the pressure coupled response and the velocity coupled response results. The results of calculations with the steady state burning rate and the pressure coupled response model were compared to available experimental data. However, experimental data containing an adequate description of the propellant's composition in terms of particle size and size distribution were not available for comparison with the results of calculations for the erosive burning or velocity coupling models.

### Steady State PEM Burning Rate Results

The PEM, not unlike the earlier BDP model and other burning rate models, relies on the numerical value of several constants whose magnitude are known only to a small degree of precision. The constants include activation energies, pre-exponential factors, reaction orders, heats of reaction, specific heats, thermal conductivities, etc., for the various flames, gas and solid phase reactions.

In order to determine the appropriate values for these input constants, the experimental burning rate data presented by Miller (6,7) was used. Miller determined the burning rate and pressure exponent for a series of AP/HTPB non-metalized propellants at a pressure of 68.03 atm



and an initial temperature of 294°K. These composite propellants were formulated from eight individual oxidizer grinds with the total oxidizer mass fraction held constant at 87.4 percent for each blend. Figure 19 presents the particle size distribution as weight percent less than diameter versus particle diameter for some of the oxidizer grinds used in the Miller formulations. The solid lines through the data points represent a least squares fit of the measured particle size distribution to a log normal distribution function. The values of the weight median diameters,  $\bar{D}$ , and the distribution width parameter,  $\sigma$ , are presented in Table 1 for each of the oxidizer grinds. Also appearing in Table 1 are the standard deviations of error for the log normal fit of each of the grinds. Thus, the particle size distributions of the eight grinds are accurately represented by the log normal approximations.

Table 1  
Correlation for the Log Normal Distributions

Nominal Diameter ( $\mu$ )	$\bar{D}(\mu)$	$\sigma(\mu)$	Std. Dev. (%)
400	448.0	1.222	.775
200	195.0	1.628	3.079
90	71.0	1.370	2.382
50	44.2	1.445	.979
20	22.6	1.676	2.075
10	10.8	1.808	2.830
6	5.23	1.878	1.041
2	1.89	1.305	1.134
0.7	.686	2.716	2.204

The twenty-five Miller propellants are essentially five similar groups of five families of propellants (in terms of the oxidizer particle size distribution). The families range from very broad overall distributions to very narrow distributions, all with the same percentage of oxidizer. The compositional grid for the twenty-five propellants are presented in Table 2. The total percentage of oxidizer for each propellant equals 87.4, a constant for all of the propellants.

The burning rate and the burning rate pressure exponents determined by Miller for the twenty-five propellants are presented in Table 3. Those propellants for which no data are presented are propellants that presented problems during the propellant mixing operation.

The results of calculations with the PEM are presented in Figures 30 and 31. Figure 30 depicts the theoretical burning rate versus the experimental burning rate for the twenty-one propellant configurations considered, and Figure 31 depicts the theoretical pressure exponent versus the experimental exponent for the same propellants. In both cases, the PEM prediction matched the experimental data quite well with over seventy-five percent of the data being within ten percent of the predicted values. The PEM input parameters used for the above calculations are presented in Table 4.

In addition to the parameters listed in Table 4, the flame temperatures for the primary and final flames were calculated with the NASA equilibrium thermochemistry program (63). The flame temperatures are stored in the PEM computer code in tabular form as a function of combustion pressure and propellant composition. Quadratic interpolating polynomials are used to retrieve data at pressures and compositions between the tabular grid points.

Table 2

## Miller Propellant Compositional Grid

Propellant Designation	Per Cent Nominal Particle Size							
	400	200	90	50	20	6	2	0.7
SD III-88-1	-	-	-	-	45.26	31.58	-	10.53
SD III-88-2	-	-	31.58	-	13.68	-	-	42.11
SD III-88-3	-	-	-	-	55.79	-	-	31.58
SD III-88-4	-	31.58	-	-	24.21	-	-	31.58
SD III-88-5	42.11	-	-	-	13.68	-	-	31.58
SD III-88-6	-	-	-	31.58	13.68	31.58	10.53	-
SD III-88-7	-	-	31.58	-	13.68	-	42.11	-
SD III-88-8	-	-	-	31.58	24.21	-	31.58	-
SD III-88-9	-	31.58	-	-	24.21	-	31.58	-
SD III-88-10	42.21	-	-	-	13.68	-	31.58	-
SD III-88-11	-	-	-	-	45.26	42.11	-	-
SD III-88-12	-	-	31.58	-	13.68	42.11	-	-
SD III-88-13	-	-	-	-	55.79	31.58	-	-
SD III-88-14	-	31.58	-	-	24.21	31.58	-	-
SD III-88-15	42.11	-	-	-	13.68	31.58	-	-
SD III-88-16	-	31.58	-	31.58	24.21	-	-	-
SD III-88-17	-	-	31.58	-	55.79	-	-	-
SD III-88-18	-	-	42.11	-	45.26	-	-	-
SD III-88-19	-	31.58	-	-	55.79	-	-	-
SD III-88-20	42.11	-	-	-	45.26	-	-	-
SD III-88-21	31.58	31.58	-	10.53	13.68	-	-	-
SD III-88-22	31.58	-	-	42.11	13.68	-	-	-
SD III-88-23	-	42.11	-	31.58	13.68	-	-	-
SD III-88-24	-	31.58	-	42.11	13.68	-	-	-
SD III-88-25	42.11	-	-	31.58	13.68	-	-	-



Table 3

Strand Burning Rate of the Miller Propellant Compositions at 1000 psia

Propellant Designation	Burning Rate (cm/sec)	Pressure Exponent (psi)
SD III-88-1	-	-
SD III-88-2	2.977	0.916
SD III-88-3	3.636	0.689
SD III-88-4	2.847	0.797
SD III-88-5	2.253	0.928
SD III-88-6	2.903	0.621
SD III-88-7	-	-
SD III-88-8	2.786	0.692
SD III-88-9	2.743	0.771
SD III-88-10	2.278	0.841
SD III-88-11	-	-
SD III-88-12	2.626	0.617
SD III-88-13	-	-
SD III-88-14	2.477	0.613
SD III-88-15	1.824	0.690
SD III-88-16	1.417	0.451
SD III-88-17	2.118	0.474
SD III-88-18	1.803	0.437
SD III-88-19	1.974	0.529
SD III-88-20	1.405	0.610
SD III-88-21	.828	0.430
SD III-88-22	1.316	0.458
SD III-88-23	1.171	0.463
SD III-88-24	1.364	0.449
SD III-88-25	1.120	0.528

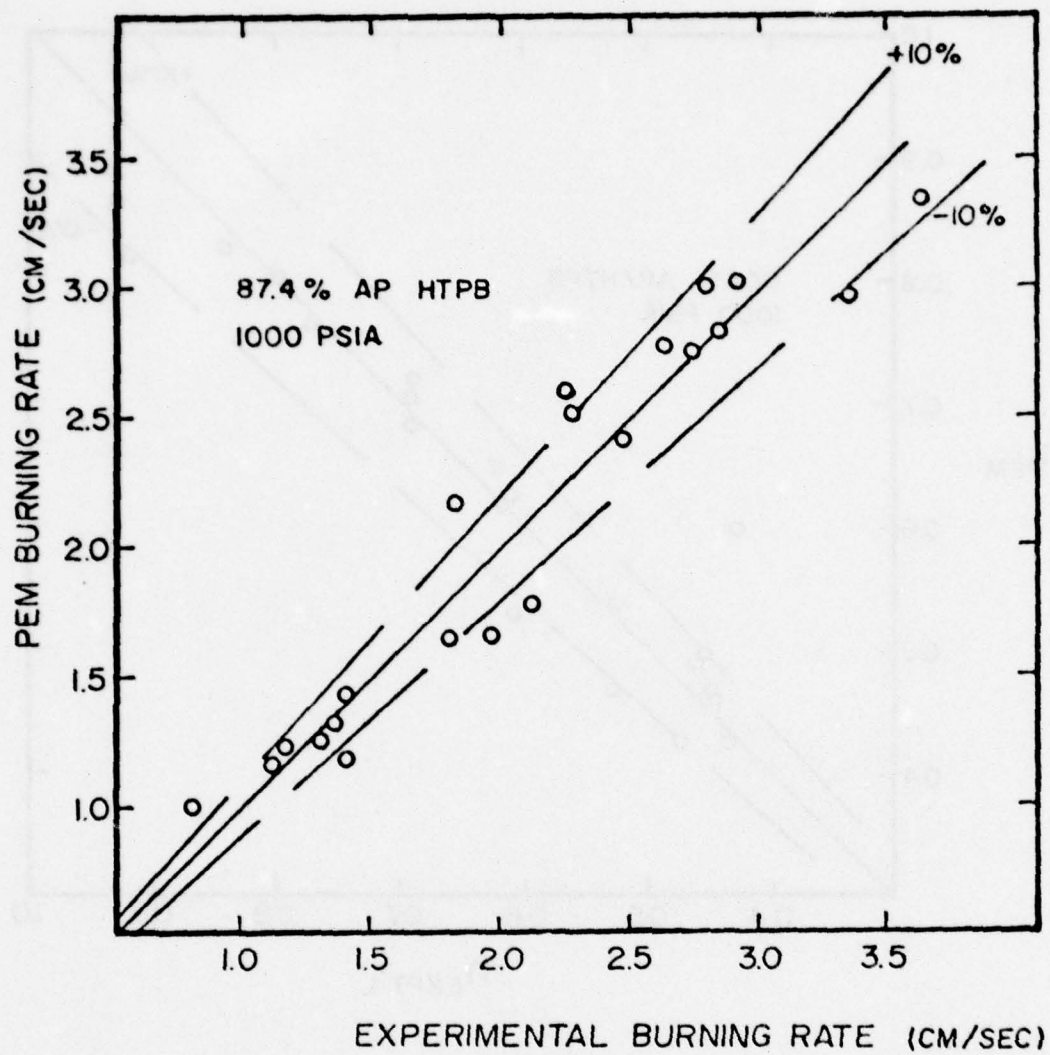


Figure 30. A Comparison of PEM Burning Rate with Experimental Burning Rate: Miller Data

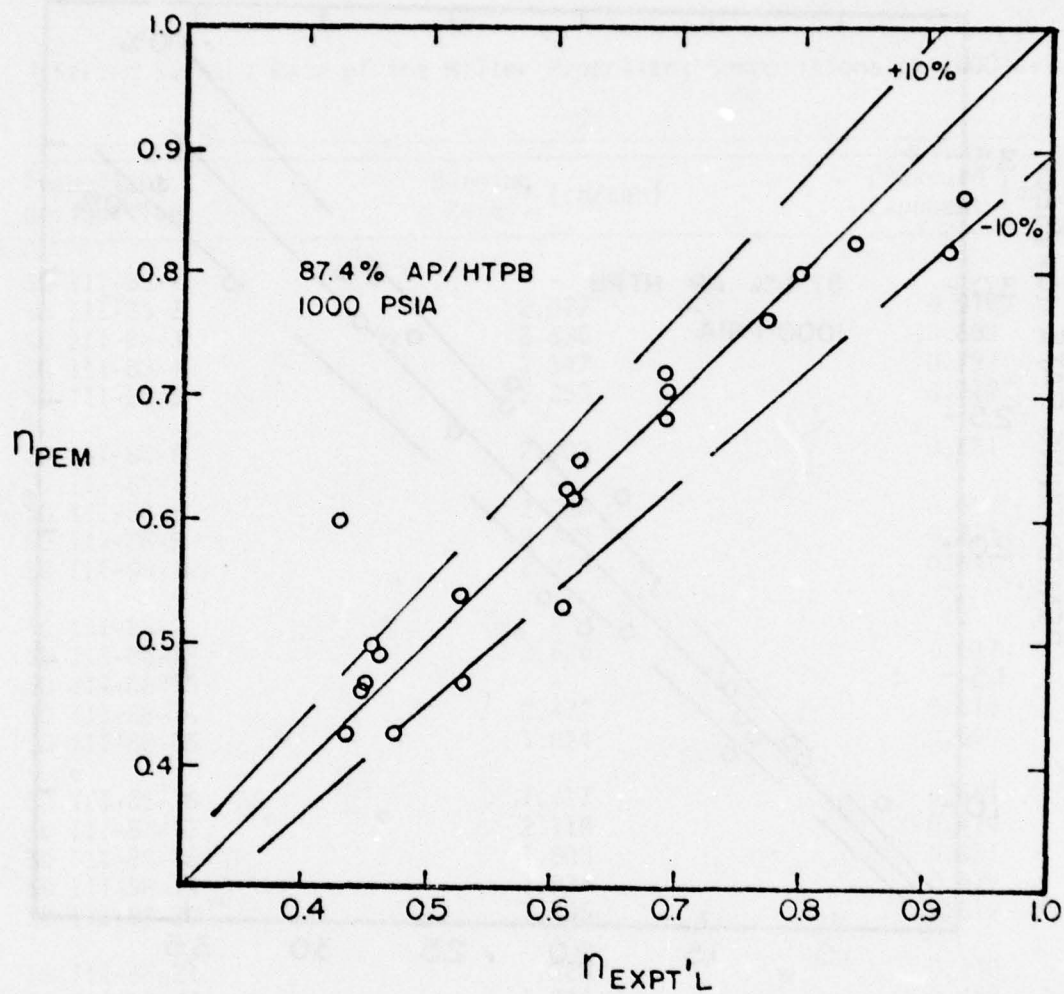


Figure 31. A Comparison of PEM Burning Rate Pressure Exponent with Experimental Data of Miller



Table 4

## PEM Input Parameters for the Miller Propellants

Description of Parameter	Value	Units
Number of oxidizer types	1	-
Start Pressure	34.0136	atm.
Stop pressure	136.0544	atm.
Number of pressure points	3	-
Maximum number of terms in series solution	50	--
Maximum error in series solution	.0000001	--
Number of integration steps for rate calculation	40 - 50	-
Fuel volume parameter from $V_f = CD_0^n$	3.0	-
Diameter to start integration	.1	microns
Diameter to stop integration	1100.0	microns
Fuel binder	HTPB	-
Initial propellant temperature	294.15	°K
Mass fraction of oxidizer	.8737	-
Heat of pyrolysis of fuel	433.0	cal/gm
Density of fuel	.9030	gm/cm <sup>3</sup>
Pre-exponential for fuel surface decomposition	4000	gm/cm <sup>2</sup> -sec
Activation energy for fuel surface decomposition	16,900.0	cal/mole
Oxidizer type	AP	-
Molecular weight of final flame products	20.78	gm/mole
Final flame stoichiometry variable	4.18	-
Primary flame stoichiometry variable	3.0	-
Molecular weight of primary flame products	28.0	gm/mole
Oxidizer heat of pyrolysis	-120.0	cal/gm
Density of oxidizer	1.95	gm/cm <sup>3</sup>
Arrhenius factor for oxidizer decomposition	$4 \times 10^5$	gm/cm <sup>2</sup> -sec
Activation energy for oxidizer decomposition	23000.0	cal/mole
AP Flame temperature at 100 psia	1388.0	°K
AP Flame temperature at 2000 psia	1413.0	°K

Table 4 Continued

Description of Parameter	Value	Units
Oxidizer ignition delay proportionality factor	190.0	sec atm <sup>m</sup> / cm <sup>s</sup>
Oxidizer ignition delay pressure exponent (m)	.721	-
Oxidizer ignition delay diameter exponent (x)	.80	-
Activation energy for primary flame	15,000	cal/mole
Activation energy for AP flame	29,000	cal/mole
Arrhenius frequency factor for primary flame	188.0	sec <sup>-1</sup>
Arrhenius frequency factor for AP flame	70,000	sec <sup>-1</sup>
Primary flame reaction order	2.0	-
AP flame reaction order	1.8	-
Specific heat of solid and gases	.3	cal/gm °K
Thermal conductivity of gases	.003	cal/cm-sec- °K
Diffusion parameter	$7.6 \times 10^{-6}$	-
Average Diffusion flame standoff parameter	.3	-

The effect of oxidizer particle size on the polydisperse propellant burning rate can be demonstrated by presenting the pseudopropellant mean state burning rate and pressure exponent as a function of oxidizer particle size. Figure 32 presents pseudopropellant burning rate versus oxidizer diameter and Figure 33 presents the pseudopropellant pressure exponent versus oxidizer diameter.

#### Erosive Burning Results

The PEM erosive burning model, not unlike the PEM steady state burning rate model, requires a very complete description of the propellant composition in order to make quantitative predictions. Especially important is a complete description of the oxidizer particle size distribution.

In the past, experimental results have not attempted to systematically correlate erosive burning characteristics with propellant composition. Furthermore, current erosive burning data is incomplete in regard to a complete description of the propellant composition. Therefore, it was not practical to attempt a quantitative comparison of the theoretical erosive burning results with experimental results. However, in order to illustrate that the PEM erosive burning model does indeed predict the experimentally observed trends, the model was employed to predict the erosive burning characteristics of a "computer propellant".

The computer propellant considered was a composite containing 87.4 percent ammonium perchlorate with a HTPB fuel binder. The constants used for the Miller propellants as listed in Table 4 were also employed in the computer propellant.



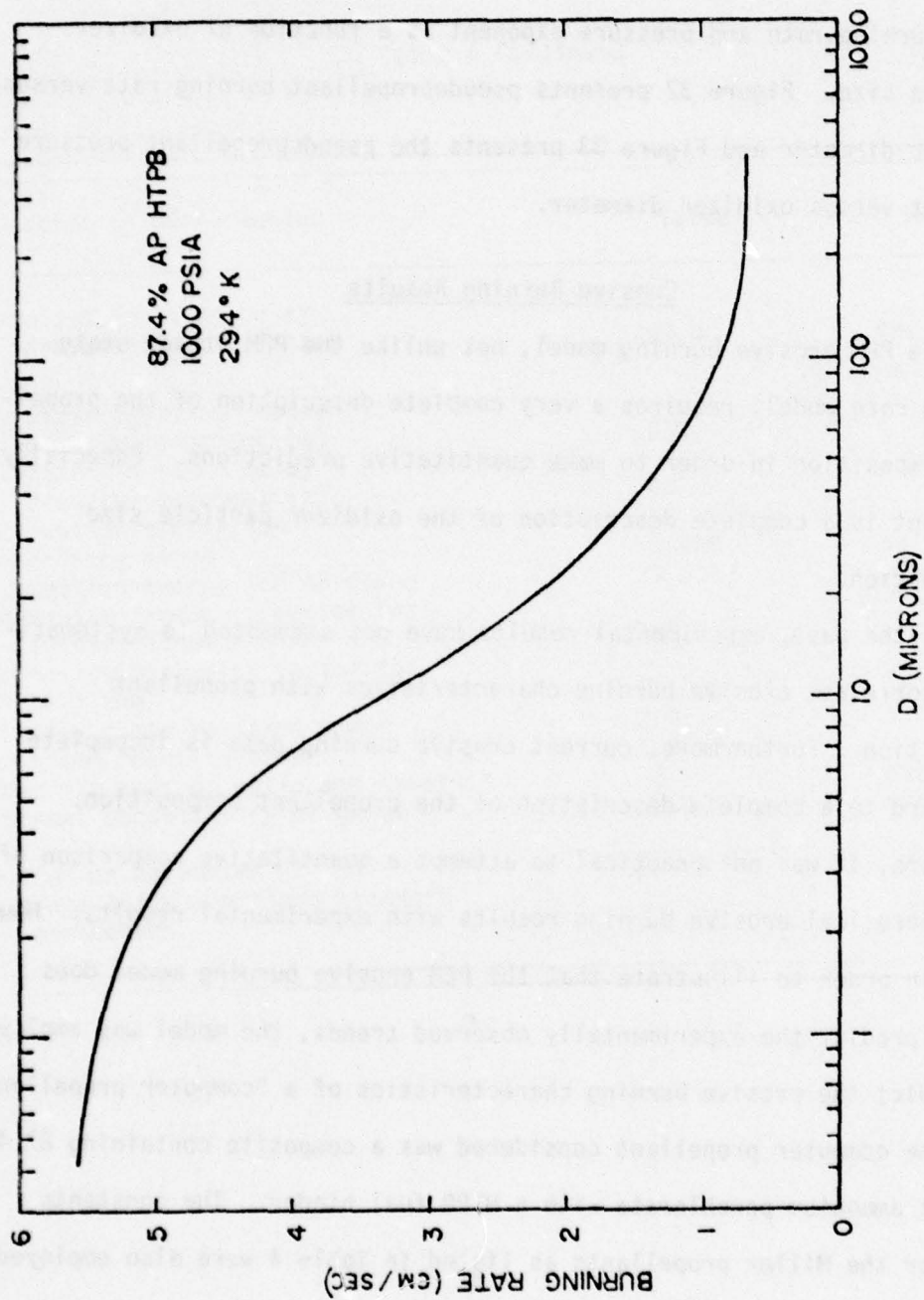


Figure 32. The Pseudopropellant Burning Rate Versus Oxidizer Particle Diameter

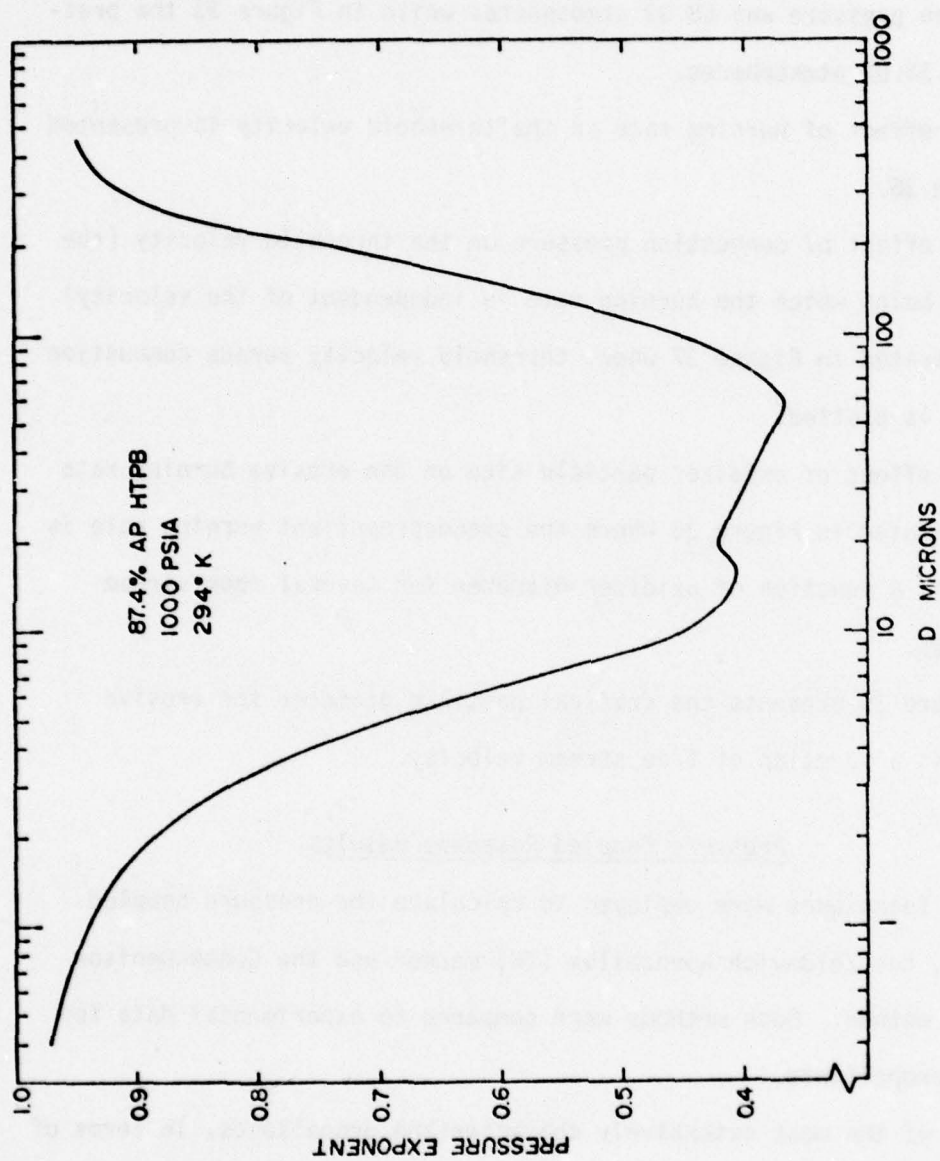


Figure 33. The Pseudopropellant Burning Rate Pressure Exponent Versus Oxidizer Particle Diameter

The effect of free stream velocity on the propellant burning rate is depicted in Figures 34 and 35, where the propellant burning rate is plotted as a function of the free stream velocity. In Figure 34 the combustion pressure was 68.03 atmospheres while in Figure 35 the pressure was 34.02 atmospheres.

The effect of burning rate on the threshold velocity is presented in Figure 36.

The effect of combustion pressure on the threshold velocity (the velocity below which the burning rate is independent of the velocity) is illustrated in Figure 37 where threshold velocity versus combustion pressure is plotted.

The effect of oxidizer particle size on the erosive burning rate is illustrated in Figure 38 where the pseudopropellant burning rate is plotted as a function of oxidizer diameter for several free stream velocities.

Figure 39 presents the critical particle diameter for erosive burning as a function of free stream velocity.

#### Pressure Coupled Response Results

Two techniques were employed to calculate the pressure coupled response, the Zeldovich Novozhilov (ZN) method and the Cohen-Denison and Baum method. Both methods were compared to experimental data for several propellants.

One of the most extensively characterized propellants, in terms of nonsteady combustion, is A-13 propellant. That propellant is composed of 20.4 percent PBAN, 76.0 percent ammonium perchlorate and 3.6 percent open 828 resin. The ammonium perchlorate consists of a monomodal



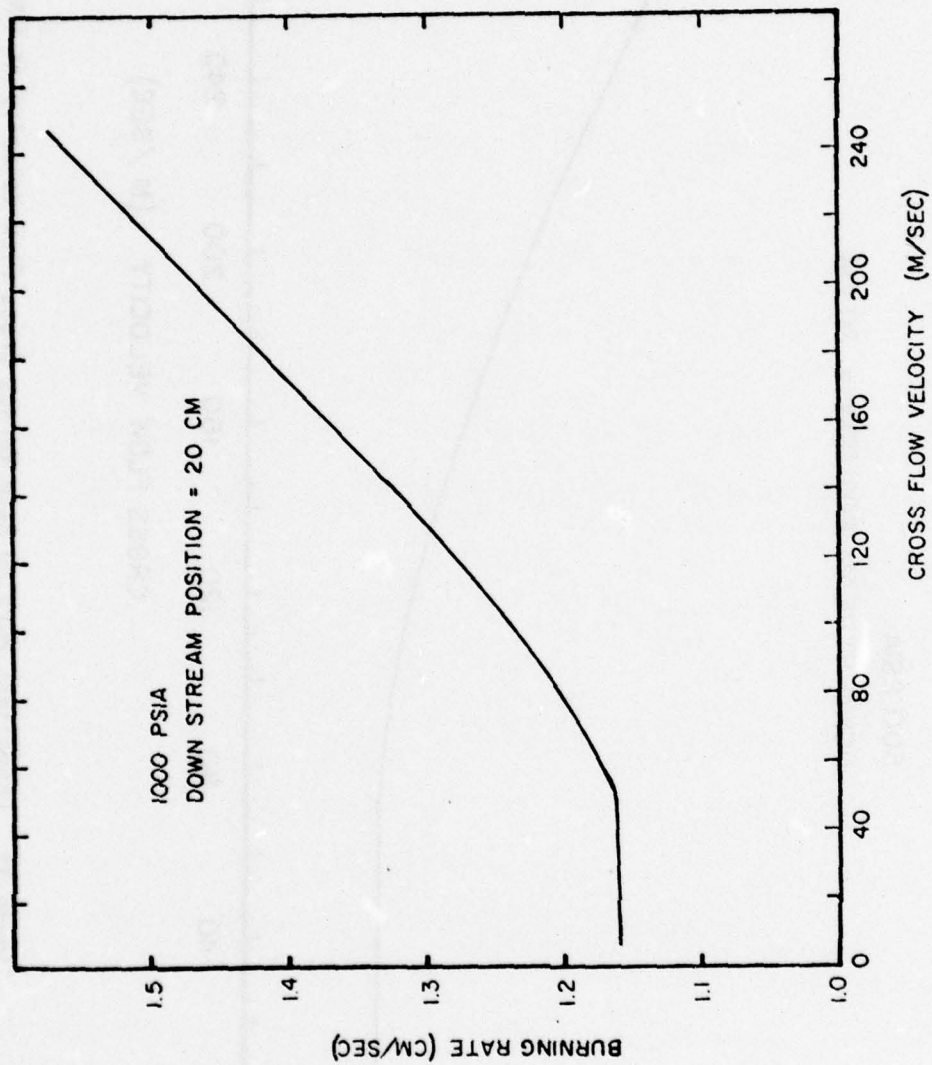


Figure 34. Propellant Burning Rate Versus Cross Flow Velocity at 1000 psia

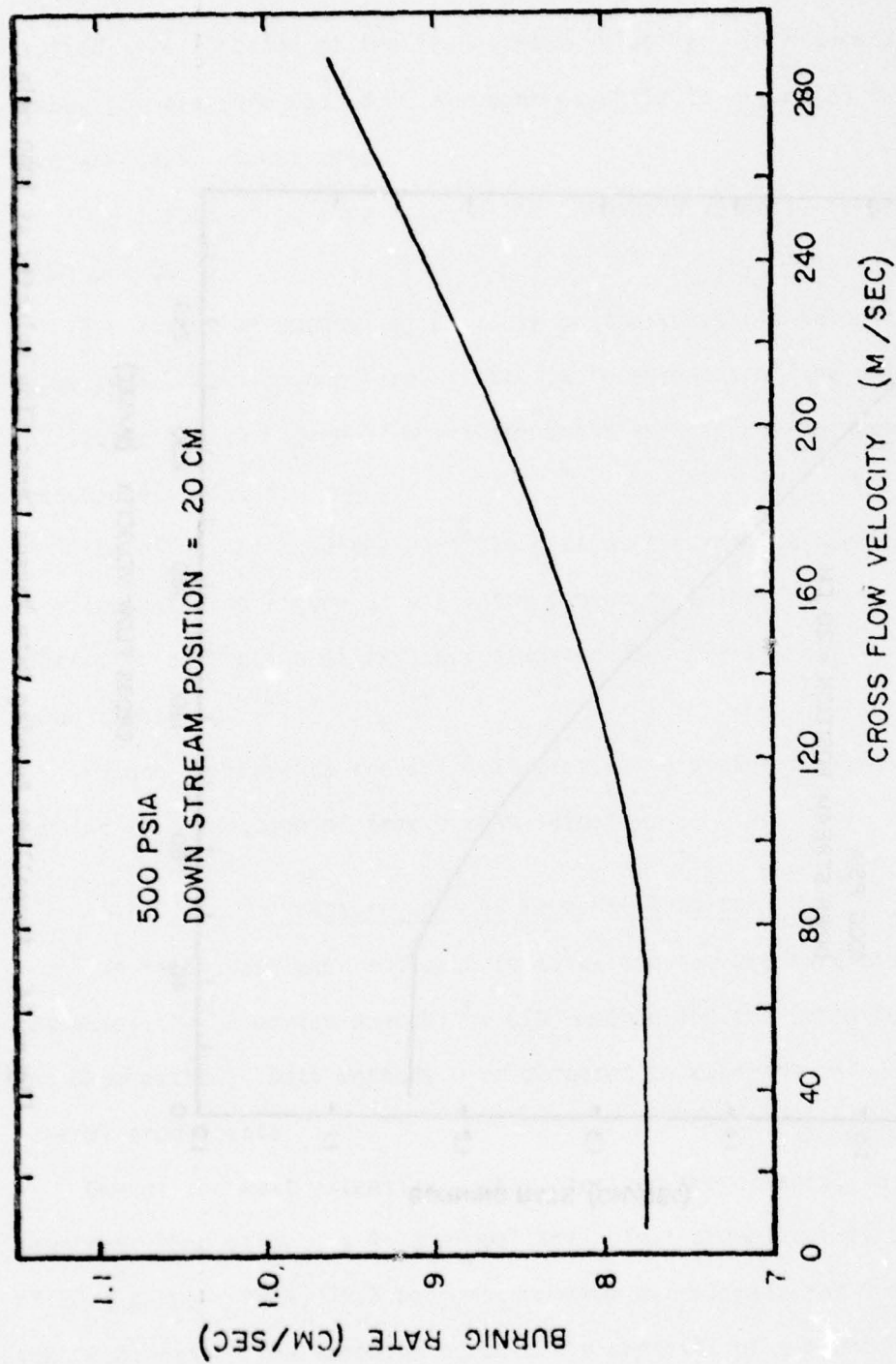


Figure 35. Propellant Burning Rate Versus Cross Flow Velocity at 500 psia

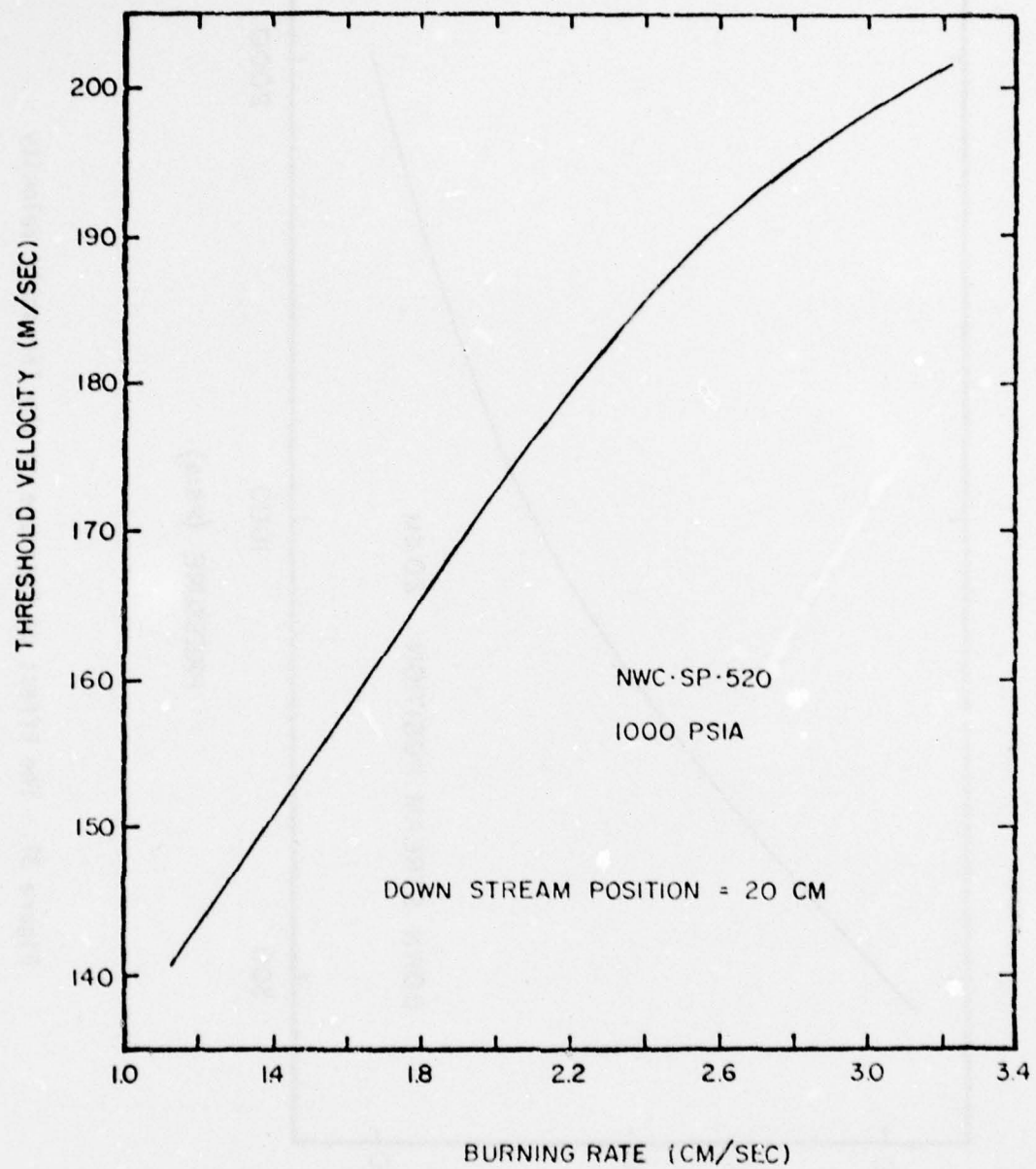


Figure 36. The Effect of Burning Rate on the Threshold Velocity



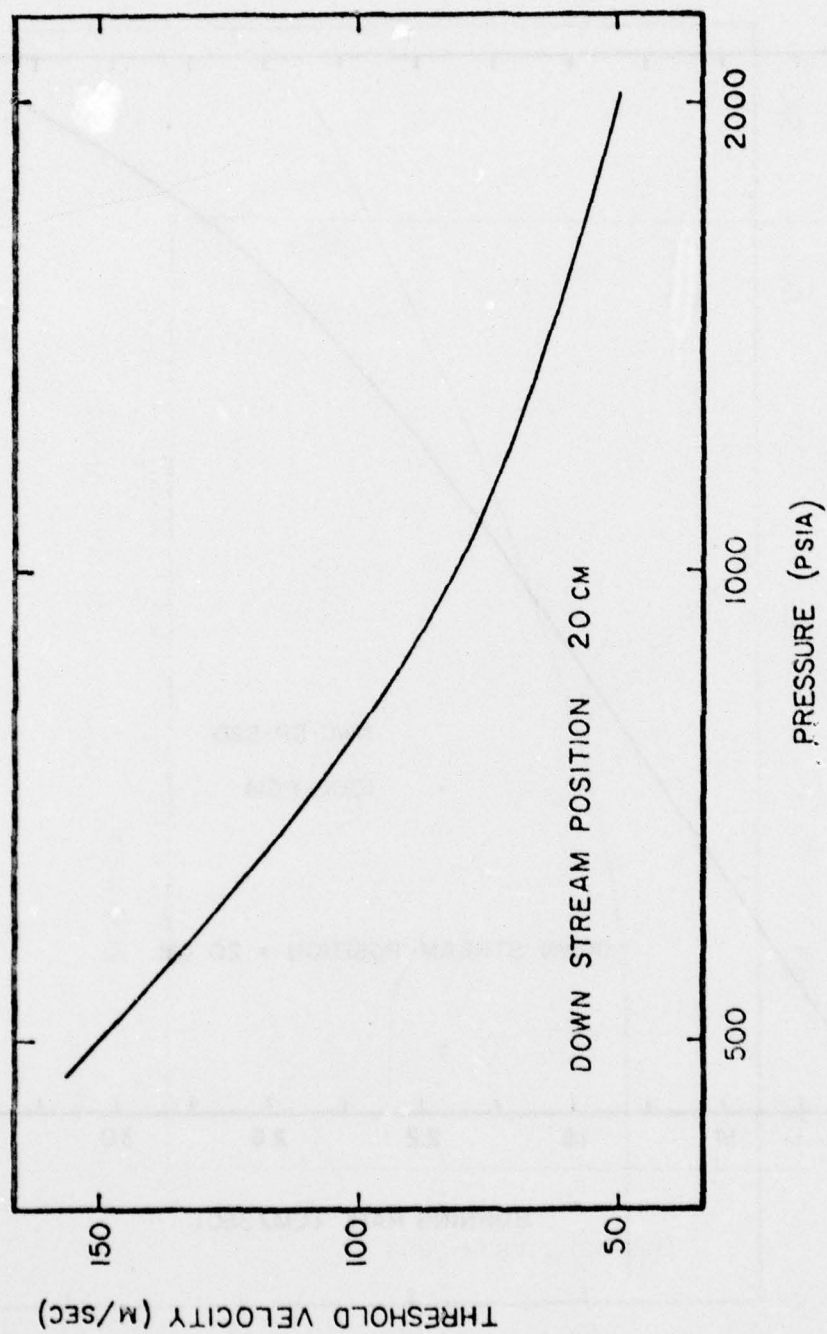


Figure 37. The Effect of Pressure on the Threshold Velocity

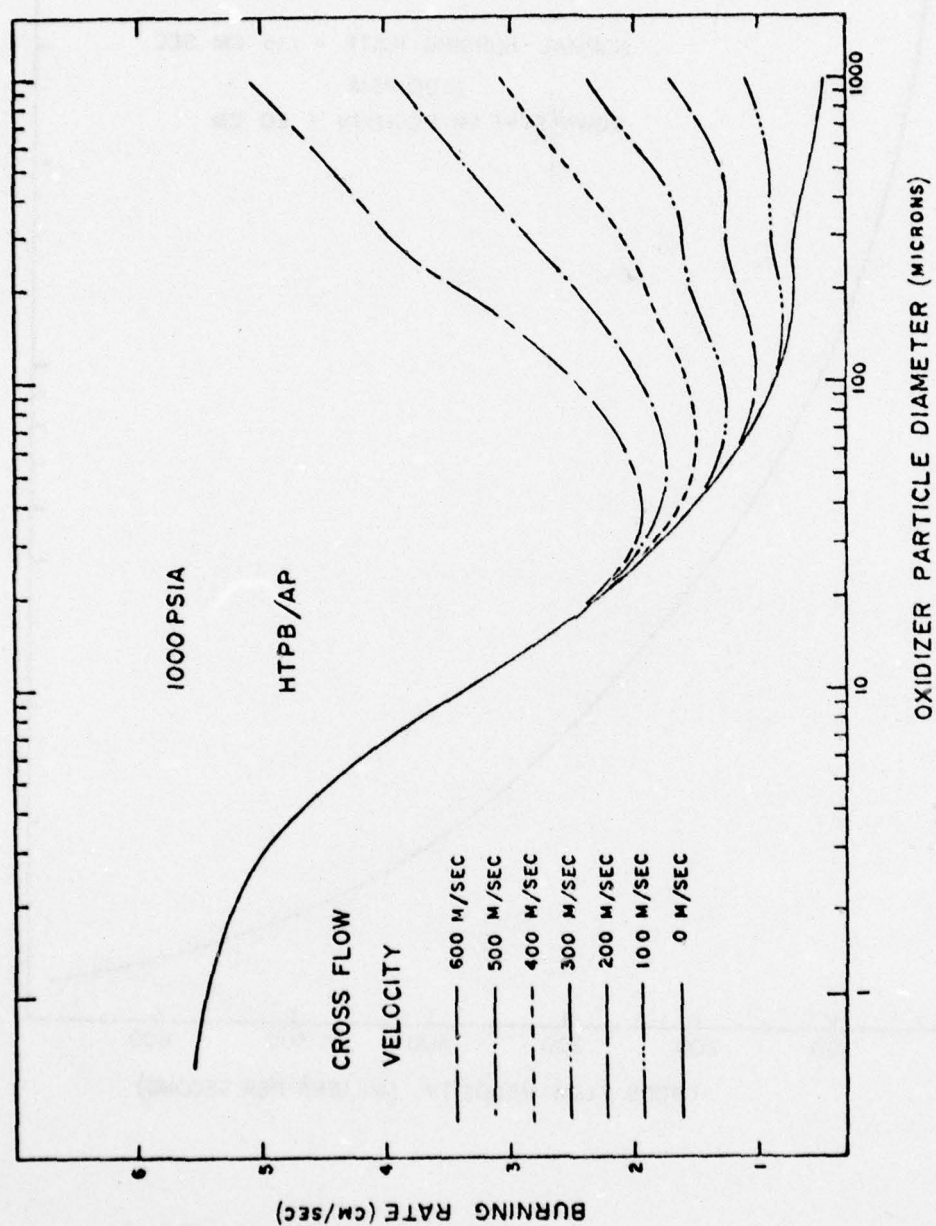


Figure 38. The Effect of Oxidizer Particle Size on the Pseudopropellant Erosive Burning Rate

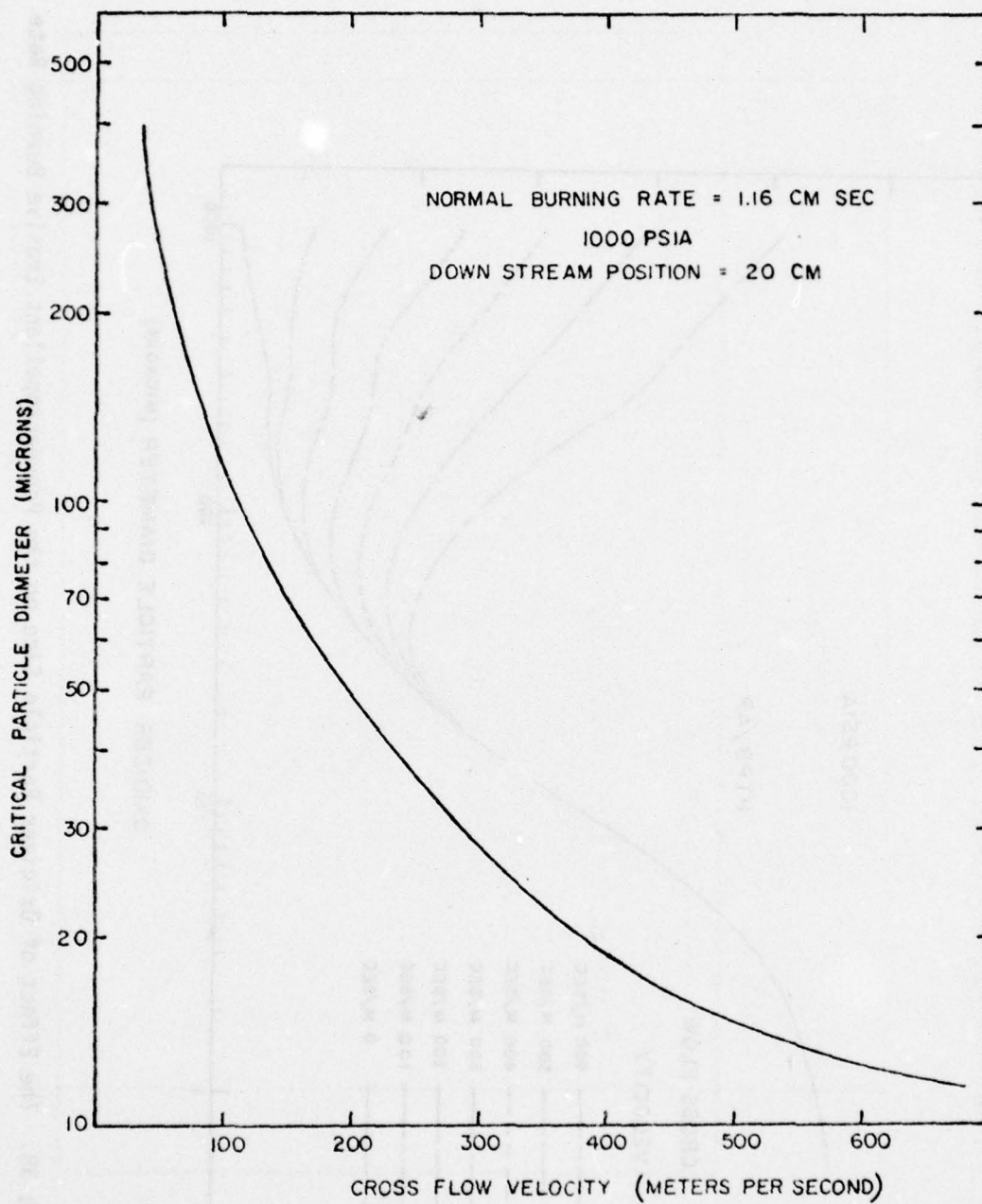


Figure 39. The Critical Particle Diameter for Erosive Burning Versus Free Stream Velocity



particle size distribution with a 90 micron nominal weight median diameter. Experimental measurements of the actual oxidizer particle size distribution have not been reported. However, normal 90 micron grinds typically have a distribution width parameter of 1.4 and a weight median diameter of 71 microns.

The above particle size distribution parameters were used for the theoretical prediction of the pressure coupled response of the A-13 propellant.

Figure 40 compares the results of calculations of the pressure coupled response of A-13 propellant utilizing the Cohen-Denison and Baum method to the experimental results (48) for that propellant. The proportionality constants in equations 83 and 84 used for this calculation were those used by Cohen in reference (1).

Figure 41 presents a comparison of the results of calculations using the ZN technique to the experimental data for A-13 propellant.

Another well characterized propellant is NWC-SP-520. Pressure coupled response data over a wide frequency range as well as complete formulation data were available (64) for this propellant.

NWC-SP-520 propellant is composed of 13.1 percent HTPB binder and 86.9 percent ammonium perchlorate. The ammonium perchlorate consisted of a trimodal blend of oxidizer grinds. The oxidizer particle size distribution data is in Table 5.

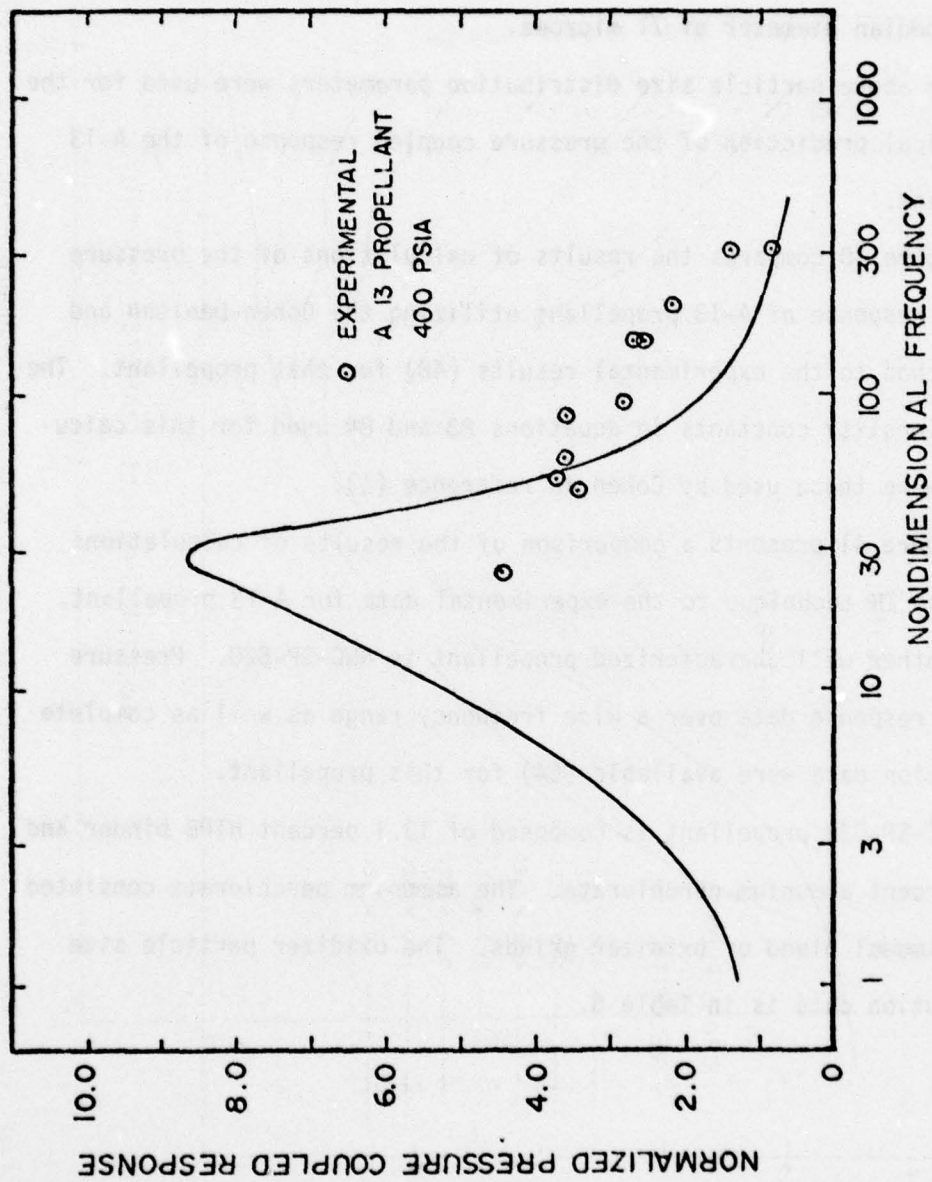


Figure 40. The Real Part of the Normalized Response Function Versus Nondimensional Frequency; Comparison of the Cohen - Denison and Baum Method with the Experimental Results of A-13 Propellant

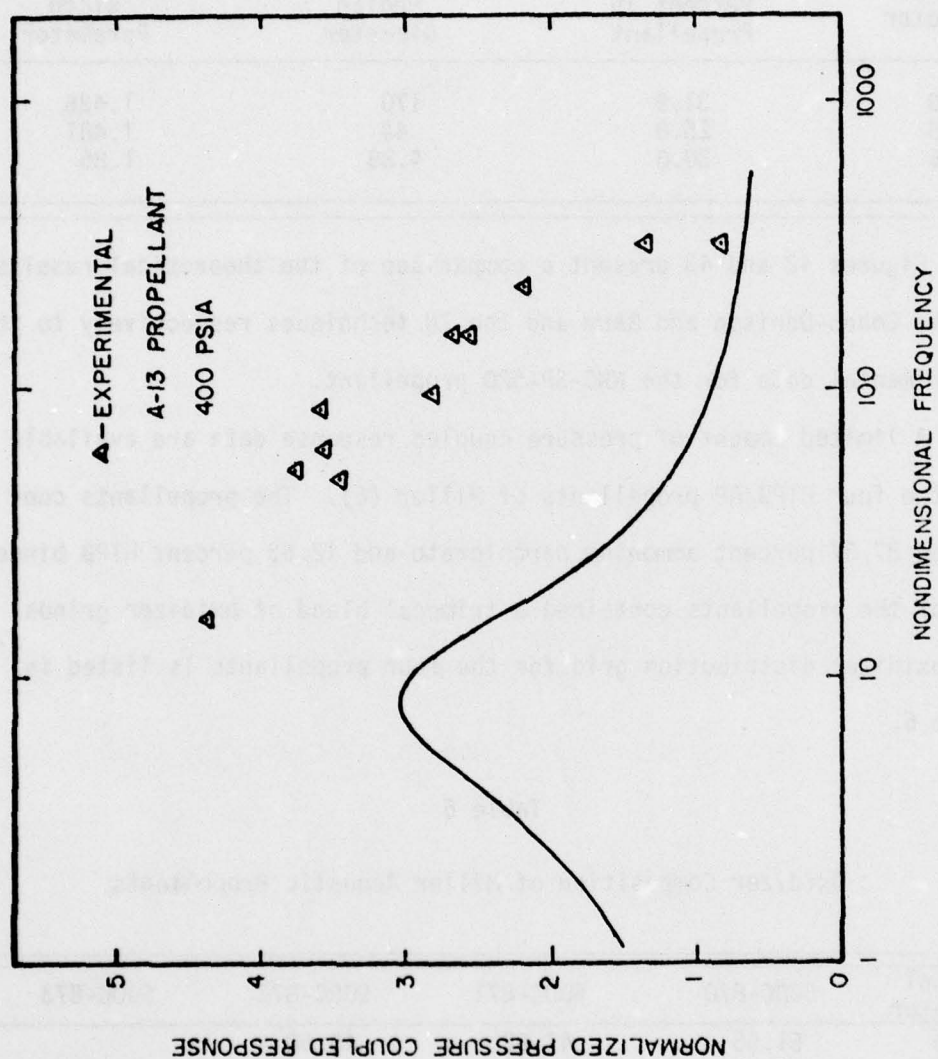


Figure 41. The Real Part of the Normalized Response Function Versus Nondimensional Frequency; Comparison of ZN Method to the Experimental Results of A-13 Propellant



Table 5

## Oxidizer Particle Size Distribution Data for NWC-SP-520

Nominal Diameter	Weight Percent in Propellant	Weight Median Diameter	Distribution Width Parameter
200	31.9	170	1.426
45	25.0	44	1.481
6	30.0	4.85	1.85

Figures 42 and 43 present a comparison of the theoretical results of the Cohen-Denison and Baum and the ZN techniques respectively to the experimental data for the NWC-SP-520 propellant.

A limited amount of pressure coupled response data are available for the four HTPB/AP propellants of Miller (6). The propellants contained 87.37 percent ammonium perchlorate and 12.63 percent HTPB binder. All of the propellants contained a trimodal blend of oxidizer grinds. The oxidizer distribution grid for the four propellants is listed in Table 6.

Table 6

## Oxidizer Composition of Miller Acoustic Propellants

Nominal Diameter	50DC-870	50DC-871	50DC-872	50DC-873
400	51.55	47.62	43.68	
200				63.61
90			31.45	
50		11.36		12.93
20	21.84	28.39		
10				10.83
6			12.24	
2	13.98			

The particle size data for the oxidizer grinds in the above propellants are presented in Table 1.

Figure 44 presents the results of pressure coupled response calculations for the four propellants using the Cohen-Denison and Baum technique while Figure 45 presents the results of the same calculations using the ZN technique. Only one experimental data point was available for each propellant.

In an attempt to illustrate the dramatic effect the oxidizer particle size distribution can have on the pressure coupled response, theoretical calculations were performed for two "computer propellants". The propellants were representative of candidate propellants for the Maverick missile propulsion system. Both of the propellants were composed of 14 percent HTPB binder and 86 percent ammonium perchlorate having a bimodal blend; 70 percent of the blend being of 192 micron weight median diameter and 30 percent being of 16.6 micron weight median diameter. The only difference between the two propellants is in the width of the particle size distributions in the two distribution modes contained in the overall distribution. One propellant had distribution width parameters of 2.0 for the 16.6 micron grind and 2.0 for the 192 micron grind while the other propellant had distribution width parameters of 4.0 for the 16.6 micron grind and 1.6 for the 192 micron grind.

The results of the theoretical calculations for the above two propellants are presented in Figure 46.

The effect of particle size on pressure coupled response is further exemplified in Figure 47 where the real part of the pseudopropellant response is presented as a function of oxidizer particle size for several frequencies.

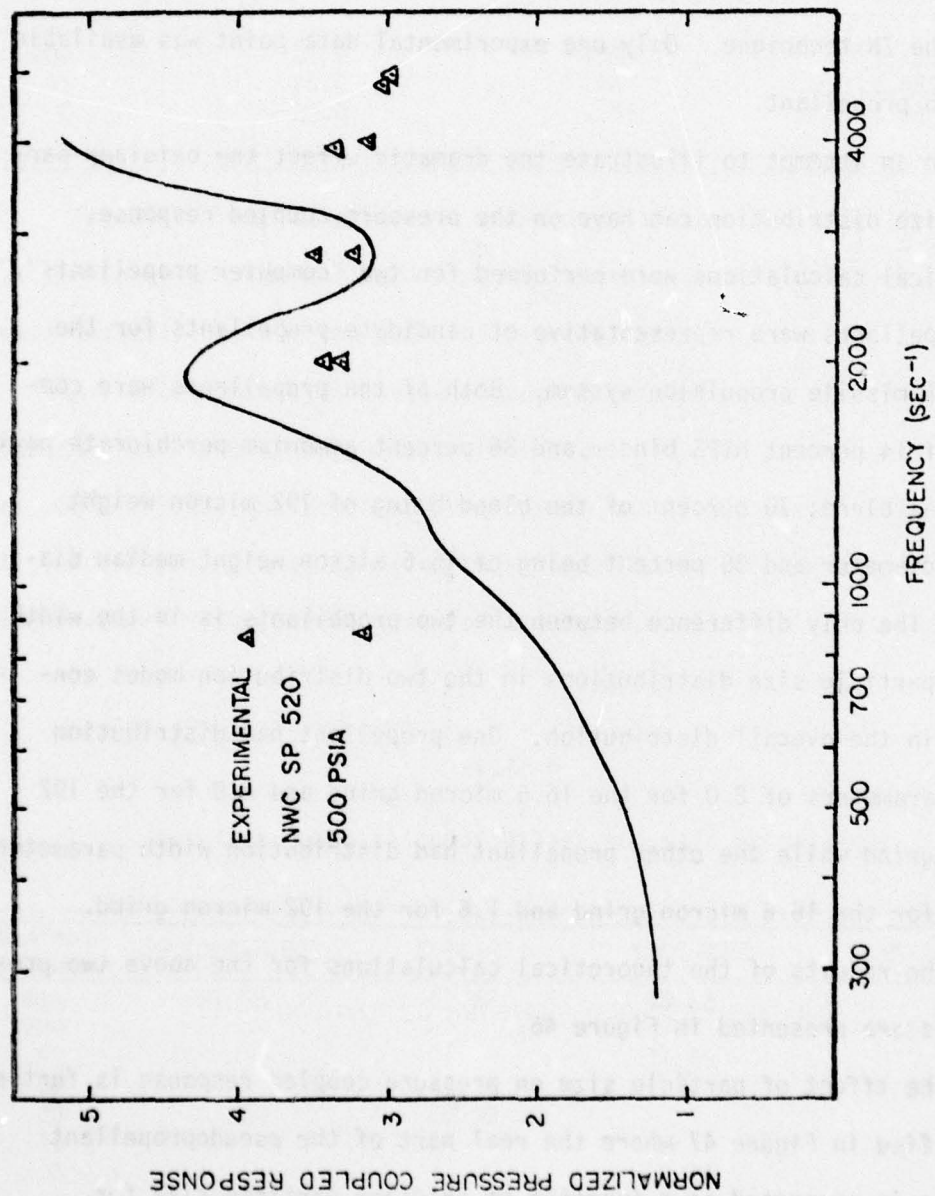


Figure 42. Comparison of the Theoretical Results with the Cohen - Denison and Baum Method to Experimental Pressure Coupled Response Data of NWC-SP-520 Propellant



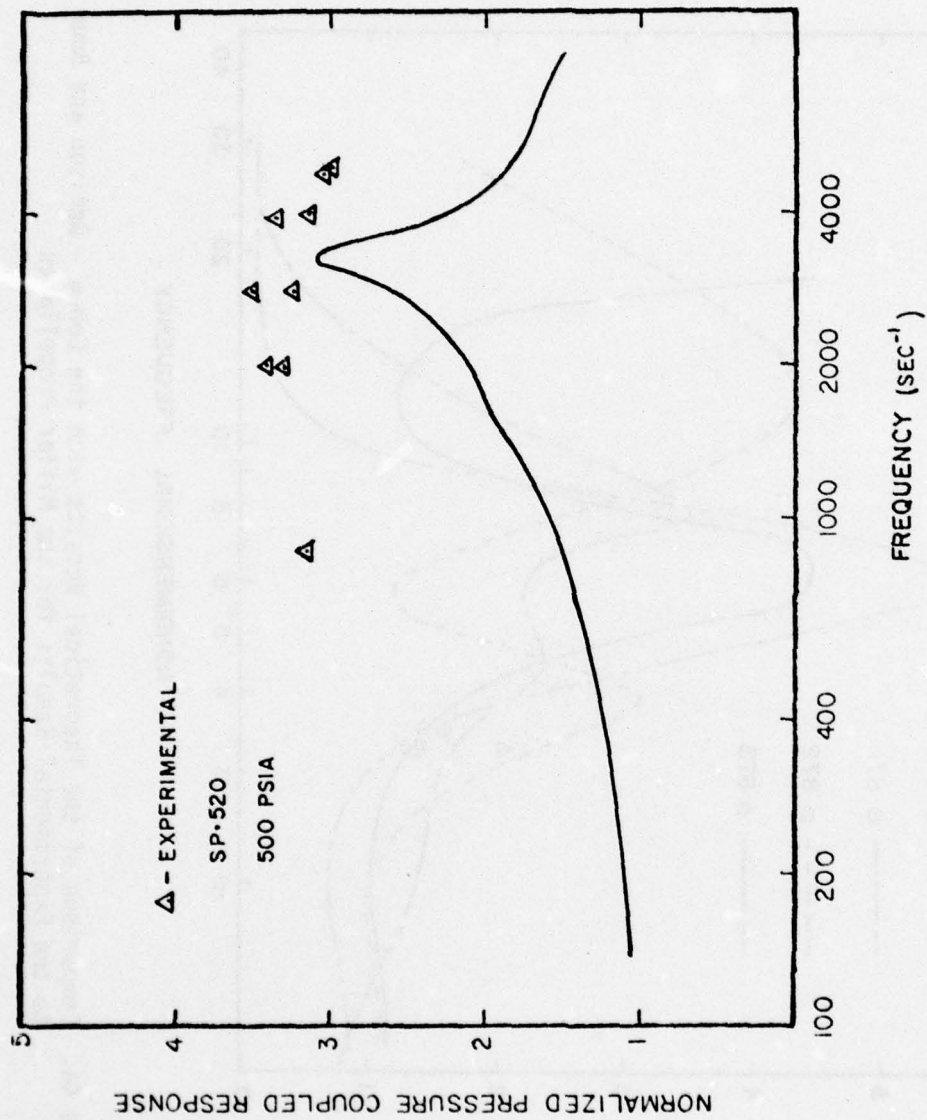


Figure 43. Comparison of the Theoretical Results with the ZN Method to the Experimental Results for NWC-SP-520 Propellant

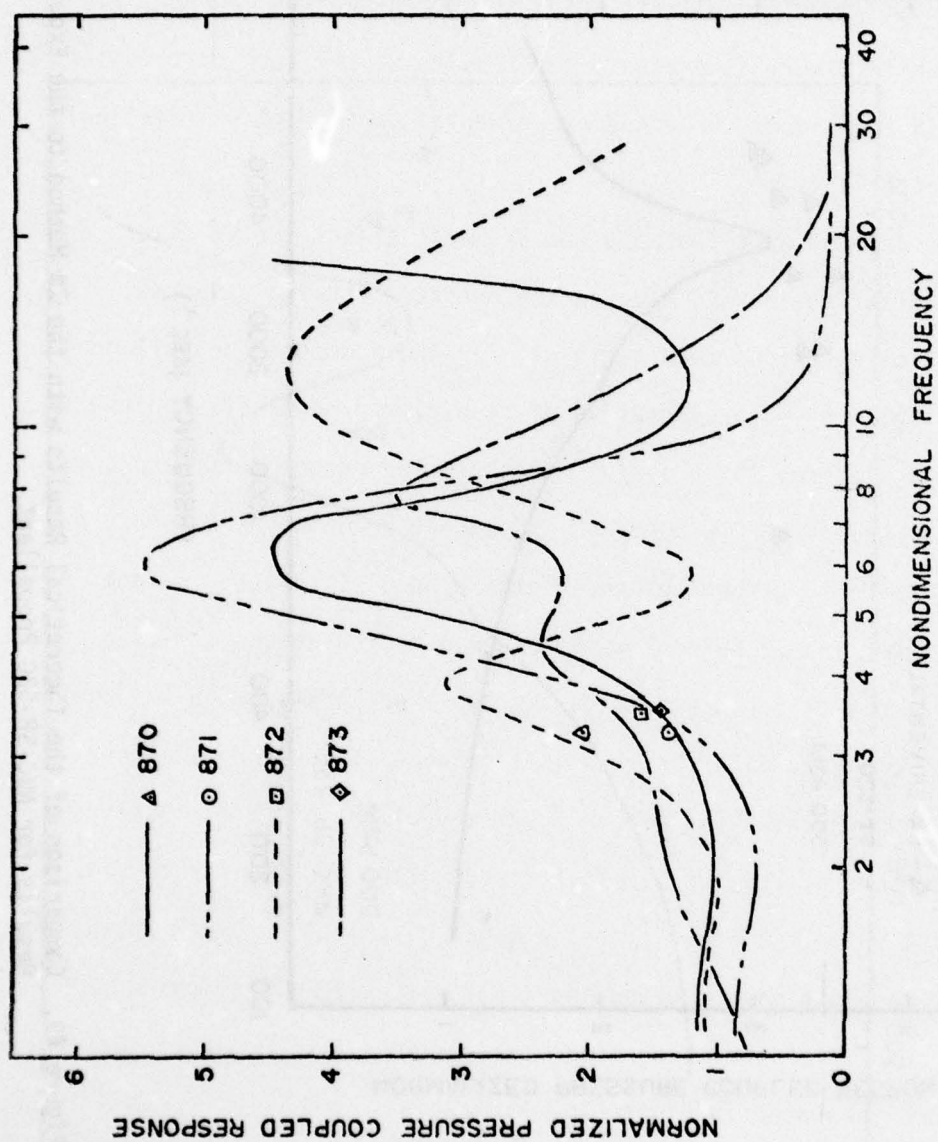


Figure 44. Comparison of the Theoretical Results with the Cohen - Denison and Baum Method to the Experimental Results for the Miller Propellants

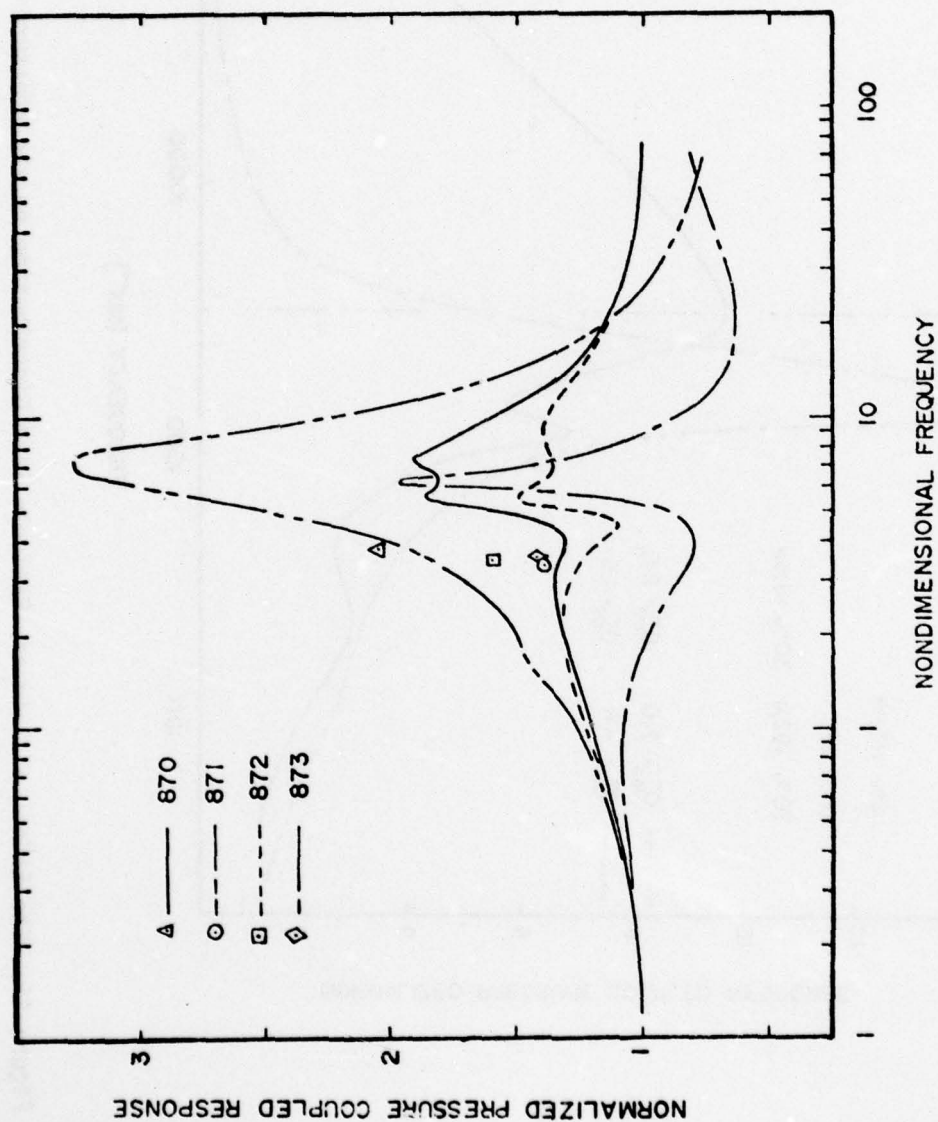


Figure 45. Comparison of the Theoretical Results with the ZN Method to the Experimental Results for the Miller Propellants



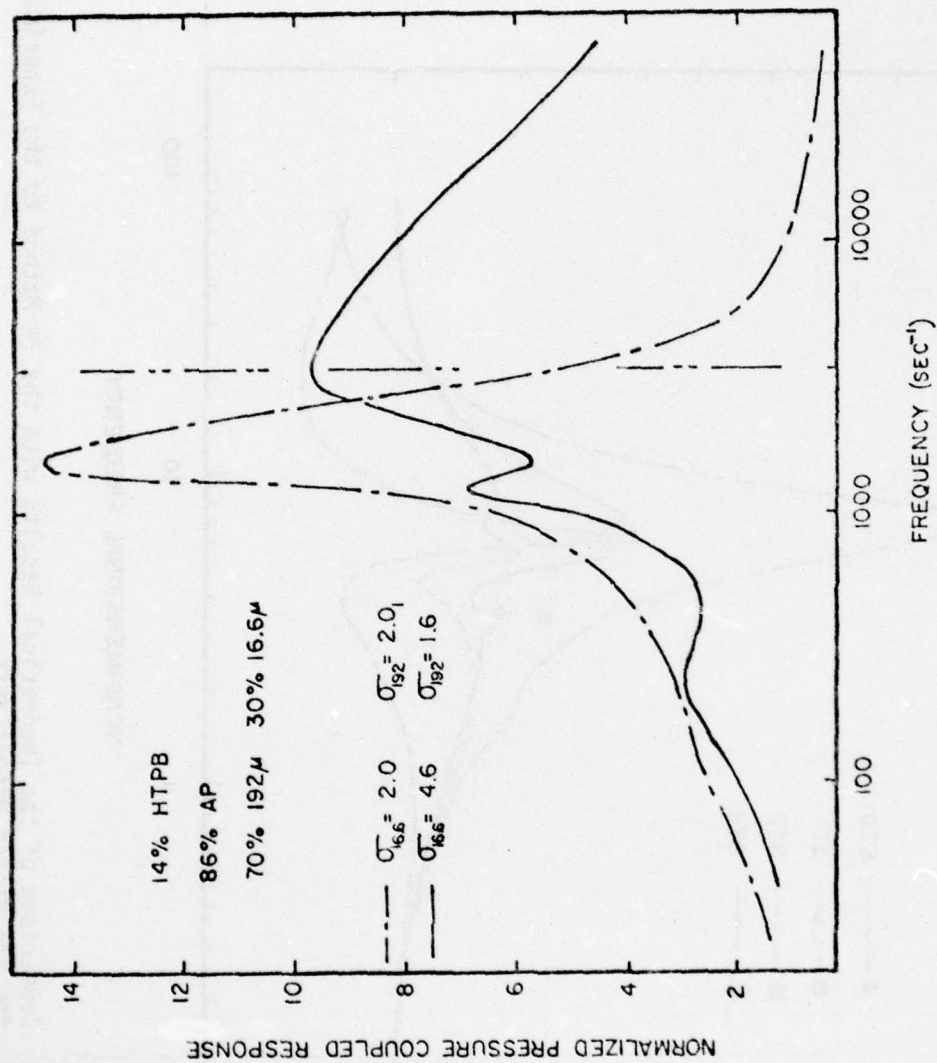


Figure 46. The Effect of Oxidizer Particle Size Distribution on the Pressure Coupled Response

AD-A056 892

PURDUE UNIV LAFAYETTE IND SCHOOL OF MECHANICAL ENGI--ETC F/G 21/9.2  
THE EFFECT OF OXIDIZER PARTICLE SIZE DISTRIBUTION ON THE STEADY--ETC(U)  
JUN 78 J A CONDON, J R OSBORN

F04611-76-C-0067

UNCLASSIFIED

AFRPL-TR-78-17

NL

3 OF 3

AD  
A056 892



END  
DATE  
FILMED  
9-78

DDC

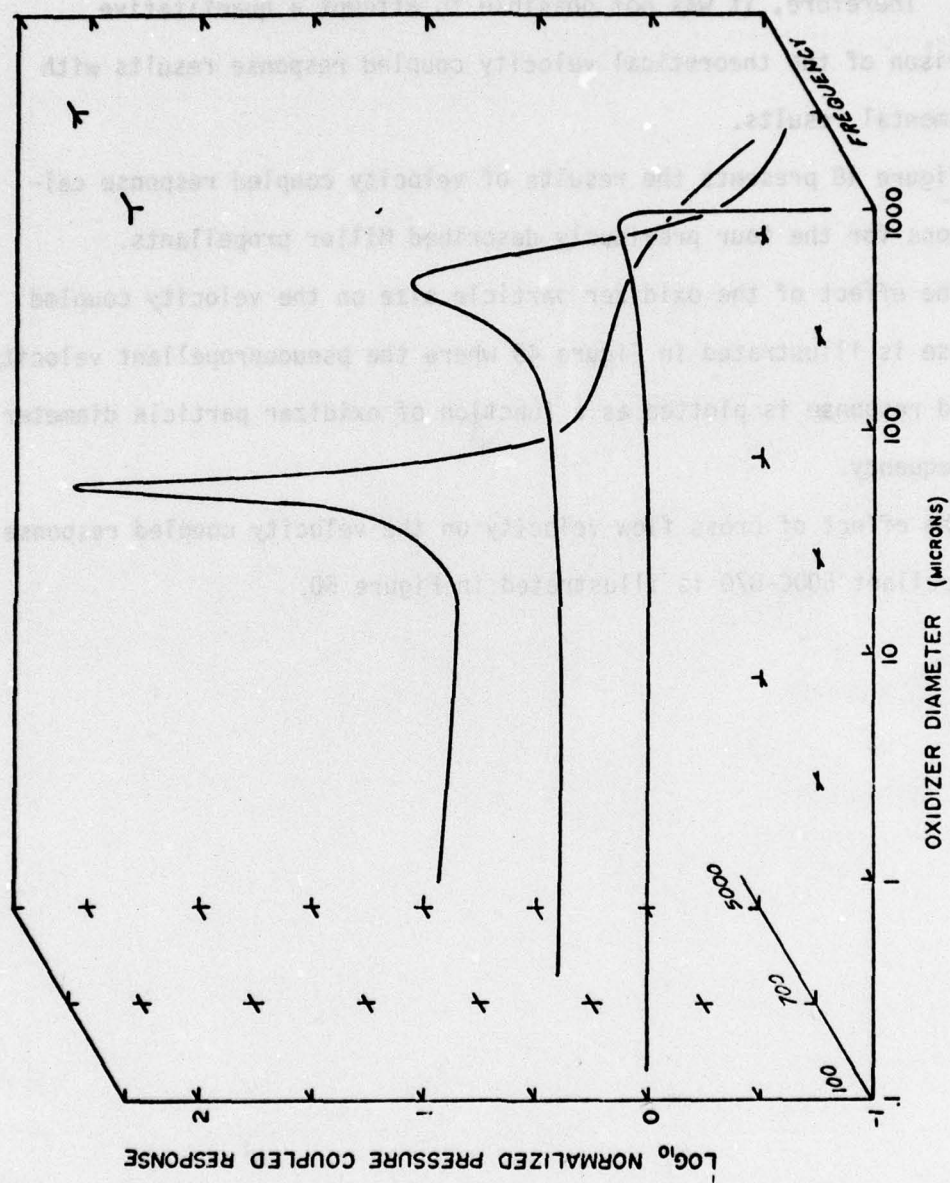


Figure 47. The Effect of Oxidizer Particle Size and Perturbation Frequency on the Pressure Coupled Response



### Velocity Coupled Response Results

At present there have been no experimental results for the velocity coupled response of composite propellants reported in the open literature. Therefore, it was not possible to attempt a quantitative comparison of the theoretical velocity coupled response results with experimental results.

Figure 48 presents the results of velocity coupled response calculations for the four previously described Miller propellants.

The effect of the oxidizer particle size on the velocity coupled response is illustrated in Figure 49 where the pseudopropellant velocity coupled response is plotted as a function of oxidizer particle diameter and frequency.

The effect of cross flow velocity on the velocity coupled response of propellant 50DC-870 is illustrated in Figure 50.

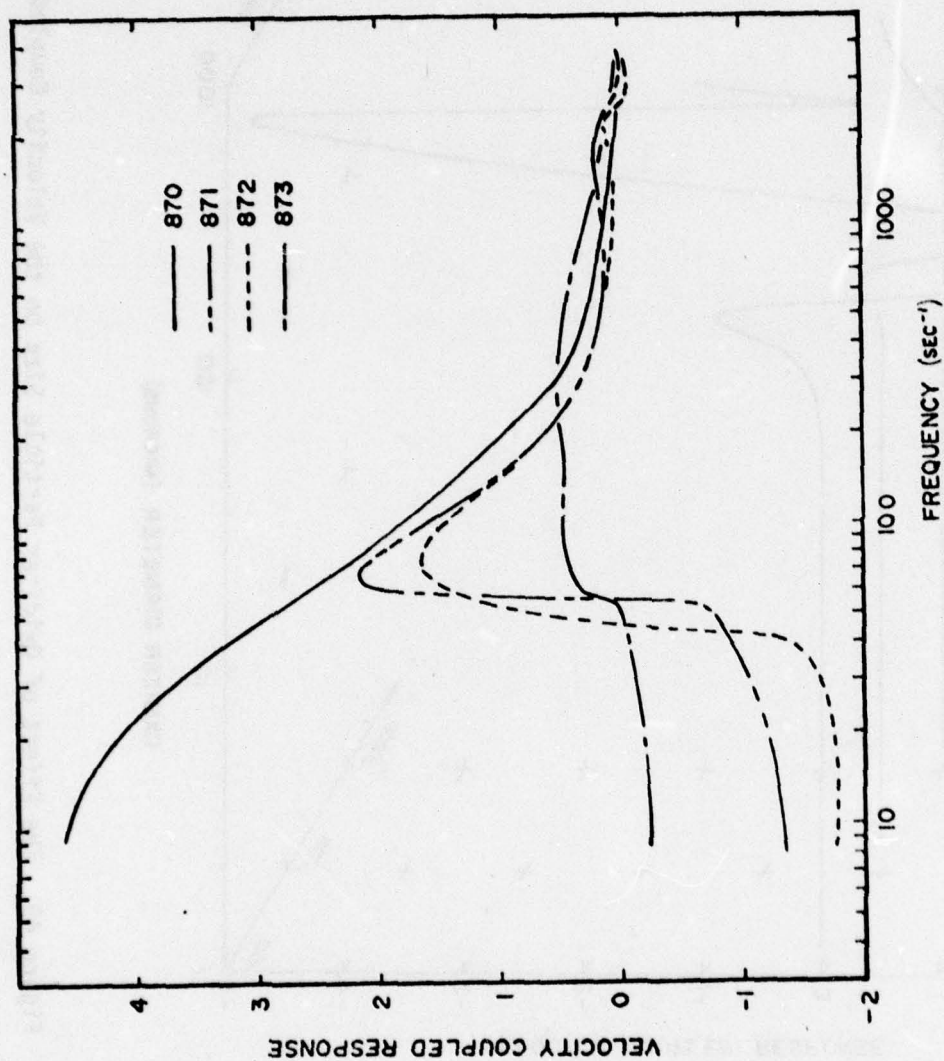


Figure 48. The Velocity Coupled Response for the Miller Acoustic Propellants

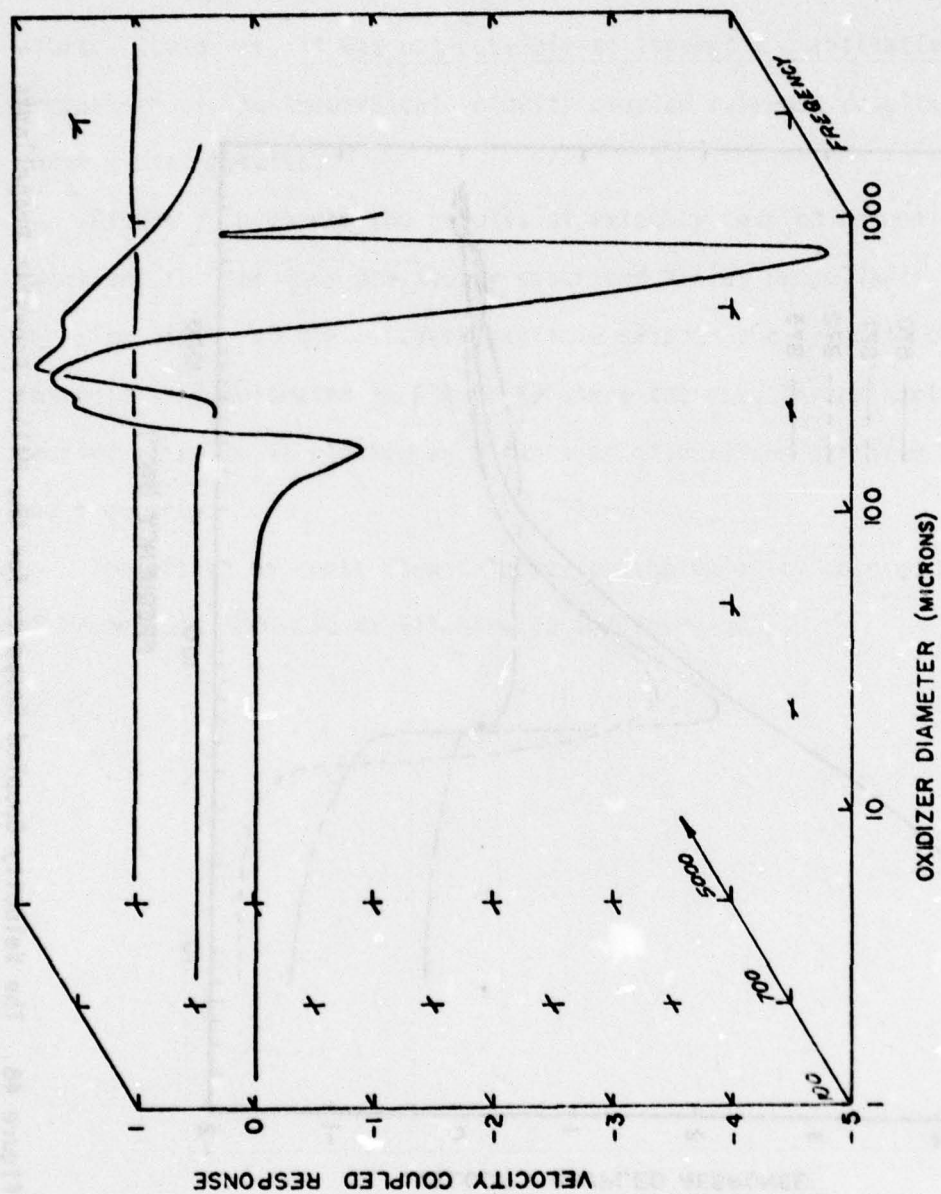


Figure 49. The Effect of Oxidizer Particle Size on the Velocity Coupled Response



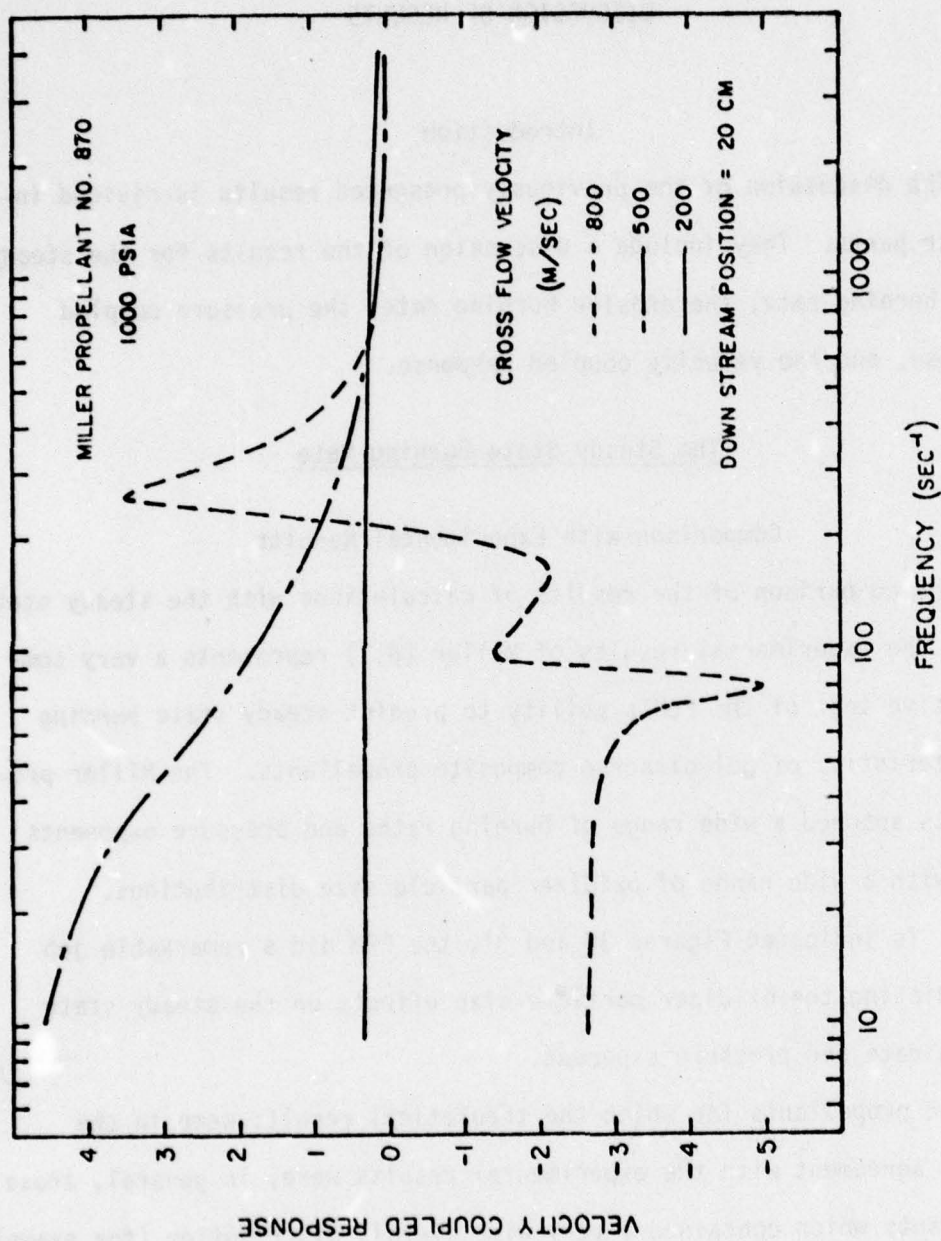


Figure 50. The Effect of Cross Flow Velocity on the Velocity Coupled Response

## DISCUSSION OF RESULTS

### Introduction

The discussion of the previously presented results is divided into four parts. They include a discussion of the results for the steady state burning rate, the erosive burning rate, the pressure coupled response, and the velocity coupled response.

### The Steady State Burning Rate

#### Comparison with Experimental Results

The comparison of the results of calculations with the steady state PEM to the experimental results of Miller (6,7) represents a very comprehensive test of the PEM's ability to predict steady state burning characteristics of polydisperse composite propellants. The Miller propellants spanned a wide range of burning rates and pressure exponents along with a wide range of oxidizer particle size distributions.

As is indicated Figures 30 and 31, the PEM did a remarkable job of predicting the oxidizer particle size effects on the steady state burning rate and pressure exponent.

The propellants for which the theoretical results were in the poorest agreement with the experimental results were, in general, those propellants which contained a very wide overall distribution (for example, propellants SD III-88-5, SD III-88-10 and SD III-88-15). Also, the theoretical results for those propellants containing 400 micron AP

were, in general, in poorer agreement with the experimental results. The PEM exponent prediction, on the other hand, was in good agreement with the experimental results for nearly every propellant.

One possible cause for the minor discrepancies in the burning rate prediction is that the geometric considerations in the PEM do not account for the micro scale surface roughness on the burning surface. That is, for the case of a wide overall particle size distribution, one would expect the burning surface geometric structure (on a micro scale) to be much rougher than for the case of a narrow overall distribution. This is due to the wide variation of burning rate with oxidizer particle size and the higher probability that a large particle will be surrounded by a large population of small particles (in the case of a wide overall distribution). The rougher micro surface structure would result in an increase in mass flux due to the increase in the ratio of the total burning surface area to the planar surface area.

Since the PEM does not presently account for the roughness of the burning surface, one would expect the PEM to underpredict the burning rate of propellants which contain a wide overall particle size distribution. That, however, was not the case. The PEM actually overpredicted the burning rate for the two propellants with the widest overall particle size distribution (SD III-88-5 and SD III-88-10). Thus, it may be concluded that the surface roughness effects are of a secondary nature in the burning rate determination.

Another possible explanation for the discrepancies is due to the assumption in the PEM that the pseudopropellants or unit flames, which compose the burning surface, burn independently of the surrounding



pseudopropellants. It is obvious that for the case of a wide overall distribution, there is a higher probability that the large particles in the distribution will be surrounded by a large population of small particles. This situation would increase the probability for flame interactions between adjacent pseudopropellants. Since flame interactions are not accounted for in the PEM one would expect the theoretical prediction to be in poorer agreement with the experimental results in the case of propellants with wide overall distributions. This was indeed the case.

It should be noted that the values for the constants used in the PEM, as presented in Table 4, all represent physically realistic values. Furthermore, most of the values have previously been reported in the literature. One constant used in the PEM for the comparison with the Miller data, however, was not a realistic one. Its value was selected to achieve a good agreement of the theoretical prediction with the experimental results. That constant is the particle diameter exponent for the amount of fuel associated with a particular oxidizer particle (see equation 127).

For an ordered packing of monodisperse particles it can be shown (21) that the value for the diameter exponent is two. In the case of a randomly packed polydispersion of spheres (the case for a composite propellant) the value of the diameter exponent is expected to be near two but certainly between values of one and three. The effect of the diameter exponent on the pseudopropellant properties of density, oxidizer mass fraction and oxidizer volume fraction are depicted in Figures 51, 52, and 53 respectively. The effect

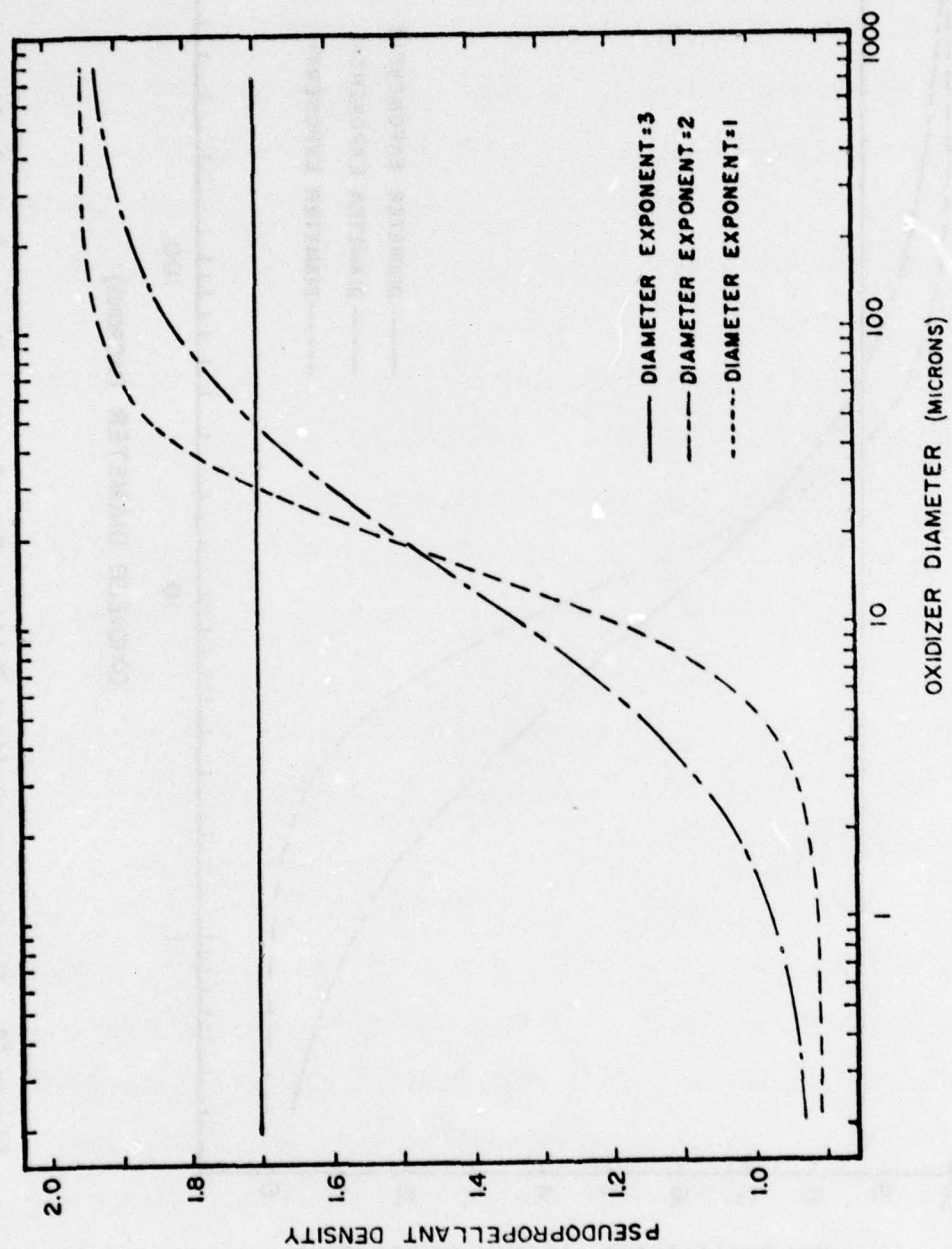


Figure 51. The Pseudopropellant Density Versus Oxidizer Particle Diameter

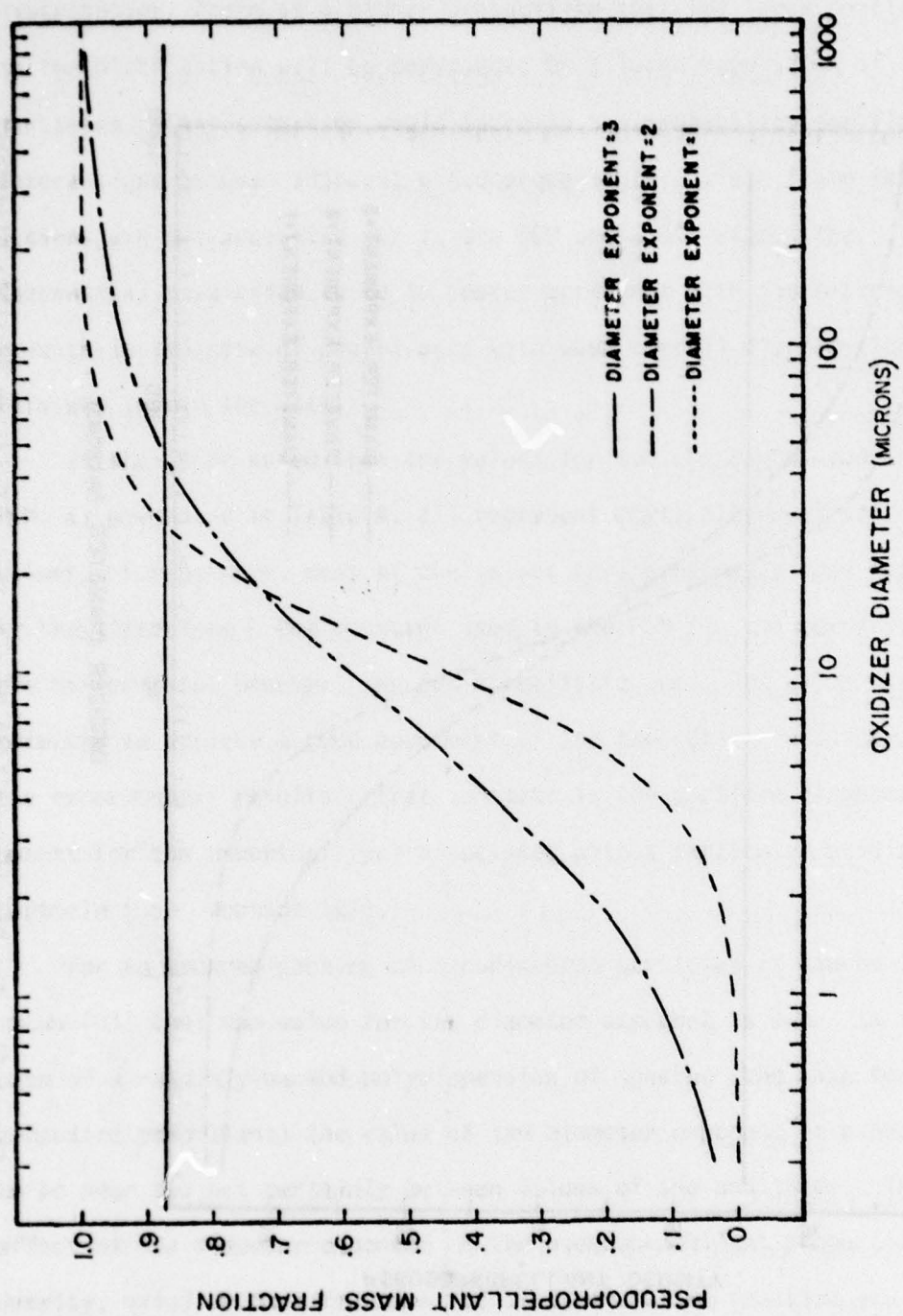


Figure 52. The Pseudopropellant Oxidizer Mass Fraction Versus Particle Size



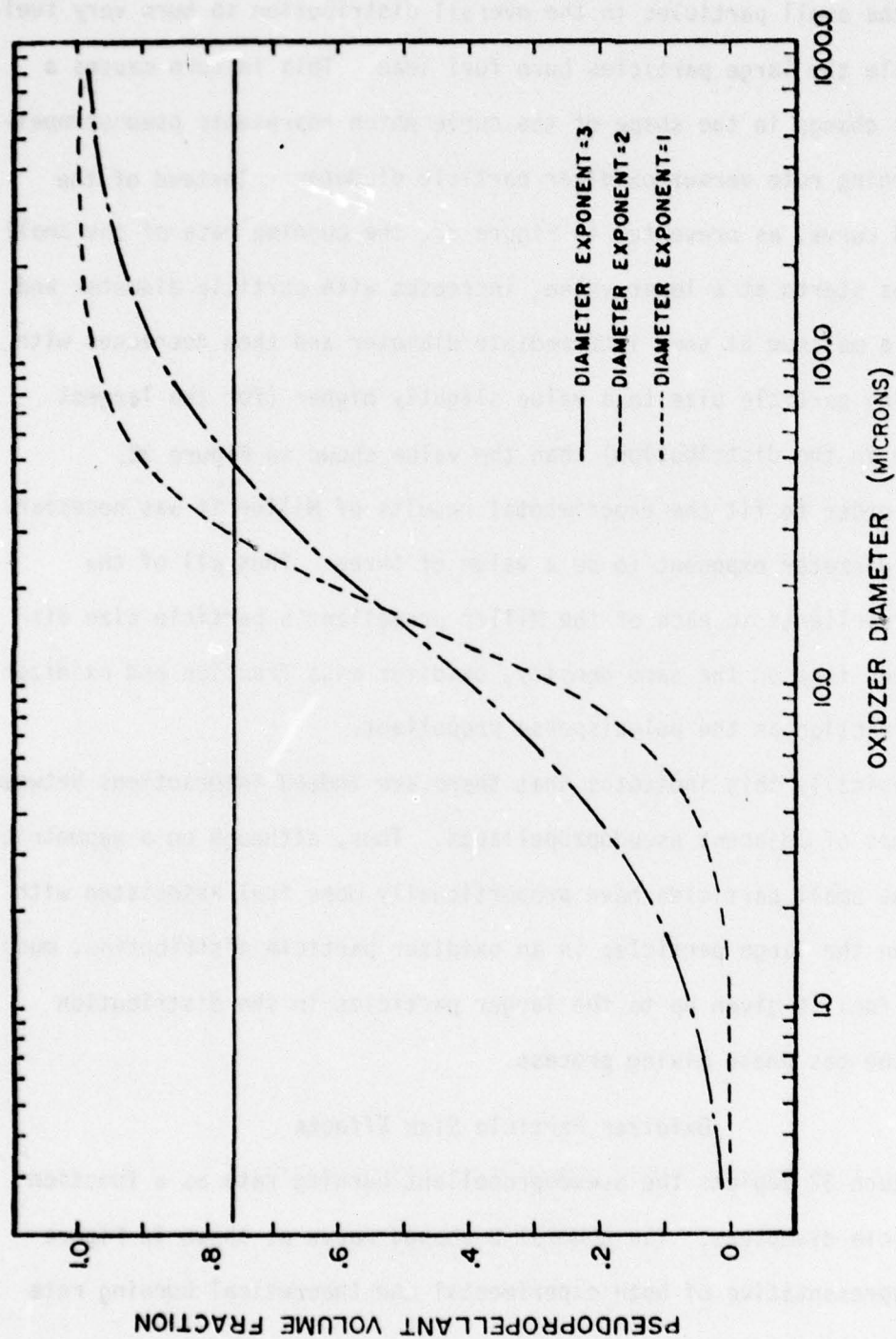


Figure 53. The Pseudopropellant Oxidizer Volume Fraction Versus Particle Size

of the diameter exponent on burning rate is dramatic. A value of two for the diameter exponent (the expected physically realistic value) causes the small particles in the overall distribution to burn very fuel rich while the large particles burn fuel lean. This in turn causes a dramatic change in the shape of the curve which represents pseudopropellant burning rate versus oxidizer particle diameter. Instead of the S-shaped curve, as presented in Figure 32, the burning rate of the small particles starts at a lower value, increases with particle diameter and reaches a maximum at some intermediate diameter and then decreases with increasing particle size to a value slightly higher (for the largest particle in the distribution) than the value shown in Figure 32.

In order to fit the experimental results of Miller it was necessary for the diameter exponent to be a value of three. Thus all of the pseudopropellants in each of the Miller propellant's particle size distributions took on the same density, oxidizer mass fraction and oxidizer volume fraction as the polydisperse propellant.

Physically this indicates that there are indeed interactions between the flames of adjacent pseudopropellants. Thus, although on a geometric basis the small particles have proportionally more fuel associated with them than the large particles in an oxidizer particle distribution, much of that fuel is given up to the larger particles in the distribution during the gas phase mixing process.

#### Oxidizer Particle Size Effects

Figure 32 depicts the pseudopropellant burning rate as a function of particle diameters. The general S-shaped curve as shown in Figure 32 is representative of both experimental and theoretical burning rate results.

The small particles yield high burning rates. As particle size decreases the burning rate approaches a limiting value determined by the premixed kinetic reaction standoff distance of a kinetically controlled primary flame between the oxidizer and the fuel binder. Conversely, the large particles yield low burning rates. As particle size increases, the burning rate approaches a limiting value determined by the kinetically controlled AP monopropellant flame. The burning rate for the intermediate diameters is determined by competing processes within each of the three flames above an individual oxidizer particle.

Figure 33 depicts the pseudopropellant burningrate pressure exponent as a function of oxidizer particle diameter. The exponent decreases from a value of near unity for the submicron size oxidizer to a minimum of about .34 for intermediate oxidizer particles of diameters between 10 and 100 microns. Above 100 microns the pressure exponent begins to increase approaching near unity for very large oxidizer particles.

To explain the pressure exponent phenomena exhibited by the pseudo-propellants, it is necessary to observe the controlling combustion mechanism for the given oxidizer particle size. For small particles the controlling flame is the primary flame. The limiting condition for small particles is a kinetically controlled primary flame. The physiochemical model then reduces to the following four equations:

$$\dot{m}_{ox} = A_{ox} \exp (-E_{ox}/RT_s)$$

32



$$T_s = T_o - \alpha Q_L / C_p - (1 - \alpha) Q_f / C_p + (Q_{PF} / C_p) \exp(-\xi_{PF}^*) \quad 284$$

$$\xi_{PF}^* = C_p \dot{m}_T^2 / (\lambda k p^{\delta_{PF}}) \quad 285$$

$$\dot{m}_T = (S_{ox} / S_T) \dot{m}_{ox} / \alpha \quad 178$$

The above four equations can be differentiated with respect to pressure to yield a closed form solution for the pressure exponent,  $n$ . The result after simplification is:

$$n = \frac{d \ln \dot{m}}{d \ln p} \quad 286$$

or

$$n = \delta_{PF} [(2 + C_p R T_s^2 / (E_{ox} Q_{pf} \xi_{pf}^* \exp(-\xi_{pf}^*)))^{-1}] \quad 287$$

Thus, the limiting value of the pressure exponent for small particles is determined by the value of the term inside the brackets times the primary flame reaction order. The value of that term is determined by the heat released in the primary flame, the specific heat of the combustion gases, the activation energy for the oxidizer decomposition process and the primary flame standoff distance. For typical values of the above parameters, the term inside the brackets has a value of about .5 and the pressure exponent is seen to be a little less than half of the primary flame gas phase reaction order, or of the order unity.

The same reasoning can be applied to the limiting condition of large oxidizer particles. For large particles the controlling mechanism is the kinetically controlled AP monopropellant flame, as the characteristic times for diffusion are so great that the heat feedback from the final diffusion flame is negligible. The physiochemical model then reduces to the following three equations:

$$\dot{m}_{ox} = A_{ox} \exp(-E_{ox}/RT_s) \quad 32$$

$$T_s = T_o - Q_1/C_p + (Q_{ox}/C_p) \exp(-\epsilon_{ap}^*) \quad 288$$

$$\epsilon_{ap}^* = C_p \dot{m}_{ox}^2 / \lambda K P^\delta \quad 289$$

The above three equations can be differentiated with respect to pressure to yield a closed form solution for the pressure exponent,  $n$ . The result after simplification is:

$$n = \delta_{AP} [(2 + C_p RT_s^2 / (E_{ox} Q_{AP} \epsilon_{AP}^* \exp(-\epsilon_{AP}^*)))^{-1}] \quad 290$$

Thus, the limiting value of the pressure exponent for large particles is analogous to the limiting condition for small particles. The limiting value of the exponent for large particles is determined by the value of the term inside the brackets times the ammonium perchlorate monopropellant flame reaction order. For typical values of the parameters in equation 290 the term inside the brackets has a value of about .5. Thus, the pressure exponent is again seen to be a little less than half of the AP flame monopropellant reaction order, or of order unity.

The pressure exponent for the intermediate particle sizes is not so easy to characterize since the controlling mechanism for the combustion of the intermediate particles is a complicated competitive process between the three flame zones. The surface geometry also changes with pressure for the intermediate particles to further complicate the process. The value of the exponent for the case of competing flames is partially diffusion controlled and the diffusion standoff distance is only a very weak function of pressure. Thus, the pressure exponent is lower for the case where diffusion takes a part in the controlling mechanism. The higher the dominance of diffusion in the controlling combustion process the lower will be the value of the pressure exponent.

Thus, it is obvious that the oxidizer particle size has a pronounced effect on the steady state burning characteristics. Furthermore, the burning characteristics can be tailored by appropriate adjustments in the oxidizer particle size distribution.

#### The Erosive Burning Rate

##### Comparison with Experimental Observations

As stated previously, the primary objective of performing calculations with the erosive PEM was to illustrate that the model does indeed predict the experimentally observed trends.

One of the more predominant experimental observations is that, as the flow velocity across a burning propellant surface is increased, no effect on the burning rate is observed until the cross flow velocity reaches a certain value (the threshold velocity). Figures 34 and 35 illustrate that the model does indeed predict a threshold velocity.



Physically, the threshold velocity is due to the interaction between blowing at the burning surface and the cross flow induced turbulent boundary layer. At low cross flow velocities the blowing parameter is very high. Consequently, the shear stress at the surface is very low and the velocity gradient in the flame zone region directly above the surface is very low. Thus, the contribution of turbulence to the transport properties in the gas phase reaction zone is negligible. The above situation is depicted in Figure 54a.

As the cross flow velocity is increased, a point is finally reached where the effect of turbulence is finally felt in the gas phase reaction zone as illustrated in Figure 54b.

Further increases in the cross flow velocity result in increases in the transport properties within the gas phase reaction zone due to the increased level of turbulence in that region.

The effect of burning rate on the threshold velocity has been widely observed. Slower burning propellants have lower threshold velocities than higher burning rate propellants. In order to illustrate that the erosive PEM predicts the correct effect of burning rate on the threshold velocity, it was necessary to compare the threshold velocities of propellants which contain identical oxidizer particle size distribution as well as identical composition; thereby eliminating the possible effects of flame temperature and oxidizer particle size on the threshold velocity. The computer propellants chosen for the illustration were all identical in composition and particle size distribution. Changes in the burning rate of the base line propellant were accomplished by simulating catalysis of the primary and AP flames. The

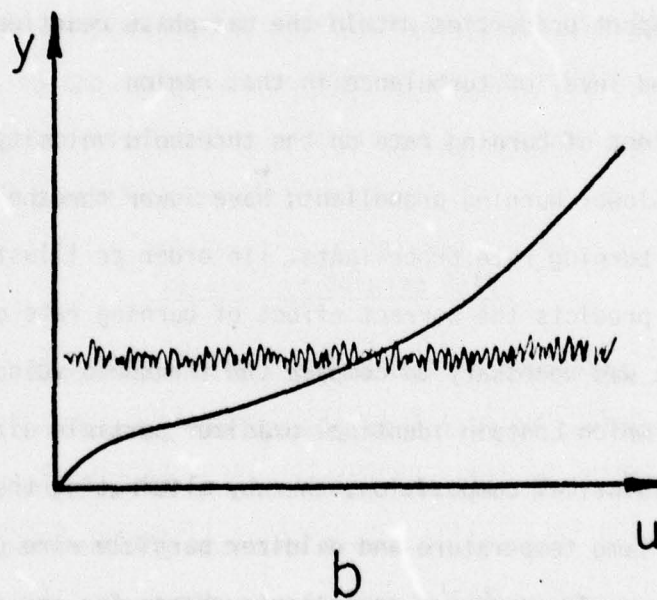
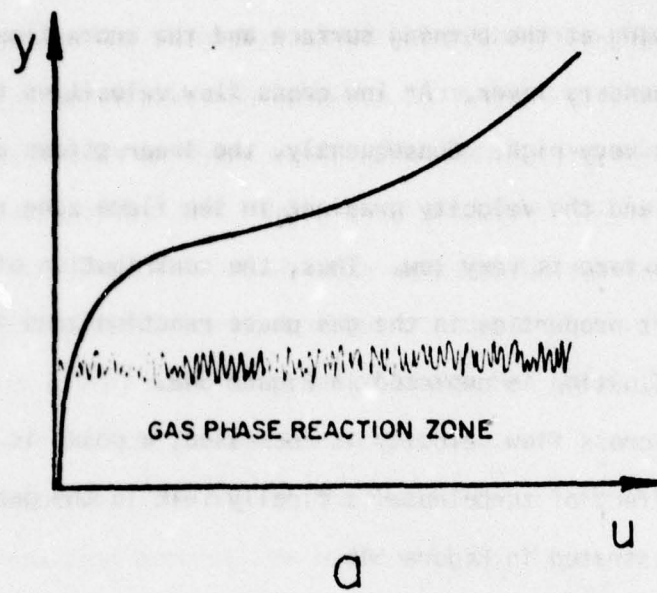


Figure 54. Gas Phase Reaction Zone in the Turbulent Boundary Layer

catalysis was simulated by adjusting the activation energies in the Arrhenius expressions for the primary and AP flame reaction rate constants. The results presented in Figure 36 illustrate that the model predicts the correct dependence of threshold velocity on the propellant burning rate.

The physical effect of burning rate on the threshold velocity can be explained solely by the effect of blowing on the turbulent boundary layer. For low burning rates the blowing rate is such that the turbulence penetrates into the gas phase reaction zone at lower cross flow velocities than in the case of high burning rate. As the burning rate is increased, the blowing parameter increases. This, in turn, increases the difficulty for turbulence penetration into the flame zone.

The effect of pressure on the threshold velocity would, at first thought, be expected to be analogous to the effect of burning rate on the threshold velocity. However, experimental evidence (65) suggests that this is not the case. Thus, the threshold velocity has been observed to decrease with increasing pressure. The same effect was also exhibited by the erosive PEM as illustrated in Figure 37. Thus, even though the blowing increases with increased pressure, the effect of pressure on the turbulent boundary layer is such that the shear stress (or velocity gradient) in the gas phase reaction zone increases with pressure at a faster rate than the increased blowing can decrease the shear stress.

#### Oxidizer Particle Size Effects

The effect of oxidizer particle size on the erosive burning characteristics was illustrated in Figure 38.



Physically, as the free stream velocity increases, the turbulence extends closer to the burning surface. Now, the combustion of the large particles is normally dominated by the kinetically controlled AP monopropellant flame (since the characteristic diffusion times are so large). However, as the free stream cross flow velocity is increased and the turbulence finally extends into the final flame zone, the average value of the transport properties for the final flame are enhanced. This decreases the characteristic diffusion time and increases the heat transfer from the final flame zone. The kinetically controlled AP monopropellant flame, on the other hand, is driven away from the surface due to the increased mass flow. Thus, as the free stream cross flow velocity is increased, the kinetically controlled AP flame becomes less dominant in the controlling mechanism and the final flame becomes more dominant. A point is finally reached where the AP flame has extended into the turbulence region. At this point the controlling mechanism is divided between the AP flame and the final flame.

As particle size is decreased, the characteristic time for diffusion becomes smaller. Thus, the degree of extension of the final flame into the turbulent region decreases with particle size.

The critical particle diameter for erosive burning is presented as a function of free stream velocity in Figure 39 (for a nominal burning rate of 1.3 centimeters per second and a pressure of 68 atmospheres). Thus, for a free stream cross flow velocity of 300 meters per second and a burning rate of 1.3 centimeters per second, there would be no erosive burning at a pressure of 68 atmospheres if all of the oxidizer

particles in the propellants particle size distribution were smaller than 100 microns in diameter.

### The Pressure Coupled Response

#### Comparison with Experimental Results

The two methods employed to calculate the pressure coupled response were the ZN technique and the Cohen-Denison and Baum technique. The latter technique utilizes two empirical constants (the proportionality constants for equations 83 and 84). The ZN technique, on the other hand, enables the pressure coupled response to be calculated from first principles. Both methods predicted the correct order of magnitude of the pressure coupled response for each of the propellants. See Figures 40 through 45 where the comparisons with the experimental data are presented.

In those propellants that contained a multimodal distribution of particle sizes, both methods predicted multiple peaks in the response function (Figures 42 through 45). The Cohen-Denison and Baum technique predicted the correct magnitude of the pressure coupled response, at least up to a frequency of 4000 hertz. The ZN technique, on the other hand, appears to underpredict the magnitude of the response. The latter technique did, however, correctly predict the frequency at which the experimental data indicated a maximum in the response function for both A-13 and NWC SP-520 propellants.

It is interesting to note that the Cohen-Denison and Baum technique predicted the pressure coupled response of the four Miller acoustic propellants (see Figure 44) to well within the experimental error in the data. However, all four of the propellants contained 400 micron AP,

which proved to be troublesome during the steady state burning rate predictions.

#### Oxidizer Particle Size Effects

The possible dramatic effect of the oxidizer particle size distribution on the pressure coupled response is illustrated in Figure 46. The particle size effect can be explained by looking at the response of each pseudopropellant in the oxidizer particle size distribution. Figure 47 presents the pseudopropellant pressure coupled response as a function of oxidizer particle diameter for several perturbation frequencies. It is seen that the large particles resonate and therefore dominate the response at low perturbation frequencies. As the frequency is increased, the resonance moves to smaller particle diameters. Furthermore, the magnitude of the response at the resonant particle diameter increases as the frequency increases. Thus, it is the small oxidizer particles in the distribution which drive up the magnitude of the pressure coupled response and the effect of the small particles is felt to a greater degree as the perturbation frequency is increased.

#### The Velocity Coupled Response

As stated previously, there have been no experimental results for the velocity coupled response of composite propellants reported in the open literature. Thus, it was not possible to attempt a quantitative comparison of the theoretical velocity coupled response results with experimental results.



### The Oxidizer Particle Size Effect

The velocity coupled response of each pseudopropellant is a complicated function of the pressure coupled response and the erosive strength of the pseudopropellant. Thus, it is much more difficult to determine the effect of oxidizer particle size on the velocity coupled response than in the case of the pressure coupled response alone. The effect of particle size on the erosive burning characteristics as well as the pressure coupled response of the pseudopropellants were described previously. Since the erosive effect is more dominant with the large oxidizer particles and the large oxidizer particles are only resonant at low frequencies, the velocity coupled response has the potential to be more dominant in propellants that contain large oxidizer particles. However, due to the complicated interaction between the pressure coupled response and the erosive strength, and the fact that the magnitude of the pressure coupled response of the pseudopropellants is higher for the smaller oxidizer particles, the velocity coupled response is positive only for the intermediate particle diameters. Figure 49 illustrates that as the perturbation frequency is increased, the magnitude of the velocity coupled response decreases. This is due to the fact that the resonant oxidizer particle diameter decreases to diameters where the erosive effect is negligible.

## CONCLUSIONS

### Introduction

The conclusions for the combustion of polydisperse composite propellants are divided into four parts. They are the steady state burning rate, the erosive burning rate, the pressure coupled response and the velocity coupled response.

### The Steady State Burning Rate

The results of calculations with the steady state PEM indicate that the model can accurately predict the burning rate and pressure exponent of HTPB/AP class propellants with a very wide range of oxidizer particle sizes.

Propellants containing a very wide overall distribution of particle sizes along with large particle diameters were in the poorest agreement with the experimental results. This was attributed to the PEM's lack of consideration of interactions between the flames of adjacent pseudo-propellants. The case for flame interactions was further demonstrated by the value for the diameter exponent in the equation which relates, geometrically, the amount of fuel associated with a particular oxidizer particle to the diameter of that particle. A value of 3.0 for the diameter exponent was necessary to obtain agreement of the theoretical results with the experimental results. Thus, although on a geometric basis small particles have proportionally more fuel associated with them

than do the large particles in an oxidizer particle distribution, much of that fuel is given up to the larger particles in the distribution during the gas phase mixing process.

The effect of the oxidizer particle size on the steady state burning rate has long been recognized. However, the effect of the oxidizer particle size distribution has not. The results of calculations with the PEM clearly indicate that the particle size distribution should be considered during the tailoring of propellants to meet specific burning rate and pressure exponent requirements. As will be discussed in a subsequent section, the advantages of employing the particle size distribution in the tailoring process becomes even more pronounced when the nonsteady burning characteristics are also to be considered in the tailoring process.

Some general conclusions concerning the effect of particle size on the burning rate and pressure exponent follow:

1. The burning rate of small particles approaches an upper limit determined by the premixed kinetically controlled primary flame between the oxidizer and the fuel binder.
2. The burning rate of large particles approaches a lower limiting value determined by the kinetically controlled AP monopropellant flame.
3. The burning rate of the intermediate particles lies somewhere between the above extremes and is determined by a competitive process between the three flames above a pseudopropellant.
4. The pressure exponent approaches a limiting value of approximately half the kinetically controlled primary flame reaction order for small particles.



5. The pressure exponent approaches a limiting value of approximately half the kinetically controlled AP monopropellant flame reaction order for large particles.

6. The pressure exponent of intermediate oxidizer particles is determined by the degree of dominance of diffusion in the controlling mechanism for combustion. The higher the degree of dominance of diffusion the lower will be the pressure exponent.

#### The Erosive Burning Rate

In the previous section it was demonstrated that the erosive PEM predicts the following experimentally observed trends in erosive burning:

1. Threshold velocities are usually observed.
2. Slower burning propellants are more strongly affected by cross flows than higher burning rate formulations.
3. The threshold velocity decreases as pressure is increased.

The agreement of the theoretically predicted trends with the experimentally observed trends indicates that the proposed theory for erosive burning is quite plausible.

Several conclusions concerning the physical mechanism for the threshold velocity can be stated:

1. At low cross flow velocities or high burning rates the blowing parameter is very high. Consequently, the shear stress or level of turbulence in the flame zone is very low and the contribution of turbulence to the transport properties in the gas phase reaction zone is negligible.

2. At higher cross flow velocities or very low burning rates the blowing parameter is low. Consequently, the shear stress or level of

turbulence in the flame zone enhances the transport properties in that flame zone.

3. The threshold velocity results since the turbulence cannot penetrate into the gas phase reaction zone (due to the blowing) until the cross flow velocity reaches a certain level.

4. The physical effect of burning rate on the threshold velocity is due solely to the effect of blowing on the turbulent boundary layer.

5. The effect of pressure on the threshold velocity is due to the effect of pressure on the turbulent boundary layer. Even though the blowing parameter increases with increased pressure, the shear stress in the gas phase reaction zone increases with pressure at a faster rate than the increased blowing can decrease the shear stress.

6. Due to the complicated interaction between the blowing parameter, the turbulent boundary layer and the burning rate; the erosive burning is not an additive effect.

The erosive PEM has also made possible several unique observations concerning the effect of the oxidizer particle size on the erosive burning characteristics of the polydisperse propellant. They are as follows:

1. As the cross flow velocity is increased, it is the large particles which are first affected as the turbulence extends into the final flame zone of the large particles.

2. Further increases in the cross flow velocity extends the turbulence into the flame zone of smaller oxidizer particles.

3. The dominant mechanism for the combustion of the large particles

shifts from the kinetically controlled AP monopropellant flame to a combination of that flame and the diffusion controlled final flame.

#### The Pressure Coupled Response

The two techniques employed to calculate the pressure coupled response, the ZN technique and the Cohen-Denison and Baum technique, both predicted the correct order of magnitude of the response in the comparisons to the experimental data. For frequencies below 4000 hertz the Cohen-Denison and Baum technique prediction of the magnitude of the response was in good agreement with the experimental results. The ZN technique, on the other hand, underpredicted the magnitude of the response in every case. The ZN technique did, however, predict the approximate frequency where the absolute maximum in the response function occurred in each case.

Multiple peaks in the response function were predicted by both methods.

Several conclusions concerning the effect of oxidizer particle size on the pressure coupled response follow:

1. At low frequencies the large particles are resonant; however, their response magnitude is low.
2. As frequency increases the resonance moves to smaller particles. Moreover, the magnitude of the resonant response increases.
3. Addition of fine oxidizer shifts the resonant frequency of the propellant to a higher frequency while increasing the magnitude of the peak. Conversely, addition of coarse oxidizer lowers the resonant frequency and the response magnitude.



4. The shape of the pressure coupled response curve can be adjusted so that relative minimums in the response occur at harmonic frequencies in the rocket motor chamber simply by adjusting the oxidizer particle size distribution.

#### The Velocity Coupled Response

The velocity coupled response calculations showed that for a linearized analysis, the velocity coupled response is a very complicated function of the pressure coupled response and the erosive strength of the individual pseudopropellants in the overall oxidizer particle size distribution.

The conclusions regarding the effect of the oxidizer particle size on the velocity coupled response follow:

1. At low perturbation frequencies the response is dominated by the large oxidizer particles and is negative.
2. As frequency increases the velocity coupled response becomes positive due to the influence of the intermediate sized oxidizer particles.
3. At high frequencies (on the order of 5000 hertz, but dependent on the propellant burning rate) the velocity coupled response vanishes.
4. In general, the velocity coupled response will be enhanced by the addition of coarse oxidizer and conversely the response will be depressed by the addition of fine oxidizer.

The theoretical results for velocity coupling are suspect for two reasons:

1. A linear analysis was employed so that the velocity and pressure coupled response could be assumed to be independent of each other.

2. The blocking effect due to injection at the surface was, for the sake of simplicity, ignored in the derivation of the relation between the velocity coupled and pressure coupled responses.

#### LIST OF REFERENCES

1. Cohen, N. S., Taylor, D. E., Small, K. R., Epstein, R. H., and Churchill, H. L., "Design of a Smokeless Solid Rocket Motor Emphasizing Combustion Stability," Lockheed Propulsion Company.
2. Beckstead, M. W., Boggs, T. L., and Madden, O. H., "The Effect of Oxidizer Particle Size and Binder Type on Nonacoustic Instability," AIAA paper 69-175, 1969.
3. Glick, R. L., "Prediction of Frequency from a Statistical BDP Model," 1975 AFOSR Meeting, Lancaster, California, July 1975.
4. Green, L. G., "Effects of Oxidizer Concentration and Particle Size on Resonance Burning of Composite Solid Propellants," Jet Propulsion 28, pp 159-164, March 1958.
5. Condon, J. A., Glick, R. L., and Osborn, J. R., "Statistical Analysis of Polydisperse, Heterogeneous Propellant Combustion: Nonsteady State," Thirteenth JANNAF Combustion Meeting, CPIA Publication 281, Vol. II, 1976.
6. Miller, R. R., Donohue, M. T., and Martin, J. R., "Control of Solids Distribution: I-Ballistics of Non-Aluminized HTPB Propellants," Thirteenth JANNAF Combustion Meeting, CPIA Publication 281, Vol. II, 1976.
7. Miller, R. R., Donohue, M. T., and Martin, J. R., "Control of Solids Distribution III-The Effects of Al Particle Size and Iron Oxide Addition on the Ballistics of HTPB Propellants," To be published in the proceedings of the Fourteenth JANNAF Combustion Meeting, Colorado Springs, Colorado, September, 1977.
8. Renie, J. P., Condon, J. A., and Osborn, J. R., "Oxidizer Distribution Effects," to be published in the proceedings of the Fourteenth JANNAF Combustion Meeting, Colorado Springs, Colorado, September, 1977.
9. Glick, R. L., "Steady State Combustion of Nonmetalized Composite Solid Propellants," Thiokol Corporation, Huntsville Division, Report No. U-75-27, July, 1975.



10. Glick, R. L., and Condon, J. A., "Statistical Analysis of Poly-disperse Heterogeneous Propellant Combustion: Steady State," Thirteenth JANNAF Combustion Meeting, CPIA Publication 281, Vol. II, 1976.
11. Hermance, C. E., "A Detailed Model of the Combustion Including Surface Heterogeneity and Heat Generation," AIAA Journal, Vol. 4, No. 9, pp 1629-1637, September, 1966.
12. Anderson, R., Brown, R., and Shannon, L., "Critical Comparison of Solid-Propellant Ignition Theories," TM-34-63-U2, UTC, 1963.
13. Anderson, R., Brown, R., and Shannon, L., "Heterogeneous Reactions in Ignition and Combustion of Solid Propellants," AIAA Journal, Vol. 2, pp 179-180, January, 1964.
14. Derr, R. L., Beckstead, M. W., and Cohen, N. S., "Combustion Tailoring Criteria for Solid Propellants," AFRPL-TR-69-190.
15. Jacobs, P. M. W., and Pearson, G. S., "Mechanism of the Decomposition of Ammonium Perchlorate," Combustion and Flame, Vol. 13, No. 4, August, 1969.
16. Summerfield, M., Sutherland, G. S., Webb, M. J., Tabak, H. J., and Hall, K. P., "Burning Mechanism of Ammonium Perchlorate Propellants," Solid Propellant Rocket Research, Vol. 1 of Progress in Astronautics and Rocketry, Academic Press, New York, pp 141-182, 1960.
17. Hermance, C. E., "A Detailed Model of the Combustion of Composite Solid Propellants," Proceedings of the ICRPG/AIAA 2nd Solid Propulsion Conference, pp 89-103, Anaheim, California, June 6-8, 1967.
18. Beckstead, M. W., Derr, R. L., and Price, C. F., "A Model of Composite Solid Propellant Combustion Based on Multiple Flames," AIAA Journal, Vol. 8, No. 12, pp 2200-2207, December, 1970.
19. Steinz, J. A., Stang, P. L., and Summerfield, M., "The Burning Mechanism of Ammonium Perchlorate-Based Composite Solid Propellants," AIAA Paper No. 68-658, June, 1968.
20. Miller, R. R., Hartman, K. O., and Myers, R. B., "Prediction of Ammonium Perchlorate Particle Size Effect on Composite Propellant Burning Rate," CPIA Publication 196, pp 567-591, 1970.
21. Blum, E. H., and Wilhelm, R. H., "A Statistical Geometric Approach to Random-Packed Beds," AICHE - Industrial Chemical Engineering Symposium Series No. 4, London Instn. Chem. Engrs., pp 4:21-4:27, 1965.

22. Beckstead, M. W., "Combustion Calculations for Composite Solid Propellants," Thirteenth JANNAF Combustion Meeting, CPIA Publication 281, Vol. II, 1976.
23. Beckstead, M. W., "A Model for Solid Propellant Combustion," To be published in the proceedings of the Fourteenth JANNAF Combustion Meeting, Colorado Springs, Colorado, September, 1977.
24. Cohen, N. S., Derr, R. L., and Price, C. F., "Extended Model of Solid Propellant Combustion Based on Multiple Flames," CPIA Publication 231, Vol. II, pp 25-42, 1972.
25. Shannon, L. J., and Petersen, E. E., "Deflagration Characteristics of Ammonium Perchlorate Strands," AIAA Journal, Vol. 2, No. 1, pp 168-169, January, 1964.
26. Burke, S. P., and Schumann, T. E. W., "Diffusion Flames," Ind. Eng. Chem., Vol. 20, 1928, p 998 (see also, First and Second Symposium on Combustion, The Combustion Institute, pp 2-11, Pittsburgh, Pennsylvania, 1965).
27. Williams, F. A., Combustion Theory, Addison-Wesley, pp 37-45, 1965.
28. Saderholm, C. A., "A Characterization of Erosive Burning for Composite H-Series Propellants," AIAA Solid Propellant Rocket Conference, Palo Alto, California, January 29, 1964.
29. Kreidler, J. W., "Erosive Burning, New Experimental Techniques and Methods of Analysis," AIAA Solid Propellant Rocket Conference, Palo Alto, California, January 29, 1964.
30. Schultz, R., Green, L., and Penner, S. S., "Studies of the Decomposition Mechanism, Erosive Burning, Sonance and Resonance for Solid Composite Propellants," Combustion and Propulsion, 3rd AGARD Colloquium, Pergamon Press, N. W., 1958.
31. Green, L., "Erosive Burning of Some Composite Propellants," Jet Propulsion, 24, 9, 1954.
32. Peretz, A., "Experimental Investigation of the Erosive Burning of Solid Propellant Grains with Variable Port Area," AIAA Journal, No. 6, p 910, 1968.
33. Marklund, T., and Lake, A., "Experimental Investigation of Propellant Erosion," ARS Journal, No. 30, p 173, 1960.
34. Dickinson, L. A., Jackson, F., and Odgers, A. L., "Erosive Burning of Polyurethane Propellants in Rocket Engines," Eighth Symposium (Int.) on Combustion, p 754, Williams and Wilkins, Baltimore, 1962.



35. Zucrow, M. J., Osborn, J. R., and Murphy, J. M., "An Experimental Investigation of the Erosive Burning Characteristics of a Non-homogeneous Solid Propellant," AIAA Journal, Vol. 3, p 523, 1965.
36. Velyunov, V. N., Dvoryashin, A. A., Margolin, A. D., Ordzhonikidze, S. K. and Pokhil, P. F., "Burning of Ballistite Type H in Sonic Flow," Fizika Goreniza i Vzryva, Vol. 8, No. 4, pp 501-505, October - December, 1972.
37. Lenoir, J. M., and Robillard, G., "A Mathematical Method to Predict the Effects of Erosive Burning in Solid Propellant Rockets," Sixth Symposium (Int.) on Combustion, p 663, Reinhold Publishing Corporation, New York, 1957.
38. Zucrow, M. J., Osborn J. R., and Murphy, J. M., "The Erosive Burning of a Nonhomogeneous Solid Propellant," AICHE Symposium Series No. 52, pp 23-29, 1964.
39. Corner, J., Theory of the Interior Ballistics of Guns, John Wiley and Sons, Inc., New York, 1950.
40. Zeldovich, T. B., "Theory of Propellant Combustion in a Gas Flow," Fizika Goreniza i Vzryva, Vol. 7, No. 4, pp 463-476, October - December, 1971.
41. Vilyunov, V. N., et al., "Burning of Ballistite Type H in Sonic Flow," Fizika Gorenize i Vzryava, Vol. 8, No. 4, pp 501-505, October - December, 1972.
42. Vanderkerchove, J., "Erosive Burning of a Colloidal Solid Propellant," Jet Propulsion, Vol. 28, p 599, 1958.
43. Lengelle, G., "Model Describing the Erosive Combustion and Velocity Response of Composite Propellants," AIAA Journal, Vol. 13, No. 3, March, 1975.
44. Saderholm, C. A., Biddle, R. A., Caveny, L. H., and Summerfield, M., "Combustion Mechanisms of Fuel Rich Propellants in Flow Fields," AIAA Paper No. 72-1145, presented at AIAA/SAE 8th Joint Propulsion Specialists Conference, New Orleans, Louisiana, November 29, 1972.
45. Tsuji, H., "An Aerothermochemical Analysis of Erosive Burning of Solid Propellant," Ninth Symposium (Int.) on Combustion, pp 384-393, 1963.
46. King, M., "An Analytical and Experimental Investigation of the Erosive Burning of Composite Propellants," to be published in the proceedings of the Fourteenth JANNAF Combustion Meeting, Colorado Springs, Colorado, September, 1977.



47. Mickley, H. S., and Davis, R. S., "Momentum Transfer for Flow Over a Flat Plate with Blowing," NACA Technical Note 4017, November, 1957.
48. Culick, F. E. C., "A Review of Calculations for Unsteady Burning of a Solid Propellant," AIAA Journal, Vol. 6, No. 12, pp 2241-2255, December, 1968.
49. Denison, M. R., and Baum, E., "A Simplified Model of Unstable Burning in Solid Propellants," ARS Journal, Vol. 31, No.8, pp 1112-1122, August, 1961.
50. Novozhilov, B.V., "Nonstationary Combustion of Solid Rocket Fuels," Nauka, Moscow, 1973.
51. Glick, R. L., "Statistical Analysis of Nonmetalized Composite Solid Propellant Combustion," CPIA Publication 243, Vol. I, pp 157-184, 1973.
52. Dallavalle, J. M., Micrometrics, Pitman Publishing Co., New York, pp 123-143, 1948.
53. Glick, R. L., and Condon, J.A., "Statistical Combustion Modeling: The Effect of Additives," To be published in the proceedings of the Fourteenth JANNAF Combustion Meeting, Colorado Springs, Colorado, September, 1977.
54. Rubensin, M. W., "An Analytical Estimation of Transpiration Cooling on the Heat Transfer and Skin-Friction Characteristics of a Compressible Turbulent Boundary Layer," NACA-TN 3341, December 1954.
55. Schlichting, H., Boundary Layer Theory, 4th ed., McGraw-Hill, New York, 1960.
56. Reynolds, W. C., Kays, W. M., and Kline, J. T., "Heat Transfer in the Turbulent Incompressible Boundary Layer: I Constant Wall Temperature," NASA Memo 12-1-58W, 1958.
57. Lees, L., "Convective Heat and Mass Transfer with Mass Addition and Chemical Reactions," Combustion and Propulsion, 3rd AGARD Colloquium, Palermo, Sicily, p 451, 1958.
58. Marxman, G., and Gilbert, M., "Turbulent Boundary Layer Combustion in the Hybrid Rocket," Ninth Symposium (Int.) on Combustion, p 371, 1963.
59. Landis, R. B., and Mills, A. F., "The Calculation of Turbulent Boundary Layers with Foreign Gas Injection," International Journal of Heat and Mass Transfer, Vol. 15, p 1905, October, 1972.

60. Zucrow, M. J., and Hoffman, J. D., Gas Dynamics: Volume I, John Wiley and Sons, Inc., New York, N.Y., 1976.
61. Holt, J. F., "Numerical Solution of Nonlinear Two Point Boundary Problems by Finite Difference Methods," Numerical Analysis, Vol. 7, No. 6, June, 1961.
62. Muhlfeith, M., "Erosive Burning," Preliminary Report on the JANNAF Erosive Burning and Velocity Coupling Workshop, To be published in the proceedings of the Fourteenth JANNAF Combustion Meeting, Colorado Springs, Colorado, September, 1977.
63. Gordon, S., and McBride, B. J., "Computer Program for Calculations of Complex Chemical Equilibrium Compositions, Rocket Performance, Incident and Reflected Shocks and Chapman-Jouguet Detonations," NASA SP-273, 1971.
64. Crump, J.E., Personal Communication, 27 February, 1977.
65. Murphy, J. M., Technical Memorandum on the Current Status of Erosive Burning in Solid Propellant Rocket Motors, Jet Propulsion Center, Purdue University, Purdue JPC 313, No. TM-62-6, August, 1962.
66. Marxman, G. and Gilbert, M., "Turbulent Boundary Layer Combustion in the Hybrid Rocket," Ninth Symposium (Int.) on Combustion, p 371, 1963.